






Universitat Autònoma de Barcelona

ADVERTIMENT. L'accés als continguts d'aquesta tesi queda condicionat a l'acceptació de les condicions d'ús establertes per la següent llicència Creative Commons:  http://cat.creativecommons.org/?page_id=184

ADVERTENCIA. El acceso a los contenidos de esta tesis queda condicionado a la aceptación de las condiciones de uso establecidas por la siguiente licencia Creative Commons:  <http://es.creativecommons.org/blog/licencias/>

WARNING. The access to the contents of this doctoral thesis it is limited to the acceptance of the use conditions set by the following Creative Commons license:  <https://creativecommons.org/licenses/?lang=en>

MATHEMATICAL MODELLING OF ANGIOGENESIS
AS AN INTEGRATED MULTICELLULAR PROCESS

PhD Thesis

AUTHOR: DARIA STEPANOVA

SCIENTIFIC ADVISORS: TOMÁS ALARCÓN COR
HELEN M. BYRNE
PHILIP K. MAINI

ACADEMIC TUTOR: LLUÍS ALSÈDÀ SOLER

Universitat Autònoma de Barcelona (UAB)

Centre de Recerca Matemàtica (CRM)

Doctorate Programme in Mathematics

February 2022



© Daria Stepanova

All Rights Reserved, 2022

Contents

Acknowledgments	ii
Declaration	iii
Abstract	iv
Contents	vi
Chapter 1: Introduction	1
1.1 Motivation	1
1.2 Biological background of angiogenesis	3
1.2.1 Angiogenesis is a process of vasculature outgrowth	3
1.2.2 Phenotype specification of endothelial cells	5
1.2.3 Cell polarity, migration and cell-ECM interactions	8
1.2.4 Cell rearrangements	9
1.2.5 Cell proliferation and apoptosis	11
1.2.6 Later stages of angiogenesis	12
1.3 Mathematical modelling of random cell migration	13
1.4 Hybrid (multiscale) modelling	14
1.5 State of the art	16
1.5.1 Continuum models	17
1.5.2 Discrete and hybrid models	20
1.6 Problem outline and thesis structure	33
Chapter 2: A multiscale model of early angiogenesis	37
2.1 Summary	37
2.2 Experimental motivation	38
2.3 Model formulation	40
2.3.1 Summary of the multiscale model	40
2.3.2 Subcellular scale	43
2.3.3 Cellular scale	51
2.3.4 Tissue scale	58
2.3.5 Multiscale simulation algorithm	60
2.4 Description of quantitative metrics	61

2.5	Results	63
2.5.1	Emergent qualitative features: branching and VEGF sensitivity	63
2.5.2	Model calibration	66
2.5.3	Model validation	70
2.5.4	Sensitivity analysis	74
2.5.5	Model prediction: network structure and cell mixing	78
2.6	Discussion	82
Chapter 3: A method to coarse-grain multi-agent stochastic systems with regions of multistability		85
3.1	Summary	85
3.2	Motivation	86
3.3	Theoretical background on large deviation theory	90
3.4	Coarse-graining method	94
3.4.1	Individual agent system	94
3.4.2	Multi-agent system	101
3.5	Results	105
3.5.1	Application to EC phenotype specification	105
3.5.2	Spatial phenotype patterning in the CG system	108
3.5.3	Comparison of the full stochastic, CG and mean-field descriptions . .	112
3.6	Discussion	117
Chapter 4: Large-scale simulations of the multiscale model of angiogenesis		122
4.1	Summary	122
4.2	Motivation	123
4.3	Incorporating the CG system into the multiscale model of angiogenesis	126
4.3.1	Comparison to the CTMC benchmark	127
4.4	Cell proliferation	130
4.4.1	Cell cycle duration	132
4.4.2	Bell-shaped response of cell proliferation to VEGF activation	133
4.4.3	Influence of external microenvironment	136
4.4.4	Proliferation rate	137
4.4.5	Location of daughter cells	137
4.4.6	Asymmetric cell division	141
4.5	Vessel maturation	142
4.6	Results	143
4.6.1	Importance of vessel maturation on vasculature expansion	143
4.6.2	Effect of cell proliferation on vasculature expansion	144
4.6.3	Quantification of distances between cell nuclei	150
4.7	Discussion	154
Chapter 5: Conclusions and future work		157
Appendices		162

Appendix A: Theoretical modelling of phenotype specification via VEGF-Delta-Notch signalling	163
Appendix B: Supplementary materials for Chapter 2	168
B.1 Relating simulation units to experimental units	168
B.2 Subcellular scale: VEGF-Delta-Notch signalling pathway	169
B.3 Computational simulations of the multiscale model of angiogenesis	183
B.4 Next Subvolume (NSV) method	190
B.5 Metric definitions	190
B.6 Mixing measure	197
B.7 Quantification of simulated vascular networks	206
B.8 Sensitivity analysis	210
B.9 Supplementary movies, figures and tables	217
Appendix C: Supplementary materials for Chapter 3	235
C.1 Geometric minimum action method (gMAM)	235
C.2 System of stochastic differential equations of the VEGF-Delta-Notch model (individual cell)	236
C.3 Minimum action path (MAP) for the VEGF-Delta-Notch system in individual cell	237
C.4 Pseudocode algorithm for simulating the multi-agent CG model of a system with a region of multistability	240
C.5 Quantification metrics	241
C.6 Supplementary files, movies, figures and tables	242
Appendix D: Supplementary materials for Chapter 4	248
D.1 Details on computational simulations	248
D.2 Supplementary movies, figures and tables	248
Bibliography	265

Appendices

Appendix A

Theoretical modelling of phenotype specification via VEGF-Delta-Notch signalling

The Delta-Notch signalling pathway has been widely studied from the theoretical perspective. A review on existing mathematical models of this pathway in different biological contexts can be found in [191]. These models (see [191] and references therein) mainly focused on investigation of the contact-mediated lateral inhibition mechanism, where a cell adopting a specific phenotype inhibits its neighbours from adopting the same cell fate. This type of cell communication was shown to generate patterns of cells with alternating cell phenotypes. Most theoretical works explored the conditions necessary for emergence of phenotype patterning observed in living systems (e.g. phenotype specification of cells in *Drosophila* wings [154], endothelial cells [154], proneural cells [190]). Here, we briefly overview several early mathematical models of Delta-Notch signalling and models describing Delta-Notch interactions specific for ECs (coupled with VEGF activation, i.e. VEGF-Delta-Notch); a more detailed review on the lateral inhibition via Delta-Notch signalling in other biological contexts is out of the scope of this thesis.

A pioneering work on cell fate patterning via a lateral inhibition mechanism is by Collier et al. [182]. They considered a simple mathematical model which accounted for the levels of Notch activity and Delta ligand concentrations. The model was based on the following assumptions: (a) Notch activity in the focal cell can be described by an increasing function

of Delta levels in the cell's neighbours; (b) Notch activity down-regulates Delta production in the same cell. These assumptions constitute a negative feedback loop in gene expression of neighbouring cells. This leads to a competition between initially 'equal' cells and causes them to adopt divergent phenotypes. Collier and coworkers investigated their model analytically and numerically to determine the necessary conditions for the emergence of patterns. They performed simulations on a linear array of cells and on a small two-dimensional hexagonal lattice (with nearest neighbour interactions between cells in both geometries).

Further experimental studies of the Delta-Notch interactions revealed that this ligand and receptor can bind to each other on the membrane of the same cell; this interaction was termed *cis*-binding [153]. It was discovered that Delta trans-activates Notch in neighbouring cells (trans-binding), whereas it *cis*-inhibits Notch in its own cell [153]. However, the effects of Delta-Notch *cis*-interactions on phenotype patterning were unclear. Sprinzak and coworkers [153] developed an experimental model to monitor the dynamics of Notch, while manipulating the levels of *cis*- and trans-Delta available in the system. Their experimental results showed that the Notch response to increasing levels of trans-Delta was a gradual change in cell gene expression. By contrast, variations of *cis*-Delta levels generated an ultrasensitive cell phenotype switch. Sprinzak et al. used these experimental data to formulate a simple mathematical model which took into account mutual inhibition of Delta and Notch due to *cis*-interactions. Their model explained how this mechanism (i.e. mutual inhibition upon *cis*-binding) could generate phenotype patterning even in the absence of the Delta-Notch trans-interaction feedback (e.g. as was done in [182]). The mechanism of mutual inactivation was further analysed from the theoretical point of view in a follow-up paper by this research group [154]. They explored the role of Delta-Notch *cis*-interactions on pattern formation. In particular, the authors concluded that mutual *cis*-inhibition of Delta and Notch speeds up pattern formation, extends the range of parameter values for which phenotype patterning is observed and leads to pattern formation even without cooperative interactions [154].

Bentley and coworkers proposed another mechanism capable of amplifying differences in

gene expressions of neighbouring cells, thus driving phenotype patterning in endothelial cells [218]. Specifically, they suggested that active perception of the external microenvironment via filopodia (long, thin membrane protrusions) equips ECs with a mechanism to generate phenotypic patterns and to speed up the patterning time. Indeed, ECs are characterised by an abundance of VEGF receptors at their filopodia. Thus, an EC (typically, tip cell) with filopodia can bind more VEGF, become further activated, develop more filopodia and, due to (VEGF-induced) up-regulation of Delta, inhibit more neighbouring cells. Bentley and colleagues used their memAgent model (overviewed in section 1.5.2) to explore the impact of this positive feedback due to filopodia formation in ECs on phenotype differentiation. Their simulation results suggest that filopodia formation decreases the time for establishment of a salt-and-pepper pattern (tip cell - stalk cell - tip cell). They also highlighted the importance of adequate timing for phenotype acquisition since cell shuffling and proliferation during sprout growth require dynamic re-establishment of the phenotype pattern, which directly affects the morphology of the growing vascular network.

The timing of phenotype patterning via VEGF-Delta-Notch signalling was further investigated in a mathematical model by Venkatraman et al. [157]. The model consisted of a system of deterministic equations for two ECs interacting via the VEGF-Delta-Notch signalling pathway. Their model accounts for the filopodia-induced positive feedback in EC VEGF sensitivity; cis-interactions of Delta and Notch are neglected. The analysis of this model revealed the existence of an intermediate EC phenotype (with intermediate levels of Delta and Notch as compared to stalk and tip cell stable steady state levels). Venkatraman and coworkers quantified the time it takes for two neighbouring ECs to acquire phenotypes in different external environments. In addition, they explored how positive (negative) modulators of Delta-Notch trans-binding which (de-) stabilise Notch activation affect phenotype patterning.

The third, intermediate, EC phenotype was also discovered in mathematical models by Boareto and coworkers, first, in the general context of Delta-Notch lateral inhibition [155],

and then in the particular case of VEGF-Delta-Notch signalling in ECs [156]. These models additionally took into account (trans- and cis-) interactions of Notch with Jagged, another Notch ligand. Notch activation was shown to inhibit Delta production (as was taken into account in previous models, e.g. [157], [182], [218]) and, by contrast, to up-regulate Jagged expression. Boareto and coworkers demonstrated that this asymmetric interaction of Notch with its two ligands (Delta and Jagged) led to the existence of the third cell phenotype. The authors referred to it as a hybrid tip/stalk phenotype (since it partially inherits the behaviour of both tip and stalk cells). Cells were shown to adopt the hybrid phenotype in conditions of down-regulated basal Delta production and Jagged overexpression. The authors associated these scenarios with pathological angiogenesis which leads to the formation of vascular networks with excessive, but thin and blind-ended, sprouts (e.g. typically observed in cancer) [156].

Koon and coworkers investigated mechanisms responsible for the diversity of phenotypic patterns observed in *in vitro* and *in vivo* angiogenesis [219]. In particular, most models of Delta-Notch lateral inhibition (e.g. [155]–[157], [182], [218]) were capable of reproducing classical ‘fine-grained’ salt-and-pepper patterns (when tip cells are separated by one or two stalk cells). However, patterns of varied separation between tip cells were observed in biological experiments [219] which could not be explained by traditional modes of Delta-Notch interactions (e.g. [154], [182]). Koon and colleagues demonstrated that the richness of patterns can be explained by the spatial heterogeneity of Notch distribution within cells and tension-dependent Delta-Notch trans-binding [219]. Their model considered a linear geometry of connected ECs with possibly distinct Notch levels at the lateral cell borders. Notch receptors were assumed to diffuse from one cell border to another. In addition, experimental evidence suggested that Notch activation is affected by intracellular tension due to cell-cell adhesion. Since Delta and Notch are also implicated in cell adhesion, the authors proposed that the Notch activation rate depends on the number of Delta-Notch complexes formed between adjacent cells (which determines adhesion, or tension, between cells). In particular,

Notch activation was assumed optimal for the target degree of adhesion and decreased when intracellular tension deviates from the optimum. With these two mechanisms (spatial Notch heterogeneity and tension-dependent Notch activation), the model by Koon et al. was capable to reproduce phenotypic patterns with varied distance between tip cells. Their model also predicts the existence of an intermediate EC phenotype.

A recent mathematical model by Debir et al. [220] investigated the effects of calcium signalling on the VEGF-Delta-Notch signalling pathway. They combined the two-cell phenotype specification model of Venkatraman and coworkers [157] with an experimentally validated model of calcium signalling in cells [221]. Specifically, the experimental results showed that VEGF activation of ECs induces oscillations in calcium release, which are directly connected to the Delta-Notch signalling. VEGF-induced Ca^{2+} activity leads to up-regulation of Delta production (thus favouring the tip cell phenotype), whereas downstream signalling cascades of Notch signalling lead to inhibition of calcium activity (thus favouring the stalk cell phenotype). These oscillations in Ca^{2+} release disappear as ECs adopt the stalk phenotype. By contrast, tip cells show periodic calcium fluctuations. The model by Debir et al. [220] was capable of capturing these effects of Ca^{2+} activity in EC phenotype specification. Nonetheless, although their simulation results show that cell phenotype depends on calcium activity, the model predicts that it is intracellular communication that determines the final cell fate.

Appendix B

Supplementary materials for Chapter 2

B.1 Relating simulation units to experimental units

Based on [4], [10], we approximated the correspondence between time, space and VEGF concentration in our simulations and real experiments.

Space Since in our model we account for cell nucleus positions, we chose the voxel size such that it approximately corresponds to the size of the nucleus of an endothelial cell. Thus, we fixed the voxel width, $h = 5 \mu m$.

Time In experiments from [4], [10], confocal microscopy imaging was carried out with time intervals of 15 minutes. Thus, in order to relate our simulation time to experimental time, we fix 0.03 of simulation time = 15 minutes. Then we calibrated our model, using this time correspondence, such that the dynamics of vascular growth in simulations and experiments from [4], [10] are in good quantitative agreement.

VEGF concentration In [4], [10], experiments were performed with uniform VEGF concentrations of 0, 5, and 50 ng/ml. Using molar mass of a VEGF molecule (40 kDa), the Avogadro constant ($N_A = 6.022 \times 10^{23} \text{ mol}^{-1}$) and assuming that a cell is exposed to all VEGF molecules within a sphere of radius equal to $20 \mu m$, simple computation yields the following correspondence

$V = 0$, external VEGF molecules ~ 0 *ng/ml*;

$V = 2500$, external VEGF molecules ~ 5 *ng/ml*;

$V = 25000$, external VEGF molecules ~ 50 *ng/ml*.

B.2 Subcellular scale: VEGF-Delta-Notch signalling pathway

The subcellular scale of our model accounts for the phenotype specification mediated by the VEGF-Delta-Notch signalling pathway. Within a growing tumour, hypoxic regions of the tissue secrete tumour angiogenic factors (TAFs), which diffuse towards the underlying vascular bed and activate quiescent endothelial cells (ECs), thus inducing angiogenic sprouting [18], [25]. We focus on the vascular endothelial growth factor (VEGF), the most well-studied TAF. The canonical Delta-Notch pathway interacts with the VEGF pathway enabling a contact-mediated communication between ECs allowing them to coordinate their decision making processes [16], [23], [27], [38]. Specifically, ECs acquire one of the two phenotypes, tip or stalk, which are characterised by distinct gene expression patterns (tip cells: high Delta and VEGFR2, low Notch; stalk cell: low Delta and VEGFR2, high Notch) [9], [27], [38]. Phenotypic switching modifies EC behaviour which is manifested in cell-cell and cell-ECM interactions [25], [32]. In our model, these interactions are accounted for at the cellular and tissue scales. In turn, the local extracellular environment (configuration of the cellular and tissue scales) serves as a modulator of VEGF-Delta-Notch signalling [18], [19], thus, dynamical coupling between scales is maintained in both directions. In this section, we present a more detailed description of the formulation of the subcellular scale model.

Phenotype specification via the VEGF-Delta-Notch signalling pathway has been extensively investigated from the mathematical modelling perspective [5], [37], [153]–[157], [182], [219]. Here, we combine the lateral inhibition model of the Delta-Notch signalling pathway

developed in [153], [154] with the VEGF signalling pathway as was done in [155], [156]. We refer to these works for a more detailed overview of the biological foundation of the model.

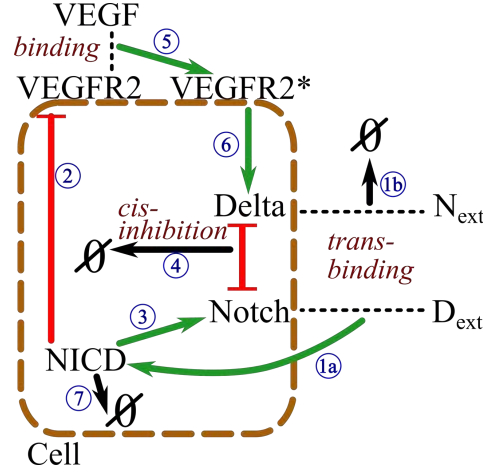
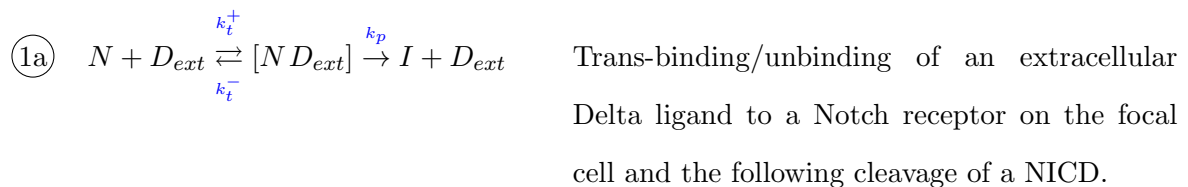
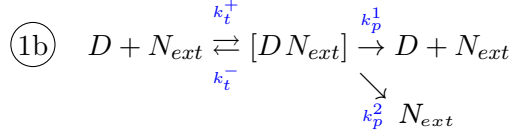


Figure B.1. An illustration of the kinetic reactions of the VEGF-Delta-Notch signalling pathway for the individual cell system. The reactions are labelled by blue circled numbers (see text for description). N_{ext} and D_{ext} represent extracellular levels of Notch and Delta, respectively.

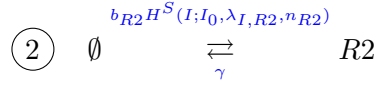
Individual cell system

Let N denote the level (number of proteins) of Notch receptor in a cell, D – Delta ligand, I – Notch intracellular domain (NICD), $R2$ – VEGF receptor 2 (VEGFR2) and $R2^*$ – activated, i.e. bound to VEGF, VEGFR2. We assume the focal cell is exposed to extracellular levels of Notch and Delta, N_{ext} and D_{ext} , respectively (which belong to neighbouring cells, whose signalling dynamics we do not account for explicitly in the individual cell system, thus N_{ext} and D_{ext} are assumed to be constant). We denote by V the extracellular level of VEGF. We assume V to be constant as maintained in many *in vitro* experiments (e.g. [4], [10]). The kinetic reactions involved in our model are (see the illustration in Figure B.1):

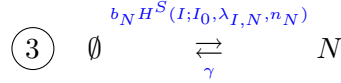




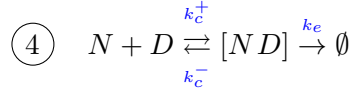
Trans-binding/unbinding of a Delta ligand on the focal cell to an extracellular Notch receptor on the focal cell followed by either endocytotic recycling of the Delta ligand (upper reaction with the rate k_p^1) or its degradation (lower reaction with the rate k_p^2).



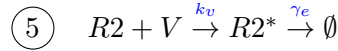
NICD-dependent production of a VEGFR2 receptor and its degradation at a constant rate.



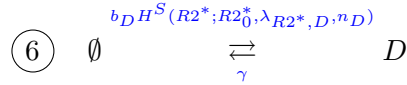
NICD-dependent production of a Notch receptor and its degradation at a constant rate.



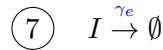
Mutual cis-inhibition of a Delta ligand and a Notch receptor [153], [154].



Binding of an external VEGF to a VEGFR2 and the following degradation of the activated receptor.



Production of a Delta ligand, dependent on activated (bound to VEGF) VEGFR2, and its degradation at a constant rate.



Degradation of a NICD.

Here $H^S(X; X_0, \lambda_{X,Y}, n_Y)$ is the so-called shifted Hill function:

$$H^S(X; X_0, \lambda_{X,Y}, n_Y) = \frac{1 + \lambda_{X,Y} \left(\frac{X}{X_0}\right)^{n_Y}}{1 + \left(\frac{X}{X_0}\right)^{n_Y}}. \quad (\text{B.1})$$

This function represents the transcriptional regulation of gene expression of a generic gene,

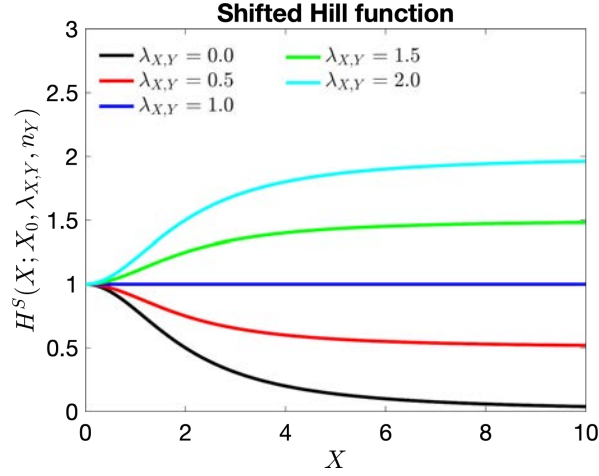
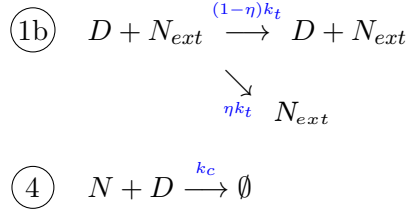


Figure B.2. An illustration of the shifted Hill function for varying parameter $\lambda_{X,Y}$. The functional form of $H^S(\cdot)$ is given by Eq (B.1). Here $X_0 = 2.0$, $n_Y = 2$.

Y , in response to the signalling variable X . X_0 and n_Y are positive parameters characterising the activation threshold and cooperativity, respectively. For $0 \leq \lambda_{X,Y} < 1$ ($\lambda_{X,Y} > 1$) the production of Y is down-regulated (up-regulated) as the amount of X increases; if $\lambda_{X,Y} = 1$ then X has no effect on production of Y (see Figure B.2). We assume that NICD signalling up-regulates production of Notch, thus $\lambda_{I,N} > 1.0$ (reaction ③), whereas production of VEGFR2 is down-regulated, $\lambda_{I,R2} < 1.0$ (reaction ②). Activated VEGFR2 enhances Delta production, $\lambda_{R2^*,D} > 1.0$ (reaction ⑥). In these reactions, prefactors of the type b_P characterise baseline production of the corresponding protein P .

We assume the same degradation rate, γ , for all inactivated proteins (Notch, Delta, VEGFR2). The half-life of activated signalling cues (NICD, activated VEGFR2) is much shorter, thus $\gamma_e > \gamma$ [156]. Furthermore, we assume that complexes [Delta-Notch] once formed release the signal or undergo endocytosis very fast compared to formation rate (i.e. $k_p^{1,2} \gg k_t^\pm$ and $k_e \gg k_c^\pm$). Thus, denoting $k_p = k_p^1 + k_p^2$, $k_t = k_t^+ \left(1 - \frac{k_t^-}{k_t^- + k_p}\right)$, $k_c = k_c^+ \left(1 - \frac{k_c^-}{k_c^- + k_e}\right)$ and $\eta = \frac{k_p^2}{k_p}$, we can simplify reactions ①a), ①b) and ④ :





Reaction label, R	Kinetic reaction(s)	Transition rate(s), α^R	Stoichiometric vector(s), ν^R
$\textcircled{1a}$	$N + D_{ext} \longrightarrow I + D_{ext}$	$k_t d_{ext} N, d_{ext} = D_{ext} / \Omega$	$(-1, 0, +1, 0, 0)^T$
$\textcircled{1b}$	$D + N_{ext} \longrightarrow N_{ext}$	$\eta k_t n_{ext} D, n_{ext} = N_{ext} / \Omega$	$(0, -1, 0, 0, 0)^T$
$\textcircled{2}$	$\emptyset \rightleftharpoons R2$	$[\rightarrow] \Omega b_{R2} H^S(I; \Omega I_0, \lambda_{I,R2}, n_{R2})$ $[\leftarrow] \gamma R2$	$(0, 0, 0, +1, 0)^T$ $(0, 0, 0, -1, 0)^T$
$\textcircled{3}$	$\emptyset \rightleftharpoons N$	$[\rightarrow] \Omega b_N H^S(I; \Omega I_0, \lambda_{I,N}, n_N)$ $[\leftarrow] \gamma N$	$(+1, 0, 0, 0, 0)^T$ $(-1, 0, 0, 0, 0)^T$
$\textcircled{4}$	$N + D \longrightarrow \emptyset$	$\frac{k_e}{\Omega} ND$	$(-1, -1, 0, 0, 0)^T$
$\textcircled{5}$	$R2 \longrightarrow R2^*$ $R2^* \longrightarrow \emptyset$	$V R2$ $\gamma_e R2^*$	$(0, 0, 0, -1, +1)^T$ $(0, 0, 0, 0, -1)^T$
$\textcircled{6}$	$\emptyset \rightleftharpoons D$	$[\rightarrow] \Omega b_D H^S(R2^*; \Omega R2_0^*, \lambda_{R2^*,D}, n_D)$ $[\leftarrow] \gamma D$	$(0, +1, 0, 0, 0)^T$ $(0, -1, 0, 0, 0)^T$
$\textcircled{7}$	$I \longrightarrow \emptyset$	$\gamma_e I$	$(0, 0, -1, 0, 0)^T$

Table B.1. Details of the kinetic reactions and the corresponding transition rates included in our full stochastic model of the VEGF-Delta-Notch signalling pathway within an individual cell. Ω represents system size, which is used to scale the transition rates [65] (in our simulations, we fix $\Omega = 200$). The stoichiometric vectors corresponding to a reaction R , ν^R , are indexed as $(N, D, I, R2, R2^*)^T$. Reaction labels are as in Figure B.1.

Given the transition rates and the corresponding stoichiometric vectors (listed in Table B.1), we can formulate our individual cell stochastic model of the VEGF-Delta-Notch pathway in terms of the Chemical Master Equation (CME)

$$\frac{\partial P(X, t)}{\partial t} = \sum_R (\alpha^R(X - \nu^R) P(X - \nu^R, t) - \alpha^R(X, t) P(X, t)), \quad (\text{B.2})$$

where $X = (N, D, I, R2, R2^*)^T$ and $P(X, t)$ is the probability of finding the system in state X at time t . This CME cannot be solved analytically but can be numerically simulated via the Gillespie algorithm (GA) [65] or the more efficient Next Subvolume (NSV) method [64] (for more details see Appendix B.4). The computational cost of these simulations rapidly increases with the system size, Ω . Furthermore, when extended to a multicellular system (see below), the simulation time increases as the number of cells in the system increases (linearly for the GA or logarithmically for the NSV method). Thus, high computational power is required to perform numerical simulations for large numbers of cells ($O(10^2) - O(10^3)$).

To illustrate the characteristic behaviour of the individual cell system given by the kinetic reactions ① - ⑦, we derive the associated mean-field limit equations:

$$\begin{aligned}
 \frac{dN}{dt} &= b_N H^S(I; I_0, \lambda_{I,N}, n_N) - \gamma N - k_t D_{ext} N - k_c N D, \\
 \frac{dD}{dt} &= b_D H^S(R2^*; R2_0^*, \lambda_{R2^*,D}, n_D) - \gamma D - \eta k_t N_{ext} D - k_c N D, \\
 \frac{dI}{dt} &= k_t D_{ext} N - \gamma_e I, \\
 \frac{dR2}{dt} &= b_{R2} H^S(I; I_0, \lambda_{I,R2}, n_{R2}) - \gamma R2 - k_v V R2, \\
 \frac{dR2^*}{dt} &= k_v V R2 - \gamma_e R2^*.
 \end{aligned} \tag{B.3}$$

A full description and reference values of the parameters used in Eq (B.3) can be found in Table B.7.

To facilitate the analysis of the system of equations Eq (B.3), we introduce dimensionless variables and parameters (shown in Table B.2). The non-dimensional individual cell system reads

$$\begin{aligned}
 \frac{dn}{dt} &= \beta_N H^S(\rho_N \iota; 1.0, \lambda_{I,N}, n_N) - n - d_{ext} n - \kappa n d, \\
 \frac{dd}{dt} &= \beta_D H^S(\rho_{R2} r2^*; 1.0, \lambda_{R2^*,D}, n_D) - d - \eta n_{ext} d - \kappa n d, \\
 \frac{d\iota}{dt} &= d_{ext} n - \hat{\tau} \iota, \\
 \frac{dr2}{dt} &= \beta_{R2} H^S(\rho_{N\iota}; 1.0, \lambda_{I,R2}, n_{R2}) - (1 + v_{ext}) r2, \\
 \frac{dr2^*}{dt} &= v_{ext} r2 - \hat{\tau} r2^*.
 \end{aligned} \tag{B.4}$$

For simplicity, we omit the bar in the dimensionless time variable.

We have studied numerically how the d - and n -nullclines of the system of equations Eq (B.4) change as we vary the (non-dimensional) external Delta concentration, d_{ext} . Figure B.3A shows that for low values of d_{ext} (Figure B.3A (1)) lateral inhibition is not strong enough to suppress the default [16] tip phenotype. As d_{ext} increases, the system enters a bistable regime where both phenotypes, tip and stalk cell, coexist (see Figure B.3A (2)). Finally, for higher values of d_{ext} , the tip phenotype is suppressed and the only stable steady state of the system of equations Eq (B.4) corresponds to the stalk cell phenotype (see Figure B.3A (3)). A general picture can be seen in a numerically computed bifurcation diagram (Figure B.3B). The effect of external VEGF, v_{ext} , on phenotype specification is to enlarge the bistability region as its concentration increases (see Figure B.3C). On the contrary, for a fixed value of v_{ext} , increasing concentration of the external Notch, n_{ext} , reduces the size of the bistability region (see Figure B.3D).

Variable/ Parameter	Ref. value	Description
$N_0 = \frac{\gamma}{k_t}$	2000.0	The characteristic level of Notch.
$D_0 = \frac{\gamma}{k_t}$	2000.0	The characteristic level of Delta.
$R2_0 = \frac{\gamma}{k_v}$	2000.0	The characteristic level of VEGFR2.
$\rho_N = \frac{N_0}{I_0}$	20.0	The ratio of the characteristic levels of Notch and NICD.
$\rho_{R2} = \frac{R2_0}{R2_0^*}$	10.0	The ratio of the characteristic levels of unbound and bound VEGFR2.
$n = \frac{N}{N_0}$		Non-dimensional Notch receptor concentration.
$D = \frac{D}{D_0}$		Non-dimensional Delta ligand concentration.
$\iota = \frac{I}{N_0}$		Non-dimensional NICD concentration.
$r2 = \frac{R2}{R2_0}$		Non-dimensional VEGFR2 concentration.
$r2^* = \frac{R2^*}{R2_0^*}$		Non-dimensional VEGF-bound VEGFR2 concentration.
$\beta_N = \frac{b_N k_t}{\gamma^2}$	2.5	Non-dimensional baseline expression of Notch receptor.
$\beta_D = \frac{b_D k_t}{\gamma^2}$	4.0	Non-dimensional baseline expression of Delta ligand.
$\beta_{R2} = \frac{b_N k_v}{\gamma^2}$	4.0	Non-dimensional baseline expression of VEGFR2.
$v_{ext} = \frac{k_v}{\gamma} V = \frac{V}{R2_0}$	1.25	Non-dimensional external VEGF concentration.
$d_{ext} = \frac{D_{ext}}{D_0}$	0.0–5.0	Non-dimensional external Delta ligand concentration.
$n_{ext} = \frac{N_{ext}}{N_0}$	0.0–5.0	Non-dimensional external Notch receptor concentration.
$\kappa = \frac{k_c}{k_t}$	12.0	The ratio of cis- and trans-binding for Delta and Notch. According to [153], $\kappa > 1$.
$\hat{\tau} = \frac{\gamma_e}{\gamma}$	5.0	The ratio of degradation rates of activated and non-activated receptors/ligands. Activated signals have shorter half-life, thus $\hat{\tau} > 1$.
$\bar{t} = \gamma t$		Non-dimensional time.

Table B.2. Non-dimensional variables and parameters of the VEGF-Delta-Notch system. The reference values are computed according to the dimensional parameter values listed in Table B.7. For the multicellular system external Notch and Delta, n_{ext} and d_{ext} , respectively, vary according to the configuration of the system (see text for details).

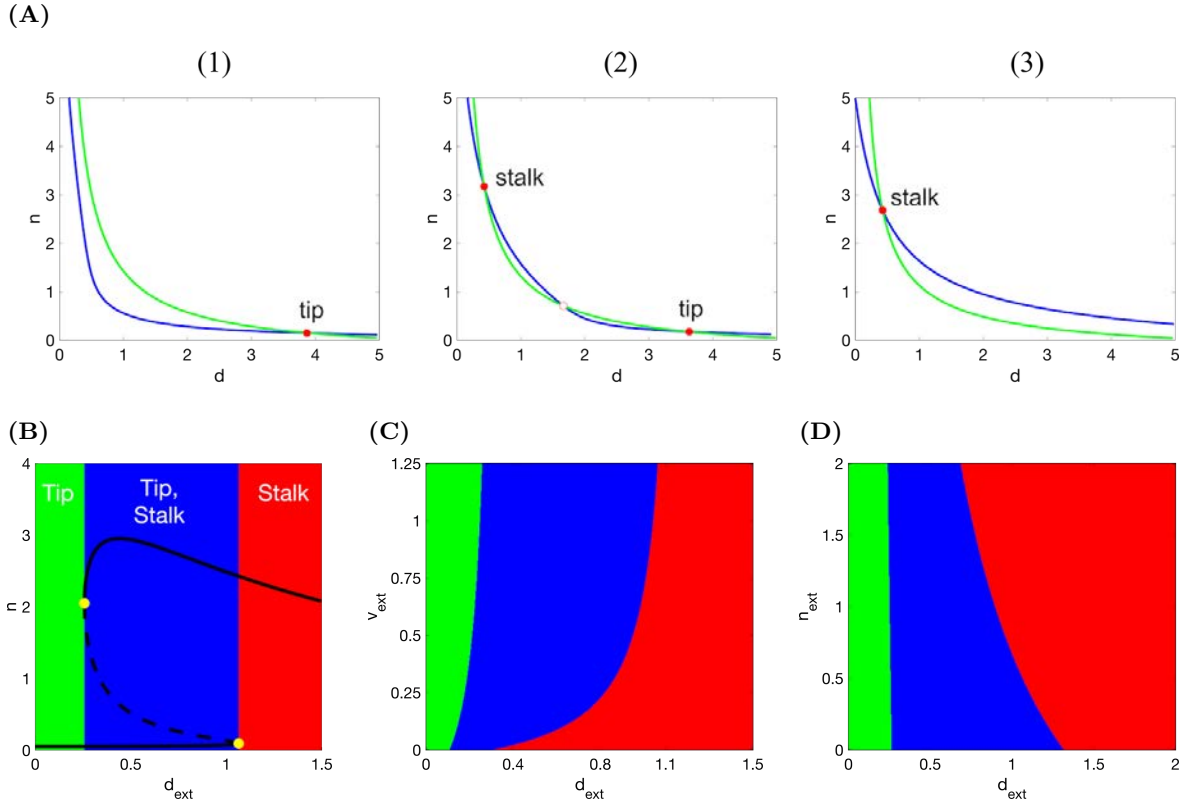


Figure B.3. Numerical simulations of the non-dimensional mean-field individual cell VEGF-Delta-Notch system (Eq (B.4)). (A) d - and n -nullclines for varying level of external Delta, d_{ext} . (1) For low values of d_{ext} (here $d_{ext} = 0.1$) there is only one (stable) steady state of the system corresponding to the tip cell phenotype. (2) A bistability region with two stable steady states: tip and stalk cells, occurs for intermediate values of d_{ext} (here $d_{ext} = 0.3$). The unstable saddle point is indicated by a red unfilled circle. (3) For higher values of d_{ext} (here $d_{ext} = 1.0$), the system is monostable with the stalk cell phenotype as its only (stable) steady state. (B) Bifurcation diagram of non-dimensional Notch concentration, n , as a function of external Delta ligand, d_{ext} , corresponding to the system of equations Eq (B.4). Full lines denote stable steady states; dashed lines – unstable steady state; yellow filled dots – saddle-node bifurcation points. (C) Phenotype diagram as a function of external Delta, d_{ext} , and external VEGF, v_{ext} , corresponding to the system of equations Eq (B.4). (D) Phenotype diagram as a function of external Delta, d_{ext} , and external Notch, n_{ext} , corresponding to the system of equations Eq (B.4). Parameter values used to make the plots (except for those indicated specifically) are listed in Table B.2.

Multicellular system

The individual cell model can be easily extended to a multicellular one. We need to specify the external levels of Delta and Notch (D_{ext} and N_{ext} , respectively) to which each individual cell is exposed. D_{ext} and N_{ext} are given by the levels of the corresponding proteins summed over all the neighbouring cells with which the focal cell is in contact. Since in our multiscale model of angiogenesis we account for cell nucleus positions instead of the exact cell membrane configurations, cell-cell interactions are assumed to be non-local, i.e. beyond their first neighbours. We define an interaction radius, R_s , and assume that two cells are in contact if they are contained (totally or partially) within a circular neighbourhood of radius R_s . Taking into account that we use an on-lattice modelling approach with a uniform hexagonal discretisation of the domain, we define a local neighbourhood of a cell located at the voxel with an index $k \in \mathbb{R}^2$, v_k , as a set of voxels

$$H(k) := \{v_l : v_l \cap \mathcal{B}_{R_s}(k) \neq \emptyset, l \neq k, l \in \mathcal{I}\}, \tag{B.5}$$

where $\mathcal{B}_{R_s}(k)$ denotes a circular neighbourhood of radius R_s centred at the centre of voxel k , and \mathcal{I} is the set of all voxel indices.

The amount of Delta on a neighbour $l \in H(k)$ which is in contact with Notch receptors of the cell of interest k is assumed to be proportional to the surface area of the overlap between the circular neighbourhood of the focal cell k and the neighbour l . This is given by the weights α_{kl} (see Figure 2.3A) defined as follows

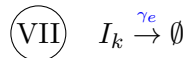
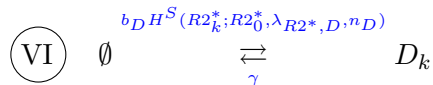
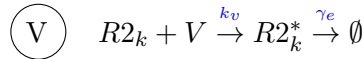
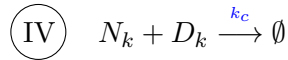
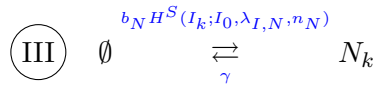
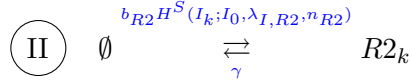
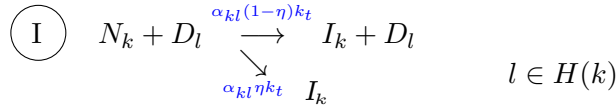
$$\alpha_{kl} = \frac{|v_l \cap \mathcal{B}_{R_s}(k)|}{|v_l|}, \quad k, l \in \mathcal{I}. \tag{B.6}$$

Here $|\cdot|$ stands for the surface area.

Thus, the external Delta (Notch) concentration, D_{ext} (N_{ext}), for a cell situated in a voxel v_k is defined as follows:

$$\begin{aligned}
 D_{ext} = \overline{D}_k &= \frac{\sum_{l \in H(k)} \alpha_{kl} D_l}{\sum_{l \in H(k)} \alpha_{kl}}, \\
 N_{ext} = \overline{N}_k &= \frac{\sum_{l \in H(k)} \alpha_{kl} N_l}{\sum_{l \in H(k)} \alpha_{kl}}.
 \end{aligned} \tag{B.7}$$

We can now rewrite the kinetic reactions ①-⑦ for the multicellular system in a straightforward manner. For each cell in the system, positioned in voxel v_k , we consider the following kinetic reactions (numbered with Roman numerals as equivalents of the kinetic reactions of the individual cell system numbered with Arabic numerals)



Note that now the reactions (1a) and (1b) of the individual cell system result in the same reaction (I) of the multicellular model. Reaction (I) is bimolecular between a Notch receptor in voxel v_k and a Delta ligand in a neighbouring cell in v_l . As a result of this reaction, a NICD is produced in the cell to which the Notch receptor belongs (voxel v_k) and Delta on the neighbour, D_l , is either degraded or endocytotically recycled.

To summarise, the subcellular scale of our model is a stochastic system given by the multicellular system with kinetic reactions (I)-(VII). We simulate it using a variation of the Stochastic Simulation Algorithm (SSA), the Next Subvolume method (NSV) [64] (more details in Appendix B.4). We list transition rates and the corresponding stoichiometric vectors used for simulation in Table B.3.

Reaction, R	Transition rate	ν_k^R	ν_l^R
I	$\frac{(1-\eta)\alpha_{kl}k_t}{\Omega} N_k D_l$	$(-1, 0, +1, 0, 0)^T$	$(0, 0, 0, 0, 0)^T$
	$\frac{\eta\alpha_{kl}k_t}{\Omega} N_k D_l$	$(-1, 0, +1, 0, 0)^T$	$(0, -1, 0, 0, 0)^T$
II	$\Omega b_{R2} H^S(I_k; \Omega I_0, \lambda_{I,R2}, n_{R2})$	$(0, 0, 0, +1, 0)^T$	$(0, 0, 0, 0, 0)^T$
	$\gamma R2_k$	$(0, 0, 0, -1, 0)^T$	$(0, 0, 0, 0, 0)^T$
III	$\Omega b_N H^S(I_k; \Omega I_0, \lambda_{I,N}, n_N)$	$(+1, 0, 0, 0, 0)^T$	$(0, 0, 0, 0, 0)^T$
	γN_k	$(-1, 0, 0, 0, 0)^T$	$(0, 0, 0, 0, 0)^T$
IV	$\frac{k_e}{\Omega} N_k D_k$	$(-1, -1, 0, 0, 0)^T$	$(0, 0, 0, 0, 0)^T$
V	$V R2_k$	$(0, 0, 0, -1, +1)^T$	$(0, 0, 0, 0, 0)^T$
	$\gamma_e R2_k^*$	$(0, 0, 0, 0, -1)^T$	$(0, 0, 0, 0, 0)^T$
VI	$\Omega b_D H^S(R2_k^*; \Omega R2_0^*, \lambda_{R2^*,D}, n_D)$	$(0, +1, 0, 0, 0)^T$	$(0, 0, 0, 0, 0)^T$
	γD_k	$(0, -1, 0, 0, 0)^T$	$(0, 0, 0, 0, 0)^T$
VII	$\gamma_e I_k$	$(0, 0, -1, 0, 0)^T$	$(0, 0, 0, 0, 0)^T$

Table B.3. Transition rates of the multicellular VEGF-Delta-Notch system. The transition rates are appropriately scaled with the system size parameter, Ω (in our simulations, we fix $\Omega = 200$). ν_r^R denotes a stoichiometric vector corresponding to a reaction R in a cell at voxel v_r indexed as $(N, D, I, R2, R2^*)^T$. The transition rates are calculated for all $k \in \mathcal{I}$ and $l \in H(k)$, where \mathcal{I} denotes the set of voxel indices in the system.

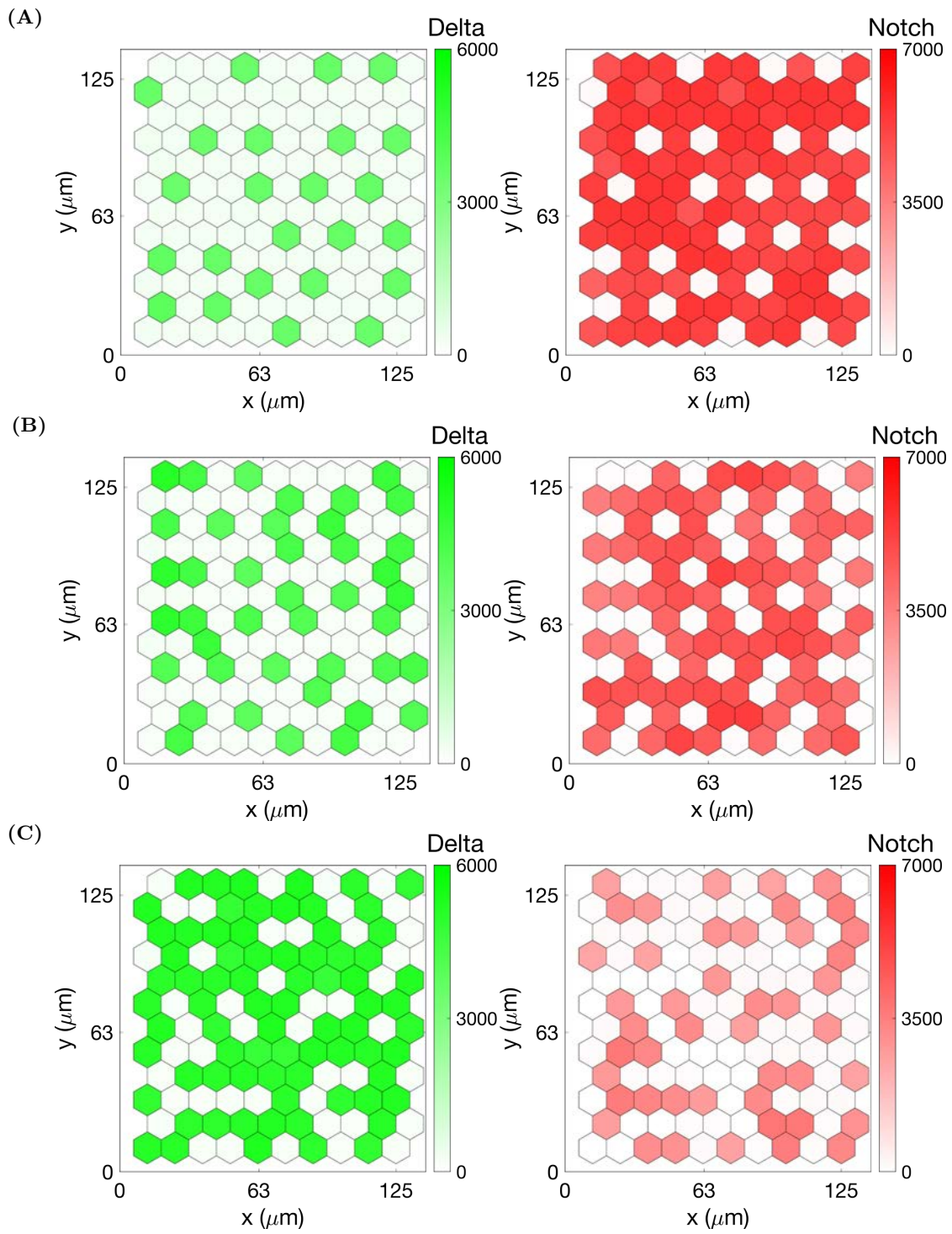


Figure B.4. (Caption on the next page.)

Figure B.4. Examples of steady state patterns of the VEGF-Delta-Notch multicellular system for different cis-inhibition parameter values. Final steady state patterns established during single stochastic simulations of the system described by the kinetic reactions (I)-(VII) for a uniform hexagonal lattice of 10×12 voxels. Cis-inhibition parameter was taken as (A) $k_c = 6.0e - 4$; (B) $k_c = 10.0e - 4$; (C) $k_c = 15.0e - 4$. External VEGF level, $V = 2500$, and the rest of the parameter values as in Table B.7.

When simulated in a simple two-dimensional domain, with only first-neighbour (voxels that share an edge) interactions, the multicellular system (reactions (I)-(VII)) produces the classical chessboard pattern [182] of alternating tip/stalk cells. However, our system amplifies the range of possible patterns beyond the classical one. This is due to accounting for mutual cis-inhibition of Delta and Notch within the same cell and non-locality of interactions within the radius R_s . Specifically, increasing the cis-binding parameter, k_c , allows tip cells to be neighbours since increasing k_c reduces the lateral inhibition ability of cells (see Figure B.4). In contrast, increasing interaction radius, R_s , enhances the ability of a tip cell to inhibit more neighbours and prevent them from acquiring the tip phenotype. Thus, the distance between two tip cells increases as R_s grows (see Figure B.15).

For completeness, we list the mean-field limit equations corresponding to the multicellular kinetic reactions (I)-(VII):

$$\begin{aligned}
 \frac{dN_k}{dt} &= b_N H^S(I_k; I_0, \lambda_{I,N}, n_N) - \gamma N_k - k_t \overline{D}_k N_k - k_c N_k D_k, \\
 \frac{dD_k}{dt} &= b_D H^S(R2_k^*; R2_0^*, \lambda_{R2^*,D}, n_D) - \gamma D_k - \eta k_t \overline{N}_k D_k - k_c N_k D_k, \\
 \frac{dI_k}{dt} &= k_t \overline{D}_k N_k - \gamma_e I_k, \\
 \frac{dR2_k}{dt} &= b_{R2} H^S(I_k; I_0, \lambda_{I,R2}, n_{R2}) - \gamma R2_k - k_v V R2_k, \\
 \frac{dR2_k^*}{dt} &= k_v V R2_k - \gamma_e R2_k^*.
 \end{aligned} \tag{B.8}$$

Here \overline{D}_k and \overline{N}_k are given by Eq (B.7) and $k \in \mathcal{I}$.

Similarly, for each voxel, v_k , in the lattice, the corresponding non-dimensional system of equations reads:

$$\begin{aligned}
 \frac{dn_k}{dt} &= \beta_N H^S(\rho_N \iota_k; 1.0, \lambda_{I,N}, n_N) - n_k - (d_{ext})_k n_k - \kappa n_k d_k, \\
 \frac{dd_k}{dt} &= \beta_D H^S(\rho_{R2} (r2^*)_k; 1.0, \lambda_{R2^*,D}, n_D) - d_k - \eta (n_{ext})_k d_k - \kappa n_k d_k, \\
 \frac{d\iota_k}{dt} &= (d_{ext})_k n_k - \hat{\tau} \iota_k, \\
 \frac{d(r2)_k}{dt} &= \beta_{R2} H^S(\rho_{N\iota_k}; 1.0, \lambda_{I,R2}, n_{R2}) - (1 + v_{ext}) (r2)_k, \\
 \frac{d(r2^*)_k}{dt} &= v_{ext} (r2)_k - \hat{\tau} (r2^*)_k, \\
 (d_{ext})_k &= \sum_{v_l \in H(k)} \alpha_{kl} d_l, \\
 (n_{ext})_k &= \sum_{v_l \in H(k)} \alpha_{kl} n_l.
 \end{aligned} \tag{A.9}$$

Here, again, cross-talk between neighbouring cells is accounted for via $(d_{ext})_k$ and $(n_{ext})_k$.

B.3 Computational simulations of the multiscale model of angiogenesis

Model geometry All simulations were performed on a rectangular lattice, $\mathcal{L} = \{v_i, i = (i_x, i_y)^T, i_x = 1, \dots, N_I^x, i_y = 1, \dots, N_I^y\}$, where v_i stands for voxel indexed by i , and i denotes the position of the voxel v_i within the lattice, \mathcal{L} . The total voxel number $N_I = N_I^x N_I^y$. N_I^x and N_I^y vary for each type of numerical experiment and are described in Table B.10. The non-dimensional voxel width, $h = 0.04$, corresponds to $5 \mu m$ (see Appendix B.1 for details).

Model parameters The parameter values used at the subcellular scale are listed in Table B.7. These values were used in all simulation experiments except those performed with mutant cells (for details, see below). Parameter values for the cellular and tissue scales are given in Table B.8.

Boundary conditions Let \mathcal{I}_B denote the set of voxels of \mathcal{L} situated on its boundary, i.e.

$$\begin{aligned} \mathcal{I}_B = & \{(1, i_y)^T, i_y = 1, \dots, N_I^y\} \cup \{(N_I^x, i_y)^T, i_y = 1, \dots, N_I^y\} \cup \\ & \{(i_x, 1)^T, i_x = 1, \dots, N_I^x\} \cup \{(i_x, N_I^y)^T, i_x = 1, \dots, N_I^x\}. \end{aligned}$$

As mentioned before, we assume that our simulations take place on a timescale such that cell proliferation is negligible and sprout elongation is driven by cell migration from the initial vascular plexus (imitating an underlying vascular bed in *in vivo* or a cell implant in *in vitro* experiments). This is implemented as a Dirichlet boundary condition for the nucleus distribution variable, \mathbf{E} , for the set of voxels corresponding to the position of the vascular plexus, \mathcal{I}_{VP} ,

$$E_i = 1 \quad \forall i \in \mathcal{I}_{VP}, \quad \forall t \geq 0.$$

The set \mathcal{I}_{VP} for each numerical experiment is listed in Table B.10. When a cell migrates from a voxel belonging to \mathcal{I}_{VP} , a new cell is put in this voxel with the baseline expression of the subcellular scale variables (its phenotype is established according to its environment in the following simulation of the subcellular model).

For the voxels on the boundary, a no-flux boundary condition is assumed for cells: migration transitions to leave the domain are set to zero, $\omega(i \rightarrow \text{exit } \mathcal{L}) = 0$, for $i \in \mathcal{I}_B$.

Since we assume that cells cannot leave the domain, we set the orientation landscape variable components pointing outside \mathcal{L} to zero. Mathematically, let n_e denote an external normal to \mathcal{L} , then

$$l_i^s = 0, \quad \forall i \in \mathcal{I}_B \text{ and } \forall s \in \mathcal{S} \text{ s.t. } (s, n_e) = 1,$$

where (\cdot, \cdot) denotes the scalar product.

The rest of the variables, namely, the variables of the subcellular scale, ECM and BM components, \mathbf{c} and \mathbf{m} , respectively, do not require any specific boundary conditions.

Initial conditions Let \mathcal{I}_{init} denote the voxel indices of the initial cell positions, i.e. $E_i = 1$ for $i \in \mathcal{I}_{init}$ and $E_i = 0$, otherwise, at time $t = 0$. Given this set of indices, the variables are initialised as shown in Table B.9.

Setups We performed several types of simulation experiments. For each type we specify the lattice dimensions, N_I^x and N_I^y , the set of indices corresponding to the vascular plexus, \mathcal{I}_{VP} , the initial cell nucleus positions, \mathcal{I}_{init} , the initial polarisation direction, s_{init} , the initial ECM and BM concentrations, c_{init} and m_{init} , respectively, and the distribution of VEGF, V . The details are given in Table B.10.

Simulations with mutant cells Some of the simulation experiments were performed with mutant cells with modified gene expression of VEGFR1 and VEGFR2, with the aim of imitating the behaviour of those used in experiments reported in [9]. To do so, we modify some of the parameters of the subcellular VEGF-Delta-Notch signalling. The details are given below in Table B.4.

In particular, VEGFR2^{+/-} mutant cells have down-regulated (by $\approx 50\%$, single allele mutants) gene expression of VEGFR2, thus we set its baseline expression to half of that for the WT (see Table B.4). VEGFR1^{+/-} mutant cells are characterised by halved gene expression of VEGFR1. VEGFR1 is known to be a sink receptor for VEGF: it has higher affinity for binding VEGF but low kinase activity. Hence, it competes with VEGFR2 for binding to VEGF but it has a minor role in signal transmission. Because of this, we have not considered it in our subcellular model of phenotype selection, and we need to account for the VEGFR1^{+/-} mutant in an effective way. Specifically, we assume that down-regulation of VEGFR1 can be accounted for by a higher affinity of VEGFR2 for binding to VEGF. We set $k_v^+ = 2k_v$ as shown in Table B.4. Furthermore, in some of the experiments by Jakobsson et al. [9], cells

Name [9]	Shortened name	Description	Change in parameters
VEGFR2 ^{+/egfp}	VEGFR2 ^{+/-}	Mutant cells heterozygous for VEGF receptor 2 having half of the amount of VEGFR2 compared with the WT cells.	$b_{R2}^+ = 0.5b_{R2}$
VEGFR2 ^{+/egfp} -DAPT	VEGFR2 ^{+/-} -DAPT	VEGFR2 ^{+/-} mutant cells additionally exposed to DAPT, a γ -secretase inhibitor abolishing the Notch signalling.	$b_{R2}^+ = 0.5b_{R2}$, $I = 0$
VEGFR1 ^{+/lacz}	VEGFR1 ^{+/-}	Mutant cells heterozygous for VEGF receptor 1 having half of the amount of VEGFR1 compared with the WT cells.	$k_v^+ = 2k_v$
VEGFR1 ^{+/lacz} -DAPT	VEGFR1 ^{+/-} -DAPT	VEGFR1 ^{+/-} mutant cells additionally exposed to DAPT, a γ -secretase inhibitor abolishing the Notch signalling.	$k_v^+ = 2k_v$, $I = 0$
WT-DAPT	WT-DAPT	Wild-type (WT) cells treated with DAPT, a γ -secretase inhibitor abolishing the Notch signalling.	$I = 0$

Table B.4. Description of mutant cells treated/untreated with DAPT (γ -secretase inhibitor) used in simulations. Changed parameters for mutant cells have + in their superscript position, compared to the wild-type (WT) cell parameters with no such superscripts.

were treated with a potent γ -secretase inhibitor, DAPT, which completely abolishes Notch signalling (see Fig 3i in [9]). γ -secretase is a protease that carries out the second cleavage releasing the active NICD. Therefore, when exposed to DAPT, the Notch receptor and its ligand should have the same dynamics as without DAPT, only NICD is not being produced. To introduce DAPT into our simulations, we set $I = 0$ for all cells in the simulation (both WT and mutant), leaving all other parameters unchanged (see Table B.4).

Multiscale simulation algorithm For the formulation of the algorithm we use the following notation:

\mathcal{I}	The set of voxel indices in the lattice, \mathcal{L} .
N_I	The total number of voxels in the lattice, \mathcal{L} .
$\mathcal{C}^s = (\mathbf{N}, \mathbf{D}, \mathbf{I}, \mathbf{R2}, \mathbf{R2}^*)$	The full-lattice configuration of the variables of the sub-cellular scale: Notch, $\mathbf{N} = (N_1, \dots, N_{N_I})$; Delta, $\mathbf{D} = (D_1, \dots, D_{N_I})$; NICD, $\mathbf{I} = (I_1, \dots, I_{N_I})$; VEGFR2, $\mathbf{R2} = (R2_1, \dots, R2_{N_I})$; activated (bound to VEGF) VEGFR2, $\mathbf{R2}^* = (R2_1^*, \dots, R2_{N_I}^*)$.
$\mathcal{C}_i^s = (N_i, D_i, I_i, R2_i, R2_i^*)$	The configuration of the variables of the subcellular scale in voxel v_i .
$\mathcal{C}^c = (\mathbf{E}, \mathbf{D}, \mathbf{c}, \mathbf{m}, \mathbf{l})$	The full-lattice configuration of the following variables: cellular scale cell distribution, $\mathbf{E} = (E_1, \dots, E_{N_I})$; sub-cellular Delta, $\mathbf{D} = (D_1, \dots, D_{N_I})$, used as a proxy to define cell phenotype; tissue scale ECM concentration, $\mathbf{c} = (c_1, \dots, c_{N_I})$; tissue scale BM component concentrations, $\mathbf{m} = (m_1, \dots, m_{N_I})$; tissue scale orientation landscape variable of ECM fibril alignment, $\mathbf{l} = (l_1, \dots, l_{N_I})$.
$\omega(i \rightarrow j)$	Transition rate for a migration event from voxel v_i to voxel v_j .
τ_{ij}	Time step corresponding to the transition $\omega(i \rightarrow j)$.
τ	Time step of the next transition to occur.

$\text{swap}(A_i, A_j)$	A swap operator for the variable A exchanging its values corresponding to voxels v_i and v_j , respectively.
t	Simulation time.
T_{max}	Final simulation time.
N_R	Number of realisations.

For clarity, we add a few comments to the pseudocode Algorithm 1.

line 1 Simulation setup is defined by specifying the lattice dimensions, N_I^x and N_I^y , the set of indices corresponding to the vascular plexus, \mathcal{I}_{VP} , the initial cell nucleus positions, \mathcal{I}_{init} , the initial ECM alignment, s_{init} , the initial ECM and BM component concentrations, c_{init} and m_{init} , respectively, the distribution of VEGF, V , and the final simulation time, T_{max} . In our simulations, we used 4 different simulation setups, as listed in Table B.10.

line 5 Initialisation of all variables is done as specified in Table B.9.

line 6 In this line we set $\tau = 1.0$. This is used as the final simulation time for the first simulation of the subcellular VEGF-Delta-Notch system, i.e. for the initial phenotype patterning. Initial pattern stabilisation from a uniform configuration set in the initialisation takes longer than when a pre-pattern exists and only several cells change their positions. Thus a value of 1.0 was chosen as a value sufficiently larger than a typical time step for a migration event (defined in *line 8*).

line 8 The subcellular VEGF-Delta-Notch system is simulated using the Next Subvolume (NSV) method with the final time given by the time step of the last migration transition, τ (except for the first iteration step in which we use $\tau = 1.0$).

Algorithm 1. Pseudocode algorithm of multiscale model simulations.

- 1: Specify simulation setup.
- 2: Nullify the realisation counter, $count_R = 0$.
- 3: **while** $count_R < N_R$ **do**
- 4: $count_R = count_R + 1$.
- 5: Initialisation.
- 6: Set $t = 0$, $\tau = 1.0$.
- 7: **while** $t < T_{max}$ **do**
- 8: Obtain \mathcal{C}^s by simulating the subcellular VEGF-Delta-Notch multicellular system with the final simulation time, τ .
- 9: Given \mathcal{C}^c , compute migration transition rates, $\omega(i \rightarrow j)$, (see Eq (2.7) of the main text) for all $i, j \in \mathcal{I}$.
- 10: Sample waiting times for each transition from the exponential distribution with the intensity given by the corresponding transition rate, $\tau_{ij} = \text{Exp}(\omega(i \rightarrow j))$, for all $i, j \in \mathcal{I}$ such that $\omega(i \rightarrow j) > 0$.
- 11: Find the migration event with the minimum waiting time: $\tau = \tau_{\bar{i}\bar{j}} = \min_{i,j} \tau_{ij}$. Set the jump direction vector, $s = h^{-1}(q_{\bar{j}} - q_{\bar{i}})$, where h is the voxel width.
- 12: Perform the migration event: $\text{swap}(E_{\bar{i}}, E_{\bar{j}})$ and $\text{swap}(\mathcal{C}_{\bar{i}}^s, \mathcal{C}_{\bar{j}}^s)$.
- 13: Update the orientation landscape due to traction forces generated by the migration event according to Eq (2.16) (of the main text) with $i = \bar{i}$ and $j = \bar{j}$ and the migration direction, s .
- 14: Do a general update of the tissue scale variables with the final time, τ : fibrils relaxation, \mathbf{l} , (Eq (2.17) of the main text); ECM concentration, \mathbf{c} , (Eqs (2.18)-(2.19) of the main text); BM component concentration, \mathbf{m} , (Eqs (2.20)-(2.21) of the main text).
- 15: Increment the simulation time: $t = t + \tau$.
- 16: [Optional] Calculate statistics.
- 17: **end while**
- 18: [Optional] Post-processing and statistical analysis.
- 19: End of the current realisation.
- 20: **end while**
- 21: End of simulation.

line 10 An equivalent procedure to sample a number, x , from the Poisson distribution with intensity λ is $x = \lceil \lambda \log(1/\text{Unif}[0,1]) \rceil$, where $\text{Unif}[0,1]$ is the uniform distribution on $[0, 1]$.

line 12 The swapping events account for both a simple migration event, when the destination voxel v_j is free and the cell from voxel v_i is just put in a new position (voxel v_j), and a switching event, when the destination voxel v_j is occupied and cells exchange their positions (the values of the subcellular scale).

B.4 Next Subvolume (NSV) method

The Next Subvolume (NSV) method is one of the modifications of the standard Stochastic Simulation Algorithm (SSA) [65], introduced in [64]. For reaction-diffusion systems, it is more efficient than the SSA since the computational effort grows as the logarithm of the number of voxels (subvolumes in 3D) instead of the linear dependency exhibited by the SSA.

In the SSA the time step for the next reaction to occur is generated from the Poisson distribution with the intensity equal to the total propensity for all voxels in the system. Then the reaction is chosen probabilistically according to the weight given by the local (for each voxel separately) propensities of each reaction. A major advantage of the NSV method is that time steps for the next reaction are generated for each voxel separately and stored in a sorted way according to the next time for a reaction to occur. Implementation of this algorithm is usually done by utilising a data structure called “priority queue” for which many efficient algorithms exist. This decreases the overall complexity of the simulating algorithm from linear (for the SSA) to logarithmic (for the NSV method) of the total number of voxels.

B.5 Metric definitions

Here we provide more details on definitions of and computational algorithms for the metrics used for model calibration. Firstly, we recall some of the notation used in the main text.

\mathcal{I}	Total set of voxel indices.
v_i	A voxel indexed by $i \in \mathcal{I}$.
$\mathbf{E} = (E_1, \dots, E_{N_I})$	Distribution of cell nuclei. Here N_I denotes cardinal of \mathcal{I} .
T_{max}	Final simulation time in a single realization of our model.
ι	A cell label.

We introduce a partitioning of a simulation time interval $[0, T_{max}]$ with a uniform step Δ as follows:

$$\mathcal{T}(\Delta) = \left\{ t_k = \Delta k, k = 0, \dots, K, K = \left\lfloor \frac{T_{max}}{\Delta} \right\rfloor \right\}, \quad (\text{B.10})$$

where $\lfloor x \rfloor$ denotes the largest integer less than or equal to $x \in \mathbb{R}$.

The pseudocode algorithms shown below should be considered as complementary to the general algorithm of multiscale simulations, Algorithm 1.

We also note that since the simulations we perform are stochastic, the statistic corresponding to $t_k \in \mathcal{T}(\Delta)$ is calculated at time \bar{t} such that $t < t_k < \bar{t}$, where t and \bar{t} are time moments corresponding to two consecutive times of migration events at the cellular scale of the multiscale simulation.

Displacement The displacement statistic characterises the average displacement a cell makes in Δ_{disp} time. In our simulations, Δ_{disp} is taken such that it corresponds to 15 minutes, in order to be able to compare to the data in [10]. However, in general, Δ_{disp} can be chosen arbitrary.

The general algorithm to compute this statistic is given in Algorithm 2. Therein, the concatenation operator, $\cdot \vee \cdot$, is defined as $v^1 \vee v^2 = (v_1^1, \dots, v_{N_1}^1, v_1^2, \dots, v_{N_2}^2)$ for vectors $v^1 = (v_1^1, \dots, v_{N_1}^1)$ and $v^2 = (v_1^2, \dots, v_{N_2}^2)$.

Algorithm 2. Pseudocode algorithm for computing the displacement statistic.

- 1: Specify the length of the displacement interval, Δ_{disp} .
- 2: Create an empty vector of displacements, $V_{disp} = \emptyset$.
- 3: **for** each realisation **do**
- 4: Nullify the simulation time, $t = 0$.
- 5: $k = 1$.
- 6: $V^1 = (0, \dots, 0) \in \mathbb{R}^{max_cell}$, where $max_cell = \sum_{i \in \mathcal{I}} E_i(t)$.
- 7: **while** $t < T_{max}$ **do**
- 8: Obtain time step, τ , for the next migration event, $\omega(i \rightarrow j)$, (see Algorithm 1).
- 9: Identify labels of cells whose nuclei are in voxels v_i and v_j , ι_i and ι_j , respectively, (if $E_j(t) = 0$, i.e. v_j is empty, then only ι_i).
- 10: Increment the components of the displacement vector, corresponding to the labels of migrating cells, $V_{\iota_i}^k = V_{\iota_i}^k + h$ and $V_{\iota_j}^k = V_{\iota_j}^k + h$, where h is the voxel width (if $E_j(t) = 0$, i.e. v_j is empty, then only increment $V_{\iota_i}^k$).
- 11: $t = t + \tau$.
- 12: **if** $t > \Delta_{disp}k$ **then**
- 13: $V_{disp} = V_{disp} \cup V^k$.
- 14: $k = k + 1$.
- 15: $V^k = (0, \dots, 0) \in \mathbb{R}^{max_cell}$, where $max_cell = \sum_{i \in \mathcal{I}} E_i(t)$.
- 16: **end if**
- 17: **end while**
- 18: **end for**
- 19: The output vector, V_{disp} , is a sample of cell displacements during all time intervals of length Δ_{disp} for all cells in all realisations. We use it to compute a probability density function of displacement in Δ_{disp} time (as in Figure 2.10A of the main text).

Orientation This statistic is used to characterise persistence of cell migration. The following procedure is used for its computation.

Each individual cell in a single realisation is associated with a label, ι . We record its

trajectory within the lattice during the simulation, $p(\iota, t) \in \mathbb{R}^2$, where $t \in [0, T_{max}]$.

Each $p(\iota, t)$ (or any sample extracted from it) is a polygonal chain, since cells perform jumps at discrete time moments and are assumed to be motionless between them. We define the length of a polygonal chain $p(\iota, t)$ given the time partitioning, \mathcal{T}_ι , as follows

$$l(p(\iota, t) | \mathcal{T}_\iota) = \sum_k \|p(\iota, t_{k+1}) - p(\iota, t_k)\|, \quad t_k \in \mathcal{T}_\iota.$$

Here $\|\cdot\|$ is the Euclidean norm in \mathbb{R}^2 .

We denote by $\mathcal{T}_\iota^r = \{t_k\}_k$ the ascending sequence of time moments of migration events of the cell with label ι . Thus, \mathcal{T}_ι^r defines the real trajectory of the cell ι (see Figure B.5A).

We also define a partitioning of the simulation time interval, defining the smoothed trajectory (see Figure B.5B), as $\mathcal{T}_\iota^s = \mathcal{T}(\Delta_{orient})$ (using Eq (B.10)), where Δ_{orient} is a uniform time step. In order to be able to compare our simulation results with experimental data from [4], Δ_{orient} was chosen such that it corresponds to 20 minutes. However, in general, Δ_{orient} can be arbitrary provided that it is greater than a typical waiting time between migration events in our multiscale simulation algorithm.

Then the orientation quantity, O_ι , is defined as

$$O_\iota = \frac{l(p(\iota, t) | \mathcal{T}_\iota^s)}{l(p(\iota, t) | \mathcal{T}_\iota^r)}.$$

When O_ι is close to 1.0, the cell ι is characterised as persistent. Lower values of O_ι correspond to trajectories in which cells performed many backward jumps (in the direction opposite to the elongation direction of a sprout).

The quantities O_ι are computed for each individual cell in each realisation. The overall sample of these quantities is used to produce box plots of the type shown in Figure 2.10C of the main text.

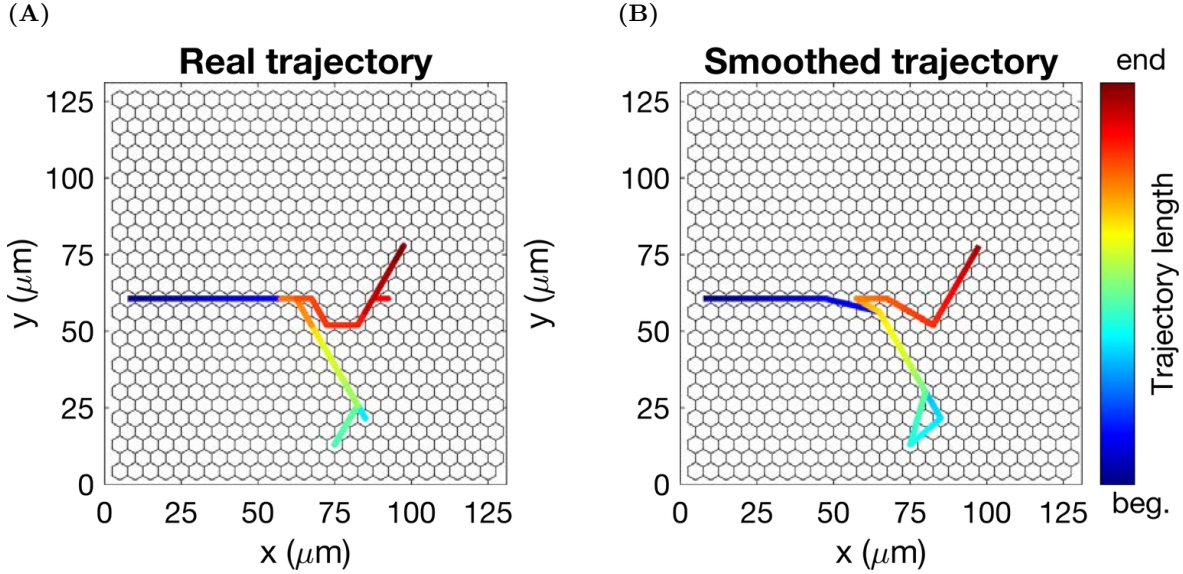


Figure B.5. Illustrations of real and smoothed trajectories for an individual cell in a single realisation. (A) Unmodified (real) trajectory of an individual cell with a label, ι , in a single realisation, $p(\iota, t)$, $t \in [0, T_{max}]$. (B) The smoothed trajectory is obtained from the real trajectory, $p(\iota, t)$, by extracting a sample $p(\iota, t_k)$ such that $t_{k+1} - t_k \approx \Delta_{orient}$. The colourbar indicates the trajectory length.

Directionality The directionality statistic provides a breakdown of migration events by their direction with respect to the direction of sprout elongation. We account for three types of movement: anterograde, retrograde and no movement (still). Since in our simulations ECs polarise according to the alignment of ECM fibrils (orientation landscape variable) which defines the direction of sprout elongation, any movement of a cell from the voxel of origin is considered anterograde. In contrast, if there is a cell in the voxel of destination of the migration event, then this cell is overtaken and is displaced to the voxel of origin. Thus, this is a retrograde movement. To define cells that stay still, we introduce a parameter, Δ_{still} . A cell is assumed to be still if it has not moved in Δ_{still} time (in our simulations this parameter corresponds to 20 minutes). A pseudocode for computing the directionality statistic is shown in Algorithm 3.

Algorithm 3. Pseudocode algorithm for computing the directionality statistic.

- 1: Specify length of a time interval to define ‘no movement’ events, Δ_{still} .
- 2: Introduce counters for anterograde movement, $count_a = 0$, retrograde movement, $count_r = 0$, and ‘no movement’ events, $count_s = 0$.
- 3: **for** each realisation **do**
- 4: Nullify the simulation time, $t = 0$.
- 5: Create an empty array, $A = \emptyset$, to record labels of cells which moved during Δ_{still} .
- 6: $k = 1$.
- 7: **while** $t < T_{max}$ **do**
- 8: Obtain time step, τ , for the next migration event, $\omega(i \rightarrow j)$, (see Algorithm 1).
- 9: Identify labels of cells whose nuclei are in voxels v_i and v_j , ι_i and ι_j , respectively, (if $E_j(t) = 0$, i.e. v_j is empty, then only ι_i).
- 10: $count_a = count_a + 1$.
- 11: $A = A \cup \{\iota_i\}$.
- 12: **if** $E_j(t) = 1$ **then**
- 13: $count_r = count_r + 1$.
- 14: $A = A \cup \{\iota_j\}$.
- 15: **end if**
- 16: Perform the migration event.
- 17: $t = t + \tau$.
- 18: **if** $t > \Delta_{still}k$ **then**
- 19: $count_s = count_s + (max_cell - \text{Size}(\text{Unique}(A)))$, where $max_cell = \sum_{i \in \mathcal{I}} E_i(t)$.
- 20: $A = \emptyset$.
- 21: $k = k + 1$.
- 22: **end if**
- 23: **end while**
- 24: **end for**
- 25: The output is given by three counters for each type of cell movement: $count_a$, $count_r$ and $count_s$, which we use to make histograms of the directionality statistic (as in Figure 2.10E of the main text).

In Algorithm 3, the routine $\text{Unique}(\cdot)$ returns an array of unique cell labels in a given set; the routine $\text{Size}(\cdot)$ returns the cardinal of a given set.

Tip cell proportion This metric, $\mathcal{R}_{tips}(t)$, is defined as the ratio of cells with tip cell phenotype to the total number of cells in the system at a predetermined time, t . To compute its average over a number of realisations, we define a partitioning of the simulation time interval, $\mathcal{T}_{tips} = \mathcal{T}(\Delta_{tips})$, where Δ_{tips} is a uniform partitioning step.

We recall that we use the parameter characterising the baseline gene expression of Delta, b_D , as a threshold to define a cell's phenotype (see Eq (2.3) in the main text). Thus, $\mathcal{R}_{tips}(t)$ in a single realisation is computed as follows:

$$\mathcal{R}_{tips}(t) = \frac{\text{Number of tip cells}}{\text{Total number of cells}} = \frac{\sum_{i \in \mathcal{I}: D_i(t) \geq b_D} E_i(t)}{\sum_{i \in \mathcal{I}} E_i(t)}. \quad (\text{B.11})$$

The pseudocode for computing the tip cell proportion statistic, $\mathcal{R}_{tips}(t)$, is shown in Algorithm 4.

Algorithm 4. Pseudocode algorithm for computing the tip cell proportion statistic.

- 1: Specify the partitioning of the time interval, \mathcal{T}_{tips} .
- 2: Nullify the realisation counter, $r = 0$.
- 3: **while** $r < N_R$ **do**
- 4: $r = r + 1$.
- 5: Nullify the simulation time, $t = 0$.
- 6: Set $k = 0$.
- 7: **while** $t < T_{max}$ **do**
- 8: Obtain time step, τ , for the next migration event (see Algorithm 1).
- 9: **if** $t < t_k < t + \tau$ **then**
- 10: Compute $\mathcal{R}_{tips}^r(t_k)$ as in Eq (B.11).
- 11: $k = k + 1$.
- 12: **end if**
- 13: **end while**
- 14: **end while**
- 15: Average the statistic over the performed realisations, $\mathcal{R}_{tips}(t_k) = \frac{1}{N_R} \sum_{r=0}^{N_R} \mathcal{R}_{tips}^r(t_k)$,
for each $k = 0, \dots, K$.

B.6 Mixing measure

A general definition of the mixing measure, $\mathcal{M}(t)$, is given by Eqs (2.22)-(2.23) of the main text (see also Figure 2.6 of the main text for an illustration). In order to fully determine $\mathcal{M}(t)$, we need to specify the distance function, $d(\cdot, \cdot, \cdot)$. Since ECs migrate within empty sleeves of vascular guidance tunnels created due to ECM proteolysis [32], we convert the simulated network into a directed graph based on the configuration of the ECM-free tunnels (defines the set of graph vertices) and the ECM fibril orientation (defines the set of edges). Pairwise distances between cells are thus computed as the shortest possible paths within the graph. Specifically, we use the classical Dijkstra algorithm with Manhattan distance function [222]. Likewise, the maximum distance, d_{max} , used as a normalisation constant in Eq (2.22) of the main text, is the maximum Dijkstra distance in the generated graph.

We now proceed to provide a more detailed description of the numerical procedure used to convert a simulated vascular network into a graph, compute distances between the vertices of this graph, define a set of indices, $\mathcal{I}_{cluster}$, and compute the temporal evolution of the mixing measure in a single numerical realisation.

Generating a graph from a simulated network

The algorithm for converting a simulated vascular network into a directed graph, $\mathcal{G}(\mathcal{N}, \mathcal{E})$, is based on the following.

- I. After reaching the final simulation time, T_{max} , in a single realisation, we consider the final state of the distribution of ECM concentration, \mathbf{c} . Based on this quantity, we determine the voxels that were explored by cell migration (thus generating the vascular guidance tunnels). Initially $c_i(t = 0) = c_{max}$ for $i \in \mathcal{I} \setminus \mathcal{I}_{init}$ (see Table B.9). Since during cell migration the ECM is degraded (see Eqs (2.18)-(2.19) in the main text), voxels v_i , which have been visited by a cell are such that $c_i(t = T_{max}) < c_{max}$. This allows us to define the so-called explored network, \mathcal{N} , as a subset of voxel indices such

that

$$\mathcal{N} = \{i \in \mathcal{I} \text{ such that } c_i < c_{max}\}. \quad (\text{B.12})$$

The voxels with indices in \mathcal{N} constitute the set of vertices in the graph, $\mathcal{G}(\mathcal{N}, \mathcal{E})$, to be constructed. Instead of using 2D indices, for simplicity, we label them in an arbitrary order.

- II. To determine the set of edges, \mathcal{E} , we look at the configuration of the ECM fibril orientation, \mathbf{l} (orientation landscape (OL) variable). Vertices corresponding to the voxels v_i and v_j , $i, j \in \mathcal{N}$ are connected if the OL of voxel of origin, $l_i = \{l_i^{\bar{s}}\}_{\bar{s} \in \mathcal{S}}$, possesses a component $s \in \mathcal{S}$ greater than the initialisation value, Δ_{init} . Here s is a unit vector connecting the centres of v_i and v_j (see Figure B.6). The rationale for this rule is that this condition implies that the direction s has been explored by a migration event from voxel v_i to v_j during simulation (see Eq (2.16) in the main text). Mathematically, it reads

- (i) there is an edge e_{ij} , $i, j \in \mathcal{N}$ if $l_i^s > \Delta_{init}$, $s = h^{-1}(q_j - q_i) \in \mathcal{S}$.

In the example shown in Figure B.7, condition (i) is satisfied for the pairs of vertices with indices $1 \rightarrow 2$ and $3 \rightarrow 4$.

- III. In most simulated networks, we find sprouts of width of more than one cell (for example, as shown in Figure B.7A). To avoid infinite distances between first-neighbour voxels which belong to the same sprout and do not point towards each other but rather are aligned in the same direction, we connect these vertices if the corresponding voxels exhibit the same explored direction, \bar{s} . This reads as follows

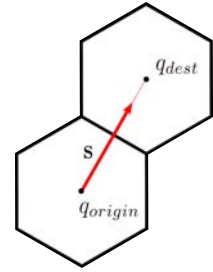


Figure B.6.
Illustration of the direction vector, s . $s = h^{-1}(q_{dest} - q_{origin})$, where $q_k \in \mathbb{R}^2$ denotes a vector of coordinates of the centre of a voxel with index k and h is the voxel width.

- (ii) there is an edge e_{ij} , $i, j \in \mathcal{N}$ if there exists $\bar{s} \in \mathcal{S}$ such that $l_i^{\bar{s}} > \Delta_{init}$ and $l_j^{\bar{s}} > \Delta_{init}$.

In Figure B.7A, voxels (vertices) 1 and 3 are neighbouring, but do not point towards each other. Nonetheless, in a generated graph (Figure B.7B) they are connected, since they both have explored the rightward OL direction ($\bar{s} = r$). The same argument holds for the pairs of vertices $2 \leftrightarrow 4$, $1 \leftrightarrow 4$, $2 \rightarrow 1$, $1 \rightarrow 3$ and $4 \rightarrow 3$.

IV. We assume that all edges of the graph have the same weight equal to unity.

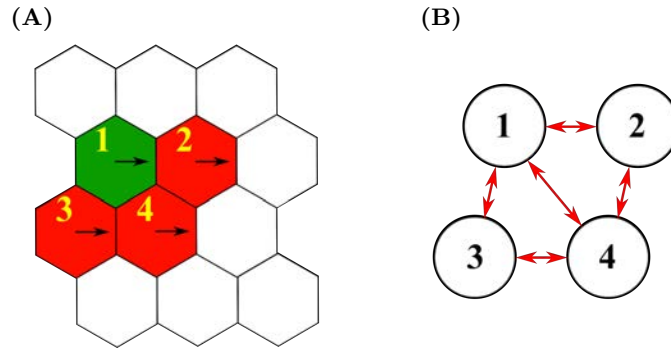


Figure B.7. (A) A simple example of a simulated network with $|\mathcal{N}| = 4$. The green colour corresponds to tip cell phenotype, red colour to stalk phenotype. Since there are cells in these voxels, the ECM concentration is less than c_{max} . Thus, these voxels form the explored network, \mathcal{N} (numbering is done in an arbitrary fashion). Explored OL variable directions are indicated by arrows. (B) The graph corresponding to the simulated network from (A).

We thus formulate a general algorithm, Algorithm 5, for converting a simulated vascular network into a graph.

We illustrate Algorithm 5 step by step with a simple example based on the small simulated vascular network in Figure B.8. The final configuration of the explored network is shown in Figure B.8A (explored vascular guidance tunnels with collagen concentration less than 1.0). The OL configuration is shown by arrows on this plot. The voxels corresponding to the explored network, \mathcal{N} , are then labelled by numbers in Figure B.8B. They form the set of

vertices of the graph. Applying Algorithm 5 to it, the simulated network is transformed into a graph (see Figure B.8C and B.8D, all edges are bidirectional).

Algorithm 5. Pseudocode algorithm to generate a graph from a simulated network.

```

1: function NETWORK TO GRAPH ( $\mathbf{c}, c_{max}, \mathbf{l}, \Delta_{init}, \mathcal{I}, \mathcal{S}$ )
2:   Create set of graph vertices  $\mathcal{N} \leftarrow \{i \in \mathcal{I} \text{ such that } c_i < c_{max}\}$  ▷ I.
3:   Create an empty set of edges  $\mathcal{E} \leftarrow \{ \}$ 
4:   for  $i \in \mathcal{N}$  do
5:     for  $s \in \mathcal{S}$  do
6:        $j \in \mathcal{I}$  such that  $q_j = q_i + hs$  ▷ Figure B.6
7:       if such  $j$  does not exist or  $j \notin \mathcal{N}$  then
8:         continue
9:       end if
10:      if there exists  $\bar{s} \in \mathcal{S}$  such that either  $[l_i^{\bar{s}} > \Delta_{init} \ \& \ \bar{s} = s]$ 
11:      or  $[l_i^{\bar{s}} > \Delta_{init} \ \& \ l_j^{\bar{s}} > \Delta_{init}]$  then
12:        Add an edge from vertex  $i$  to  $j$ ,  $e_{i,j}$ , to the set of edges  $\mathcal{E}$  ▷ II., III., Figure B.7
13:      end if
14:    end for
15:  end for
16:  Create a graph  $\mathcal{G}(\mathcal{N}, \mathcal{E})$  with all edge costs equal to 1 ▷ IV.
17:  return  $\mathcal{G}(\mathcal{N}, \mathcal{E})$ 
18: end function

```

Distances in a graph

The output of Algorithm 5 is an unweighted directed graph $\mathcal{G}(\mathcal{N}, \mathcal{E})$. We can use it to compute a matrix of shortest distances in a graph for each pair of vertices (i.e. explored voxels) in \mathcal{N} . To do so, we use the classical Dijkstra algorithm [222]. This algorithm takes as input a directional graph with non-negative edge weights (for example, the one shown in Figure B.8D) and computes a matrix of shortest paths between each pair of vertices, using edge costs. The distance of a path is calculated simply by adding up the weights of all edges constituting the path. Continuing with the example from Figure B.8, the matrix of shortest path distances for the graph from Figure B.8D is shown in Table B.5. The quantity d_{max} in

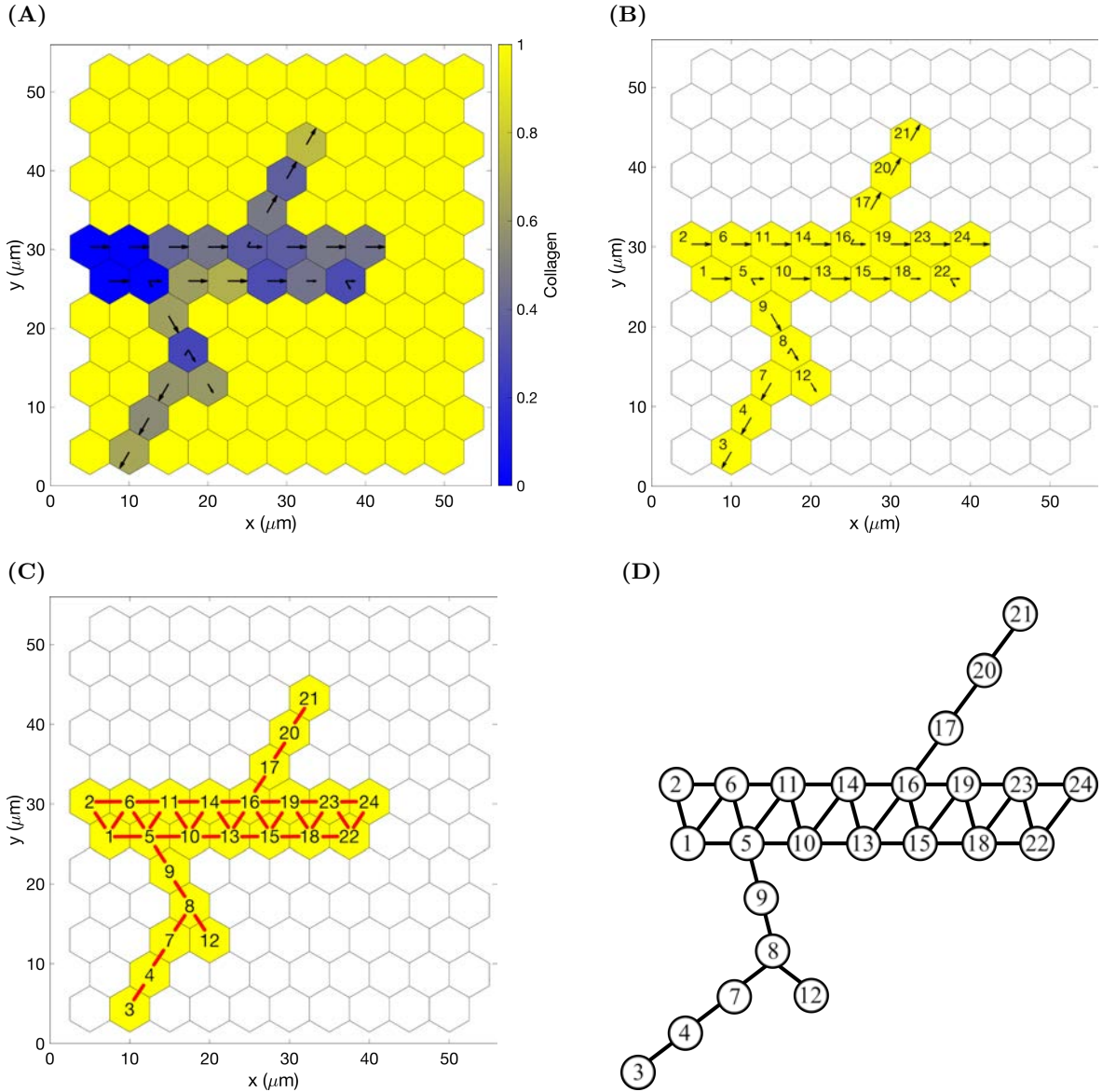


Figure B.8. An example of converting a simulated network into a graph. **(A)** The final configuration of the ECM concentration, c . Here $c_{max} = 1.0$, thus the explored network, \mathcal{N} , corresponds to all voxels v_i with $c_i < 1.0$. The colour bar indicates collagen concentration. Arrows correspond to the explored OL configuration (ECM fibril alignment). **(B)** Labelling (in an arbitrary fashion) the explored network, \mathcal{N} (see Eq (B.12)). Voxels, indices of which belong to it, are coloured in yellow. **(C)** Applying Algorithm 5 to generate a directed graph from the network. Edges between vertices are shown in red (all bidirectional). **(D)** The final graph (all edges are bidirectional, arrows are omitted for simplicity) that is provided as an input to the Dijkstra algorithm to compute shortest paths between graph vertices. All edges have equal weights of 1.

Eq (2.23) in the main text is then the maximum value in this matrix.

0	1	6	5	1	1	4	3	2	2	2	4	3	3	4	4	5	5	5	6	7	6	6	7
1	0	7	6	2	1	5	4	3	3	2	5	4	3	5	4	5	6	5	6	7	7	6	7
6	7	0	1	5	6	2	3	4	6	6	5	7	7	8	8	9	9	9	10	11	10	10	11
5	6	1	0	4	5	1	2	3	5	5	3	6	6	7	7	8	8	8	9	10	9	9	10
1	2	5	4	0	1	3	2	1	1	1	3	2	2	3	3	4	4	4	5	6	5	5	6
1	1	6	5	1	0	4	3	2	2	1	4	3	2	4	3	4	5	4	5	6	6	5	6
4	5	2	1	3	4	0	1	2	4	4	2	5	5	6	6	7	7	7	8	9	8	8	9
3	4	3	2	2	3	1	0	1	3	3	1	4	4	5	5	6	6	6	7	8	7	7	8
2	3	4	3	1	2	2	1	0	2	2	2	3	3	4	4	5	5	5	6	7	6	6	7
2	3	6	5	1	2	4	3	2	0	1	4	1	1	2	2	3	3	3	4	5	4	4	5
2	2	6	5	1	1	4	3	2	1	0	4	2	1	3	2	3	4	3	4	5	5	4	5
4	5	5	3	3	4	2	1	2	4	4	0	5	5	6	6	7	7	7	8	9	8	8	9
3	4	7	6	2	3	5	4	3	1	2	5	0	1	1	1	2	2	2	3	4	3	3	4
3	3	7	6	2	2	5	4	3	1	1	5	1	0	2	1	2	3	2	3	4	4	3	4
4	5	8	7	3	4	6	5	4	2	3	6	1	2	0	1	2	1	1	3	4	2	2	3
4	4	8	7	3	3	6	5	4	2	2	6	1	1	1	0	1	2	1	2	3	3	2	3
5	5	9	8	4	4	7	6	5	3	3	7	2	2	2	1	0	3	1	1	2	4	3	4
5	6	9	8	4	5	7	6	5	3	4	7	2	3	1	2	3	0	1	4	5	1	1	2
5	5	9	8	4	4	7	6	5	3	3	7	2	2	1	1	1	1	0	3	4	2	1	2
6	6	10	9	5	5	8	7	6	4	4	8	3	3	3	2	1	4	3	0	1	5	4	5
7	7	11	10	6	6	9	8	7	5	5	9	4	4	4	3	2	5	4	1	0	6	5	6
6	7	10	9	5	6	8	7	6	4	5	8	3	4	2	3	4	1	2	5	6	0	1	1
6	6	10	9	5	5	8	7	6	4	4	8	3	3	2	2	3	1	1	4	5	1	0	1
7	7	11	10	6	6	9	8	7	5	5	9	4	4	3	3	4	2	2	5	6	1	1	0

Table B.5. The matrix of lengths of shortest paths between each pair of vertices in the graph shown in Figure B.8D. Zero entries on the main diagonal indicate that there are no self-loops in the graph.

Using Algorithm 5 to generate a graph from the simulated network and the Dijkstra algorithm as a distance function between its vertices, we complete the definition of the mixing measure, $\mathcal{M}(t)$, Eq (2.22) of the main text.

Defining the time moments to compute the mixing statistic

To obtain the time evolution of the mixing measure averaged over a number of realisations, we need to partition the time interval of our simulations and compute $\mathcal{M}(\cdot)$ for each time instant belonging to the partition over all performed stochastic realisations. Two important issues need to be addressed:

- I. $\mathcal{M}(t)$ is calculated as a normalised difference between the distance among cells in the cluster at some time, t , and the distance between the same cells at later time $(t + t_m)$. Thus, if T_{max} is the final simulation time, then the last time moment for computing the mixing quantity is $(T_{max} - t_m)$.
- II. Our simulations are stochastic. Consequently, time steps of events are not known *a priori* but rather sampled during each individual realisation. If we decide to partition the simulation time in some predetermined way for all realisations, $\mathcal{T} = \left\{ \tau_k = \Delta_{mix} k, k = \overline{1, K}, K = \left\lfloor \frac{T_{max} - t_m}{\Delta_{mix}} \right\rfloor \right\}$ (where Δ_{mix} is a uniform partitioning step), then we will not be able to calculate the mixing quantity at *exactly that* time instant. The time steps of the stochastic simulations are usually much smaller than the chosen partitioning time step, Δ_{mix} . Therefore, if the current simulation time is t such that $t < \tau_k < T_{max} - t_m$ and next event will happen at time, \bar{t} , $\tau_k < \bar{t} < T_{max} - t_m$, then we compute the mixing measure at the time moment \bar{t} , i.e. as soon as the next partitioning time has been passed.

Defining the voxel cluster

The setup of the numerical simulations is such that we assume there is a set of voxel indices, \mathcal{I}_{VP} , corresponding to a vascular plexus from which the cells are migrating (see Appendix B.3). A Dirichlet boundary condition of a constant cell number is maintained at these voxels, i.e. if a cell migrates from one of these voxels, a new one immediately appears. Thus, choosing $\mathcal{I}_{VP} \subset \mathcal{I}_{cluster}$ guarantees that there are always cells present in these voxels, and

the mixing measure makes sense at all times. However, $\mathcal{I}_{cluster}$ can be any set of indices of the lattice. Choosing a random position for the voxel cluster might lead to a situation when there are no cells present at the cluster location and we cannot compute the mixing quantity. We set $C = |\mathcal{I}_{cluster}|$, predetermined cluster size. In the main text, $\mathcal{I}_{cluster} = \mathcal{I}_{init}$ (**Setup 1** from Table B.10) was used, thus $C = 4$.

Algorithm 6. Pseudocode algorithm for computing the mixing measure in a single stochastic realisation of the model.

- 1: Define predetermined partitioning of the time interval $\mathcal{T} = \{\tau_k\}_{k=1}^K$.
- 2: Create two empty arrays of size $K \times C$ to record cell indices, A_{id} , (see Figure B.9A) and their final positions, P , (see Figure B.9B) for each time moment of the partition \mathcal{T} .
- 3: Start stochastic simulation of the multiscale model. Let t denote the current simulation time.
- 4: Whenever simulation time $t > \tau_k$ for some k that has not been computed yet, record in A_{id} cell indices positioned at voxels with indexes $\mathcal{I}_{cluster}$, track positions of these cells and record their locations in the lattice at time $(t + t_m)$ and save them in the array P (in the corresponding k^{th} row).
- 5: When $t \geq T_{max}$ terminate the simulation.
- 6: Convert the final simulated network into a graph using Algorithm 5.
- 7: Compute the initial distance between cells in the cluster, d_{init} , that is the same for all k (since cells are taken from the same lattice locations, $\mathcal{I}_{cluster}$), using the generated graph and vertices corresponding to $\mathcal{I}_{cluster}$ voxels.
- 8: For each k in $\overline{1, K}$, compute the sum of the pair-wise distances in the graph between cells with indices from the k^{th} row of A_{id} taking their recorded final locations from the k^{th} row of the array P . Denote this quantity as d_k .
- 9: Find the distance of the longest path in the graph, d_{max} , as the maximum entry in the matrix of Dijkstra shortest paths.
- 10: Compute the mixing quantity for each k in $\overline{1, K}$ using Eq (2.22) of the main text which, in the notation of this algorithm, corresponds to $m_k = \frac{d_k - d_{init}}{C d_{max}}$.
- 11: Record in the output file the mixing quantities, m_k , for all $k = \overline{1, K}$.

Whenever we decide to compute the mixing measure, we look at the labels of the cells located in the voxels in $\mathcal{I}_{cluster}$. We then track position of these cells and compute the mixing quantity using Eqs (2.22)-(2.23) in the main text. $\mathcal{I}_{cluster}$ is fixed over all performed realisations, whereas labels of cells positioned in it for each desirable time moment change.

Mixing measure

In Algorithm 6 we lay out the general procedure for computing $\mathcal{M}(t)$ for a single realisation. The mixing statistic is computed as a mean value of the mixing quantities for each moment of the time partition, \mathcal{T} , over all performed realisations.

B.7 Quantification of simulated vascular networks

To quantify in a rigorous way the branching structure of simulated vascular networks, we developed an algorithm to extract:

- vascular network area;
- number of branching points per $100 \mu m^2$ area of vascular network;
- number of vessel segments;
- length of vessel segments.

We define a *vessel segment* as either a part of vascular network between two branching points or free sprouts, i.e. between a branching point and the leading edge of this sprout.

The orientation landscape variable and graph representation of the simulated network used to compute the mixing measure give us a direct way to perform vascular network quantification. Briefly, starting with the graph representation given by Algorithm 5 (see Figure B.10B), we reduce sprouts of width of more than one voxel to single-voxel sprouts. This gives us the ‘skeleton’ of the vascular network (see Figure B.10C). From this representation, it is straightforward to identify *branching points* as all vertices of degree greater than 2 and *vessel segments* are obtained by splitting the skeleton graph at the vertices of branching points (see Figure B.10D). We lay out the general procedure for extracting these statistics in Algorithm 7.

(A)

$$C = |\mathcal{I}_{cluster}| = |\{i_1, i_2, \dots, i_C\}|$$

K	$\underbrace{\hspace{15em}}$			
	The index of a cell located at the voxel v_{i_1} , $i_1 \in \mathcal{I}_{cluster}$, at time τ_1 .	The index of a cell located at the voxel v_{i_2} , $i_2 \in \mathcal{I}_{cluster}$, at time τ_1	The index of a cell located at the voxel v_{i_C} , $i_C \in \mathcal{I}_{cluster}$, at time τ_1 .
	The index of a cell located at the voxel v_{i_1} , $i_1 \in \mathcal{I}_{cluster}$, at time τ_2 .	The index of a cell located at the voxel v_{i_2} , $i_2 \in \mathcal{I}_{cluster}$, at time τ_2	The index of a cell located at the voxel v_{i_C} , $i_C \in \mathcal{I}_{cluster}$, at time τ_2 .

	The index of a cell located at the voxel v_{i_1} , $i_1 \in \mathcal{I}_{cluster}$, at time τ_K .	The index of a cell located at the voxel v_{i_2} , $i_2 \in \mathcal{I}_{cluster}$, at time τ_K	The index of a cell located at the voxel v_{i_C} , $i_C \in \mathcal{I}_{cluster}$, at time τ_K .

(B)

$$C = |\mathcal{I}_{cluster}| = |\{i_1, i_2, \dots, i_C\}|$$

K	$\underbrace{\hspace{15em}}$			
	The index of a cell located at the voxel v_{i_1} , $i_1 \in \mathcal{I}_{cluster}$, at time τ_1 .	The index of a cell located at the voxel v_{i_2} , $i_2 \in \mathcal{I}_{cluster}$, at time τ_1	The index of a cell located at the voxel v_{i_C} , $i_C \in \mathcal{I}_{cluster}$, at time τ_1 .
	The index of a cell located at the voxel v_{i_1} , $i_1 \in \mathcal{I}_{cluster}$, at time τ_2 .	The index of a cell located at the voxel v_{i_2} , $i_2 \in \mathcal{I}_{cluster}$, at time τ_2	The index of a cell located at the voxel v_{i_C} , $i_C \in \mathcal{I}_{cluster}$, at time τ_2 .

	The index of a cell located at the voxel v_{i_1} , $i_1 \in \mathcal{I}_{cluster}$, at time τ_K .	The index of a cell located at the voxel v_{i_2} , $i_2 \in \mathcal{I}_{cluster}$, at time τ_K	The index of a cell located at the voxel v_{i_C} , $i_C \in \mathcal{I}_{cluster}$, at time τ_K .

Figure B.9. Array structures used in Algorithm 6. (A) A schematic of the structure of the array of cell indices, A_{id} . (B) A schematic of the structure of the array of final cell positions, P .

Algorithm 7. Pseudocode algorithm for extracting network quantification statistics in a single stochastic realization of the model.

- 1: Get graph representation of the vascular network, $\mathcal{G}(\mathcal{N}, \mathcal{E})$, from Algorithm 5.
- 2: Define a graph of the network skeleton, $\mathcal{G}_s(\mathcal{N}_s, \mathcal{E}_s) = \mathcal{G}(\mathcal{N}, \mathcal{E})$.
- 3: *Network area*, A , is equal to the number of vertices in the graph \mathcal{G}_s , $|\mathcal{N}_s|$, multiplied by the area of a single voxel ($0.5\sqrt{3}h^2$, in case of hexagonal voxel of width h [μm]).
- 4: Create an empty set of pairs of vertices of \mathcal{G}_s to be merged, \mathcal{N}_{merge} .
- 5: **for** $i \in \mathcal{N}$ **do**
- 6: **for** $s \in \mathcal{S}$ **do**
- 7: $j \in \mathcal{I}$ such that $q_j = q_i + hs$ ▷ Figure B.6
- 8: **if** such j does not exist or $j \notin \mathcal{N}$ **then**
- 9: **continue**
- 10: **end if**
- 11: **if** there exists $\bar{s} \in \mathcal{S}$ such that $[l_i^{\bar{s}} > \Delta_{init} \ \& \ l_j^{\bar{s}} > \Delta_{init}]$ **then**
- 12: Add the pair of vertices (i, j) to the set \mathcal{N}_{merge}
- 13: **end if**
- 14: **end for**
- 15: **end for**
- 16: **for** $(i, j) \in \mathcal{N}_{merge}$ **do**
- 17: Merge vertex i with vertex j , i.e. delete from \mathcal{E}_s the edges $e_{i,j}$ and $e_{j,i}$ and all edges of type $e_{j,\cdot}$ ($e_{\cdot,j}$) become $e_{i,\cdot}$ ($e_{\cdot,i}$).
- 18: **end for**
- 19: Delete all vertices of degree 0 from \mathcal{N}_s .
- 20: Delete repeated edges in $\mathcal{G}_s(\mathcal{N}_s, \mathcal{E}_s)$.
- 21: Identify *branching points* as the set of vertices of degree greater than 2,

$$\mathcal{N}_{branch} = \{i \in \mathcal{N}_s \text{ s.t. } deg(i) > 2\}.$$
 ▷ Figure B.10C
- 22: *Number of branching points per 100 μm^2 of vascular network area*, $N_b = \frac{|\mathcal{N}_{branch}| \cdot 100 \mu\text{m}^2}{A}$.
- 23: The graph of vessel segments, $\mathcal{G}_{vessels}$, is obtained from \mathcal{G}_s by duplicating each vertex in \mathcal{N}_{branch} by its degree and splitting the graph, \mathcal{G}_s , at these points. ▷ Figure B.10D
- 24: *Number of vessel segments* is given by the number of connected components in the graph $\mathcal{G}_{vessels}$.
- 25: *Vessel segment lengths* are given by the number of edges in each connected component of $\mathcal{G}_{vessels}$ multiplied by the voxel width, h [μm].

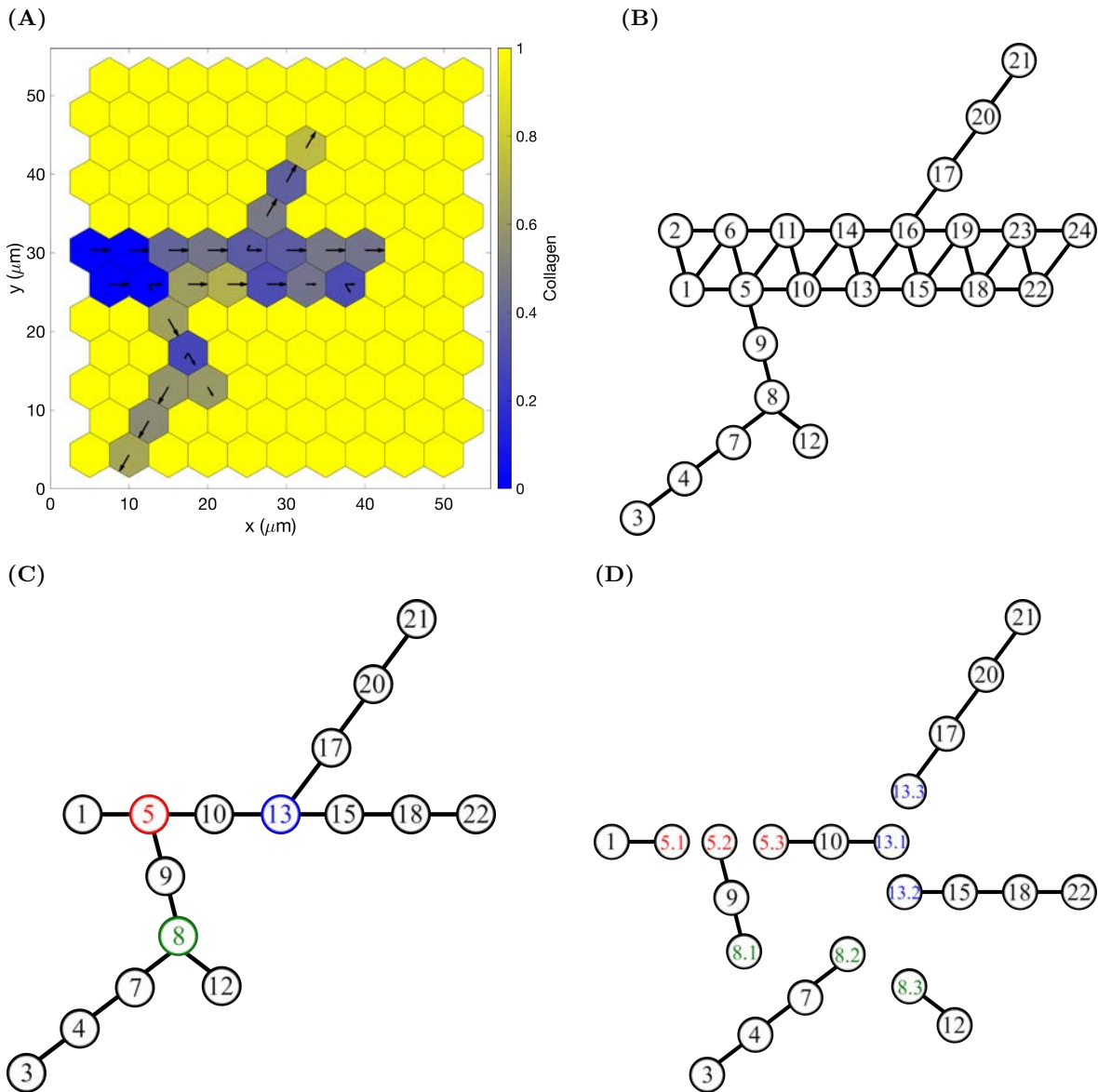


Figure B.10. An example of branching structure quantification on a single simulated vascular network. (A) The final configuration of the ECM concentration, c , of a simulated vascular network. Arrows correspond to the explored OL configuration (ECM fibril alignment). (B) The graph representation of the vascular network from (A) obtained by applying to it Algorithm 5. (C) Vascular network ‘skeleton’, \mathcal{G}_s , obtained by reducing multiple-voxel vessels to single-voxel sprouts (see Algorithm 7). Branching points (defined as vertices of degree greater than 2) are highlighted by a different colour. (D) Splitting the network ‘skeleton’ at the branching points to obtain vessel segments graph, $\mathcal{G}_{vessels}$ (see Algorithm 7).

B.8 Sensitivity analysis

Since our subcellular scale model was based on the previous works [153]–[156], we consider the parameters of this scale to be fixed (see Table B.7). By contrast, our implementation of cell migration and cell-ECM interactions is novel. Thus, we performed an extensive sensitivity analysis for the parameters corresponding to the cellular and tissue scales of our model (listed in Table B.8).

We define the set of baseline parameter values as:

$$\bar{p} = \{K, k_m, k_D, \eta_{max}, s_c, D_c, \gamma_{max}, s_m, D_m, p_{max}, s_p, D_p, E_{F1}, E_{F2}, s_{F1}, s_{F2}, R_c, D_\omega, \eta_l, c_{max}, a, \Delta_l\}.$$

Brief interpretations of these parameters and references to the corresponding equations are given in Table B.6. Baseline parameter values, calibrated by comparing our model to experimental data from [4], [10], [126], are listed in Table B.8.

Parameters	Interpretation	Reference
K, k_m, k_D	cell exploratoriness	Eq (2.14)
η_{max}, s_c, D_c	ECM proteolysis	Eqs (2.18)-(2.19)
γ_{max}, s_m, D_m	BM assembly	Eqs (2.20)-(2.21)
p_{max}, s_p, D_p	probability of cell overtaking	Eqs (2.10)-(2.11)
$E_{F1}, E_{F2}, s_{F1}, s_{F1}, s_{F2}$	cell-cell interaction	Eq (2.9)
R_c	cellular scale cell-cell interaction radius	Table 2.1, \mathbf{E}^N
D_ω	diffusion coefficient	Eq (2.7)
η_l	ECM relaxation rate	Eq (2.17)
c_{max}	maximum ECM concentration	Eq (2.8)
a	polarity vector parameter	Eq (2.13)
Δ_l	orientation landscape update increment	Eq (2.16)

Table B.6. Parameters of the cellular and tissue scales used for sensitivity analysis. Equation references are for the main text.

We define p_i as a vector of parameter values as in \bar{p} except for the parameter at position i which is incremented (or decremented) as indicated. For each of these parameter sets, we perform 100 realisations of our model using simulation **Setup 1** from Table B.10. The parameters of the subcellular scale are fixed for all experiments (see Table B.7). From these data we extract the following quantification metrics:

- anterograde cell proportion (directionality statistic);
- orientation;
- displacements;
- number of branching points per $100 \mu m^2$ of vascular network area;
- number of vessel segments;
- vessel segment lengths.

In order to compare these metrics for modified parameter sets, p_i , to the baseline parameters, \bar{p} , we compute:

- Kolmogorov-Smirnov statistic:

$$\mathcal{D}^* = \max_x | \hat{F}_{\bar{p}}(x) - \hat{F}_{p_i}(x) | .$$

Here $\hat{F}_{\bar{p}}(x)$ and $\hat{F}_{p_i}(x)$ are empirical cumulative distribution functions corresponding to the chosen metric for the sets of parameters \bar{p} and p_i , respectively. $\mathcal{D}^* \in [0, 1]$, where values close to 0 indicate that the corresponding cumulative distributions are similar and values close to 1 indicate that $\hat{F}_{\bar{p}}(x)$ and $\hat{F}_{p_i}(x)$ differ significantly.

- Relative mean change:

$$\frac{\mu_{p_i} - \mu_{\bar{p}}}{\mu_{\bar{p}}},$$

where μ_{p_i} and $\mu_{\bar{p}}$ are the mean values of the chosen metric for \bar{p} and p_i , respectively.

- Relative change of standard deviation:

$$\frac{\sigma_{p_i} - \sigma_{\bar{p}}}{\sigma_{\bar{p}}},$$

where σ_{p_i} and $\sigma_{\bar{p}}$ are the standard deviations of the chosen metric for \bar{p} and p_i , respectively.

We performed experiments for $\pm 0.1\%$, $\pm 1\%$, $\pm 5\%$, $\pm 5\%$, $\pm 10\%$, $\pm 15\%$ and $\pm 20\%$ change in the parameter values. The results for $\pm 10\%$ change are shown in Figures B.11-B.13 for the Kolmogorov-Smirnov statistic, relative change of mean and relative change of standard deviation, respectively. From these plots, it can be seen that cell behaviour (such as anterograde cell proportion, orientation of cell trajectory and cell displacements) and branching structure of the simulated networks (number of branching points, number and length of vessel segments) are affected the most by variations in parameters D_c and D_m characterising ECM proteolysis and BM deposition rates, respectively. Less significant change in the metrics is seen for cell exploratoriness parameters, K and k_D , and cell-cell adhesion parameters, E_{F1} and E_{F2} . We also note that individual cell behaviour is less affected than the overall vascular network structure.

The results of the sensitivity analysis for $\pm 10\%$ for the final value of mixing measure (the last value in the time evolution of the mixing measure extracted from the numerical simulations, $\mathcal{M}(t - t_m)$) are shown in Figure B.14. This metric is more robust than the metrics considered in Figures B.11-B.13. Interestingly, variations in majority of parameters (both positive and negative) induce a decrease in the final value of the mixing measure.

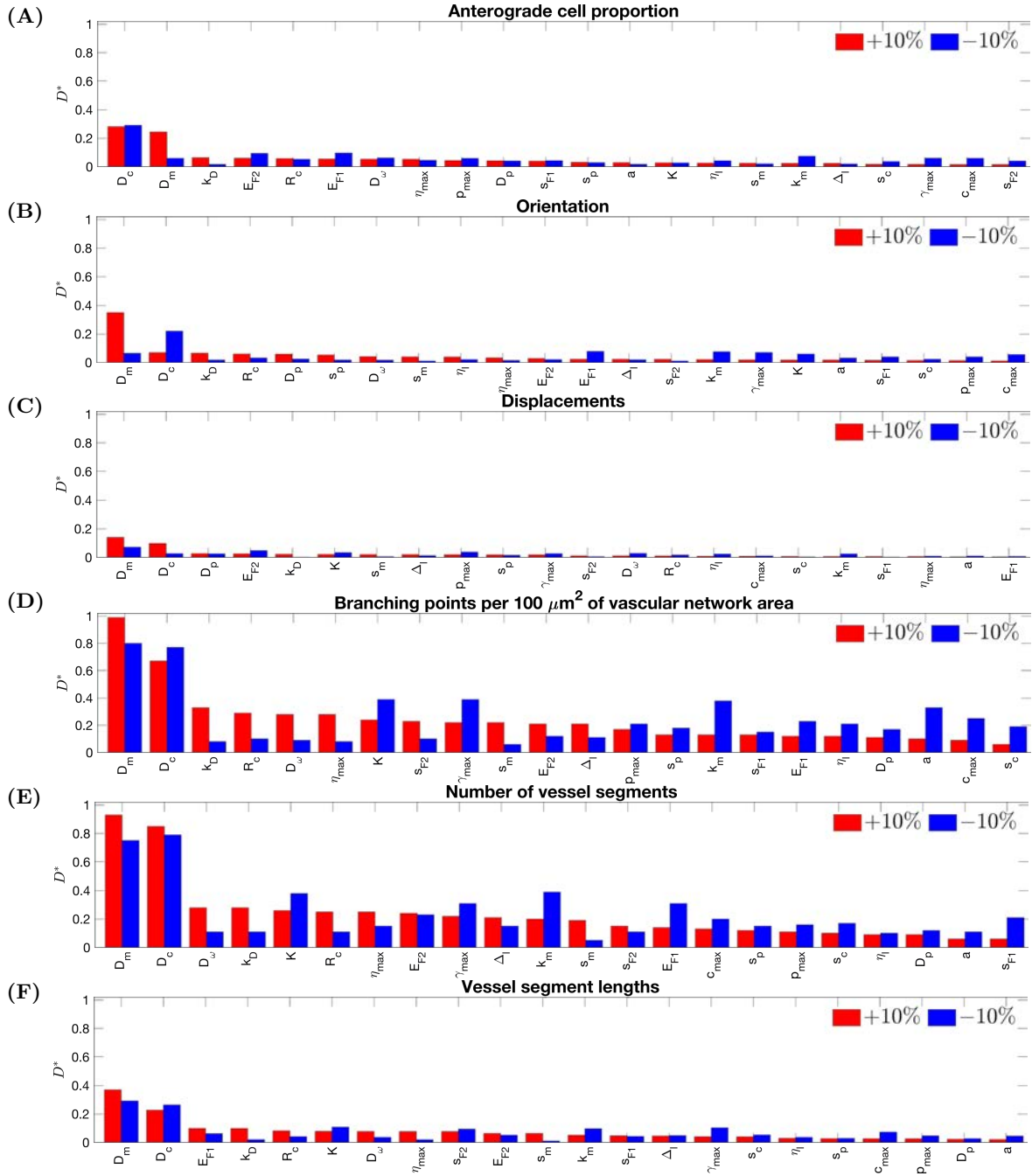


Figure B.11. Sensitivity analysis results for Kolmogorov-Smirnov distance for the following metrics: (A) anterograde cell proportion, (B) orientation, (C) displacements, (D) number of branching points per $100 \mu m^2$ of vascular network area, (E) number of vessel segments, (F) vessel segment lengths. Simulations were performed using **Setup 1** from Table B.10 and the parameter values as listed in Table B.8 except for the parameter indicated at Ox-axis which was incremented (decremented) by 10%. For each set of parameters 100 realisations were performed.

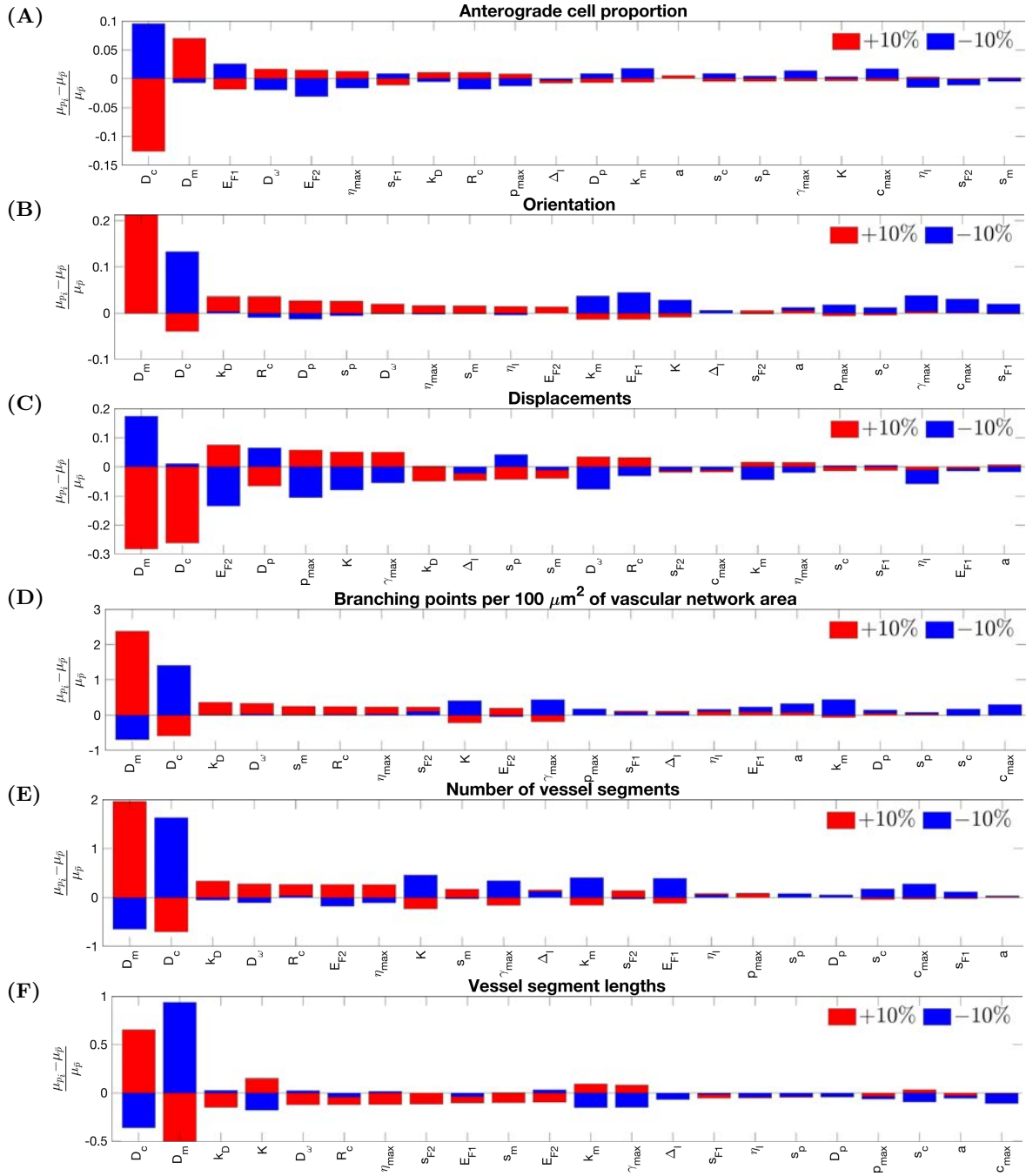


Figure B.12. Sensitivity analysis results for relative mean change for the following metrics: (A) anterograde cell proportion, (B) orientation, (C) displacements, (D) number of branching points per 100 μm^2 of vascular network area, (E) number of vessel segments, (F) vessel segment lengths. Simulations were performed using **Setup 1** from Table B.10 and the parameter values as listed in Table B.8 except for the parameter indicated at Ox-axis which was incremented (decremented) by 10%. For each set of parameters 100 realisations were performed.

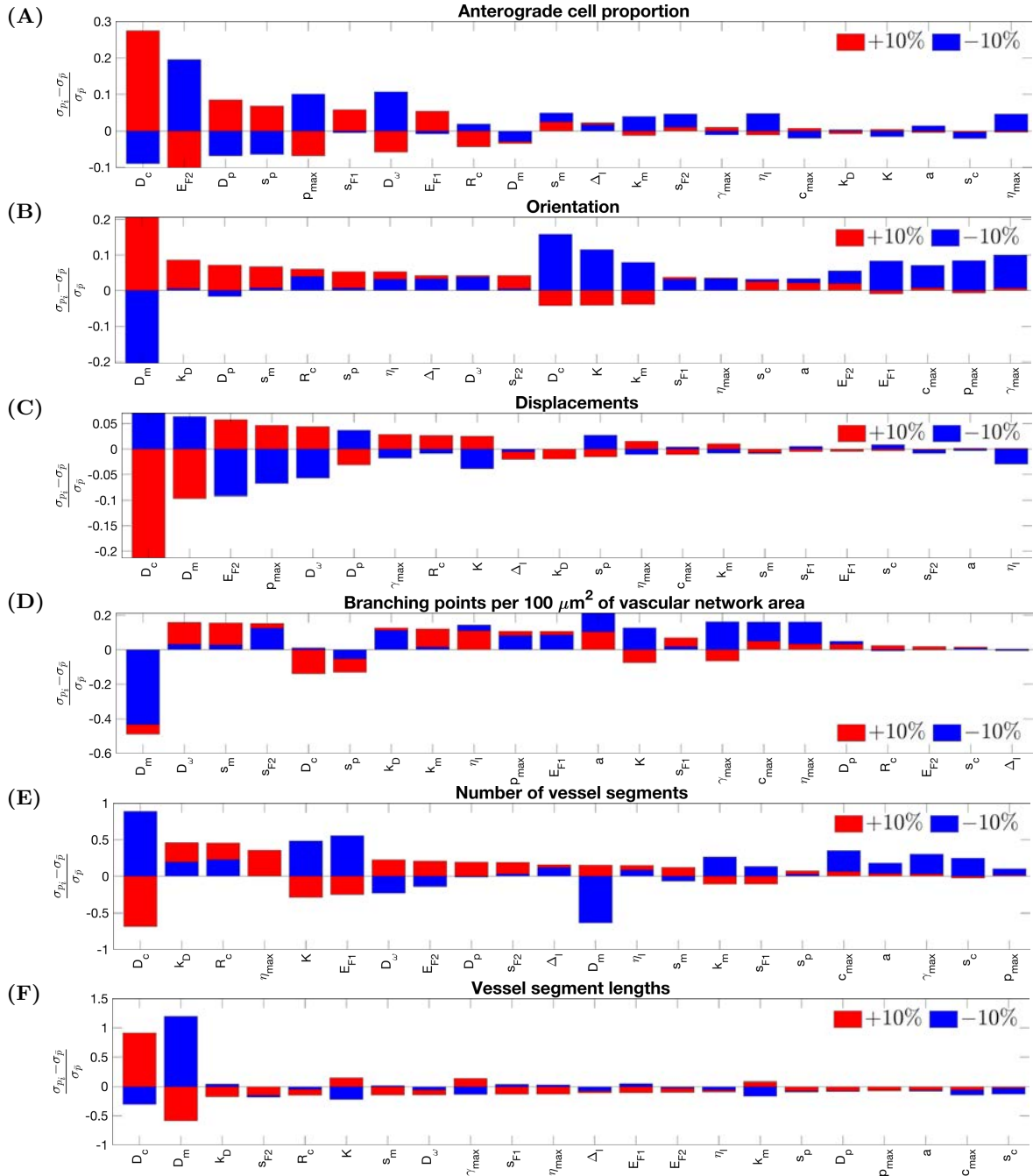


Figure B.13. Sensitivity analysis results for relative change of standard deviation for the following metrics: (A) anterograde cell proportion, (B) orientation, (C) displacements, (D) number of branching points per 100 μm^2 of vascular network area, (E) number of vessel segments, (F) vessel segment lengths. Simulations were performed using **Setup 1** from Table B.10 and the parameter values as listed in Table B.8 except for the parameter indicated at Ox-axis which was incremented (decremented) by 10%. For each set of parameters 100 realisations were performed.

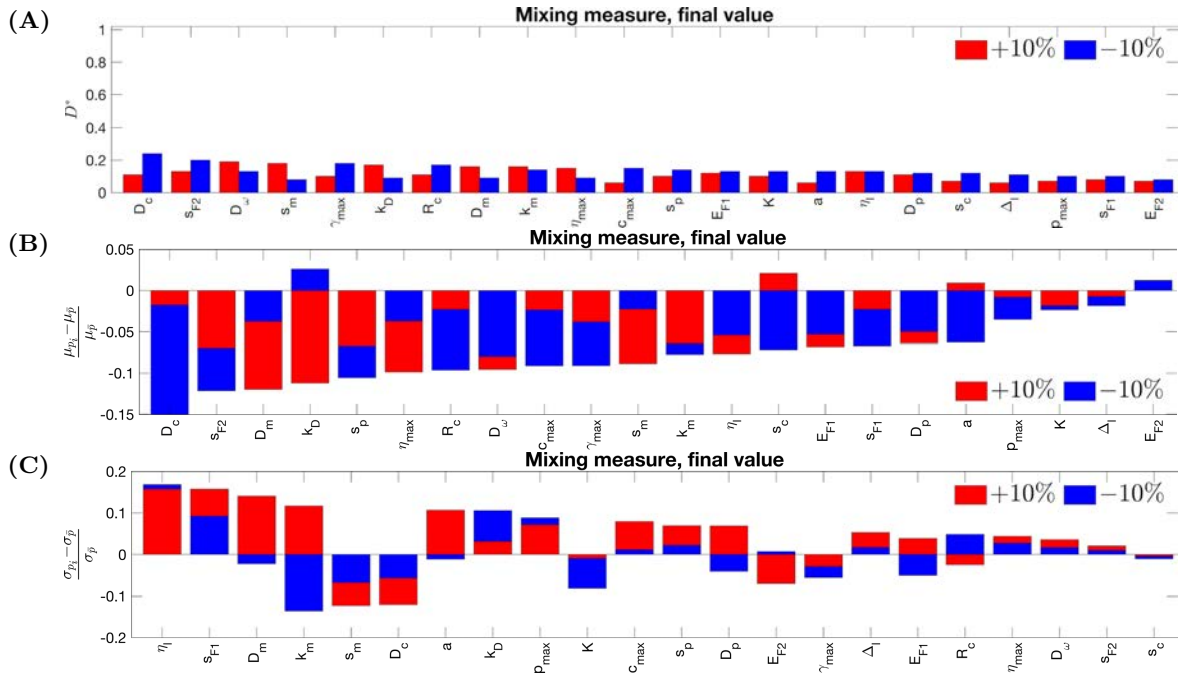


Figure B.14. Sensitivity analysis results for final value of mixing measure: (A) Kolmogorov-Smirnov distance, **(B)** relative mean change, **(C)** relative change of standard deviation. Simulations were performed using **Setup 1** from Table B.10 and the parameter values as listed in Table B.8 except for the parameter indicated at Ox-axis which was incremented (decremented) by 10%. For each set of parameters 100 realisations were performed.

B.9 Supplementary movies, figures and tables

Movie 2.1 An example of an individual vascular network generated by wild type ECs during simulation of our model with uniform VEGF = 50 ng/ml. The leftmost panel shows the concentration of Delta, D . The colour bar indicates level of Delta, D , (green colour corresponds to tip cells, red – to stalk cells). Arrows indicate the configuration of the orientation landscape, l . The central panel indicates the concentration of the ECM, c . The rightmost panel – the polarity angle, μ , variable. A circular colour bar indicates the value of μ . The simulation was performed using **Setup 1** from Table B.10 with final simulation time, $T_{max} = 2.5$. Parameter values are listed in Tables B.7 and B.8 for subcellular and cellular/tissue scales, respectively. The movie is available for download at https://github.com/daria-stepanova/PhD_thesis_supplementary_materials.

Movie 2.2 Cell migration from a cell bead in substrates of different collagen density. Single realisations of angiogenic sprouting from a cell bead in substrates of different collagen densities (reproducing the results of the polarisation experiment in [126]). Maximum collagen density (A) $c_{max} = 0.1$, (B) $c_{max} = 1.0$, (C) $c_{max} = 1.7$, (D) $c_{max} = 3.0$. The VEGF linear gradient starts with 0 ng/ml at $y = 0$ and increases up to 5 ng/ml at $y = 125 \mu m$. Central bead initial and basement membrane conditions, $\mathcal{I}_{BM} = \mathcal{I}_{init}$, are outlined by a black thick line on each plot. Colour bars indicate the level of Delta ligand. The simulations were performed using **Setup 3** from Table B.10. Parameter values are listed in Tables B.7 and B.8 for subcellular and cellular/tissue scales, respectively. The movie is available for download at https://github.com/daria-stepanova/PhD_thesis_supplementary_materials.

Movie 2.3 Single realisations of cells shuffling within a linear sprout when two given cell lines are mixed 1:1 (50% to 50%). The cell lines used in each realisation are indicated in the titles. In the top row, no treatment with DAPT inhibitor was applied to cells; in the bottom row, all ECs were treated with DAPT. The leading edge corresponds

to two rightmost voxels of each sprout. The colour bar for Delta level of the WT goes from red colour (stalk cell) to green (tip cell), whereas for the mutant cells the bar goes from purple colour (stalk cell) to yellow (tip cell). The simulations were performed using **Setup 4** from Table B.10. Parameter values are listed in Tables B.7 and B.8 for subcellular and cellular/tissue scales, respectively, except for the changed parameters for the mutant cells listed in Appendix B.3. Final simulation time, $T_{max} = 50.0$. The movie is available for download at https://github.com/daria-stepanova/PhD_thesis_supplementary_materials.

Movie 2.4 Examples of an individual vascular networks generated by wild type and mutant (VEGFR2^{+/-} and VEGFR1^{+/-}) ECs during simulation of our model with uniform VEGF = 5 ng/ml. The cell line is indicated in the title of each panel. The colour bar indicates levels of Delta, D , (green colour corresponds to tip cells, red – to stalk cells). Arrows indicate the configuration of the orientation landscape, l . Numerical simulation was performed using **Setup 1** from Table B.10 with final simulation time, $T_{max} = 2.5$. Parameter values are listed in Tables B.7 and B.8 for subcellular and cellular/tissue scales, respectively, except for the changed parameters for the mutant cells listed in Appendix B.3. The movie is available for download at https://github.com/daria-stepanova/PhD_thesis_supplementary_materials.

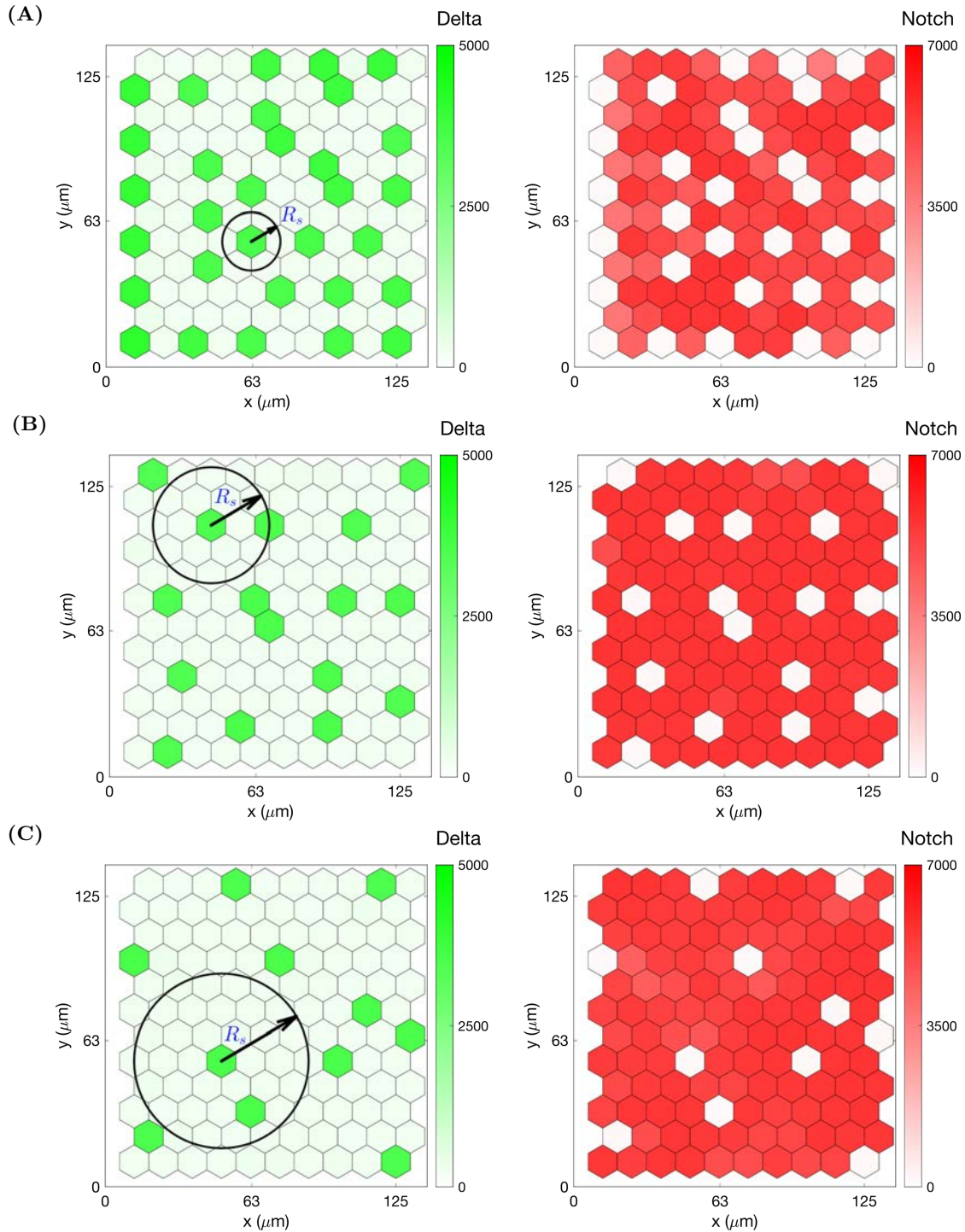


Figure B.15. Examples of steady state patterns of the VEGF-Delta-Notch subcellular model for different interaction radii. Final steady state patterns established during single stochastic simulations of the system described by the kinetic reactions outlined in Figure 2.3D for a uniform hexagonal lattice of 10×12 voxels. (A) $R_s = 1.0h$, (B) $R_s = 2.0h$, (C) $R_s = 3.0h$ and the rest of the parameter values as in Table B.7.

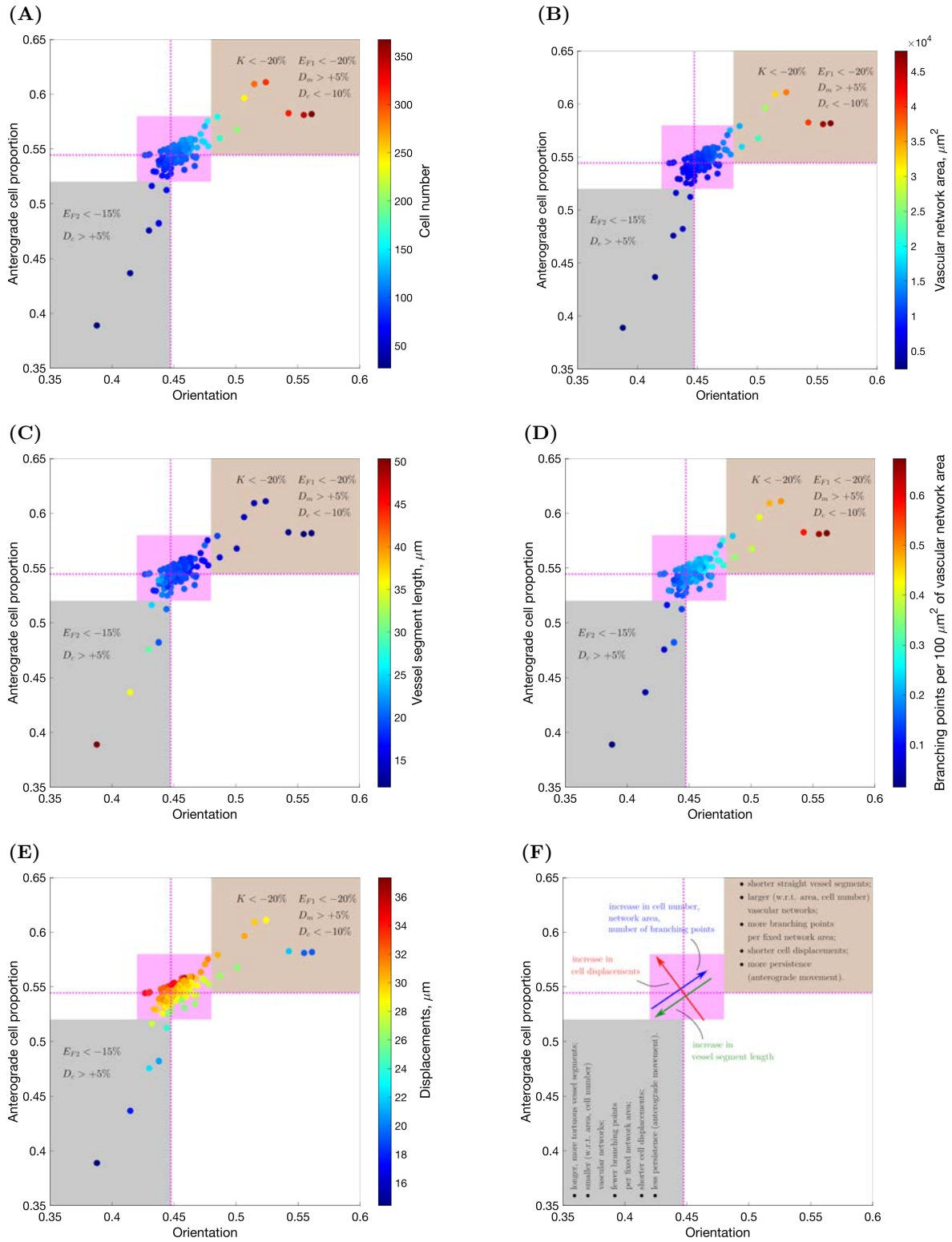


Figure B.16. (Caption on the next page.)

Figure B.16. Sensitivity analysis: orientation vs. anterograde cell proportion.

We performed simulations of our model by varying one of the parameters of the cellular and tissue scales at a time by a fixed per cent and keeping default values for the rest of the parameters (as in Table B.8). Each parameter was varied by $\pm 0.1\%$, $\pm 1\%$, $\pm 5\%$, $\pm 10\%$, $\pm 15\%$ and $\pm 20\%$. For each numerical experiment, several quantitative metrics were computed. The results are represented as scatter plots of mean cell trajectory orientation vs. mean anterograde cell proportion with colouring indicating mean **(A)** cell number; **(B)** vascular network area; **(C)** vessel segment length; **(D)** number of branching points per $100 \mu m^2$ of vascular network area and **(E)** displacements. On these plots, dashed magenta lines indicate the point corresponding to the default parameter values; magenta highlights the region of the main point clustering. The grey-coloured outlier region corresponds to vascular networks with less persistent, twisted vessels, whereas the brown outlier region is characterised by longer straight vessel segments. Variations of the parameters that push the system towards one of the outlier regions are indicated on each plot. Panel **(F)** provides a general summary of these results. Simulation setup as in **Setup 1**, Table B.9, with $T_{max} = 2.5$. The results are averaged over 100 realisations. The subcellular parameters were fixed at their default values in all experiments (see Table B.7).

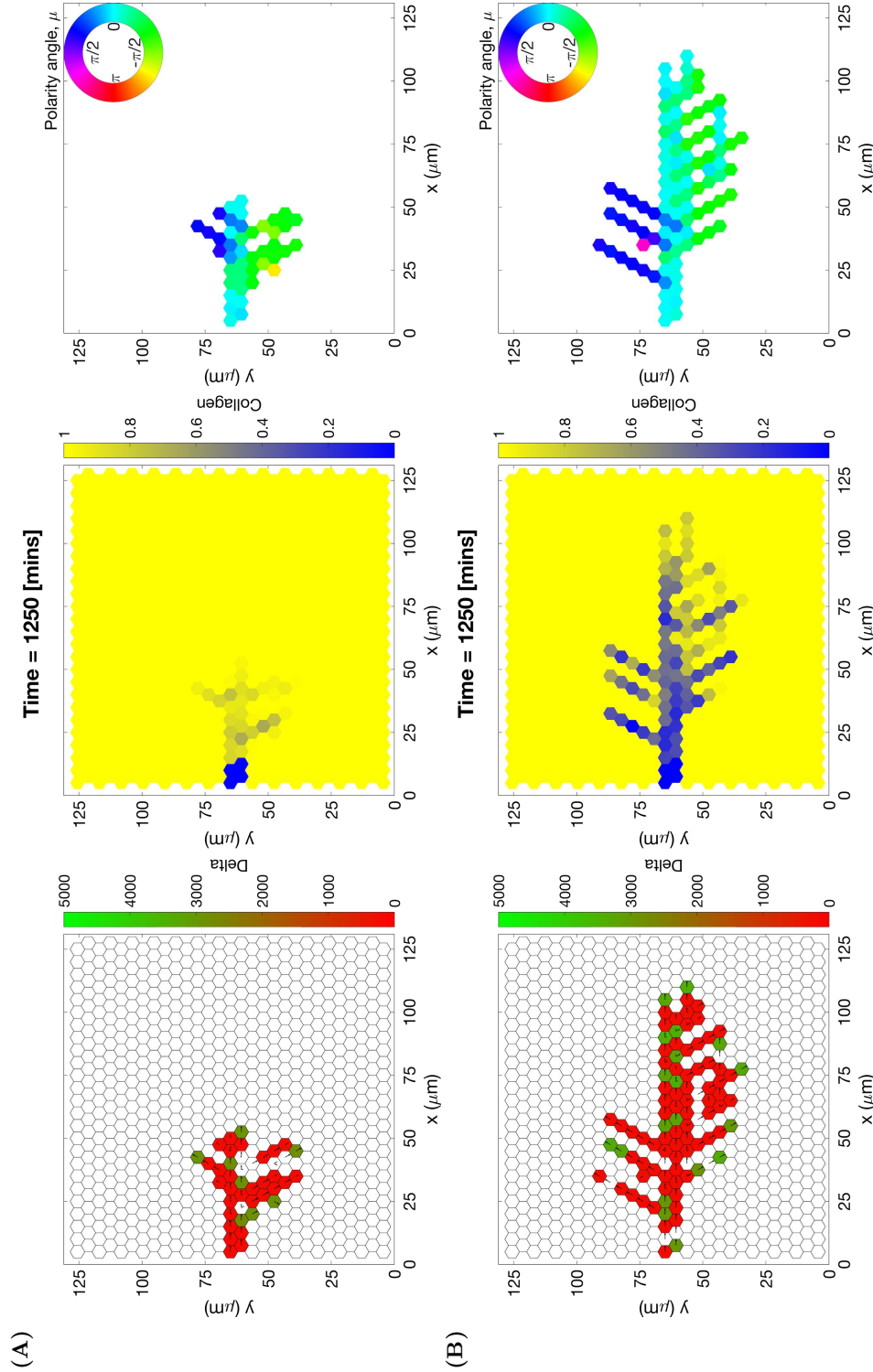


Figure B.17. Individual simulations of vascular networks generated by VEGFR2^{+/-} mutant cells. Final configurations of simulated vascular networks of VEGFR2^{+/-} mutant cells growing in uniform concentration of VEGF = 5 ng/ml, plot (A), and VEGF = 50 ng/ml, plot (B). The leftmost panels show the amount of Delta, **D**. Higher values (green colour) correspond to tip cell phenotype, low values (red colour) – to stalk. On these plots arrows correspond to the orientation landscape configuration, **I**. The central panels indicate the final concentration of the ECM, **c**. The rightmost panels – final distribution of the mean polarity angle, μ , variable. Numerical simulations were performed using **Setup 1** from Table B.10 and $T_{max} = 2.5$. Parameter values are listed in Tables B.7 and B.8 for subcellular and cellular/tissue scales, respectively, except of those changed for VEGFR2^{+/-} mutant cells (see Appendix B.3).

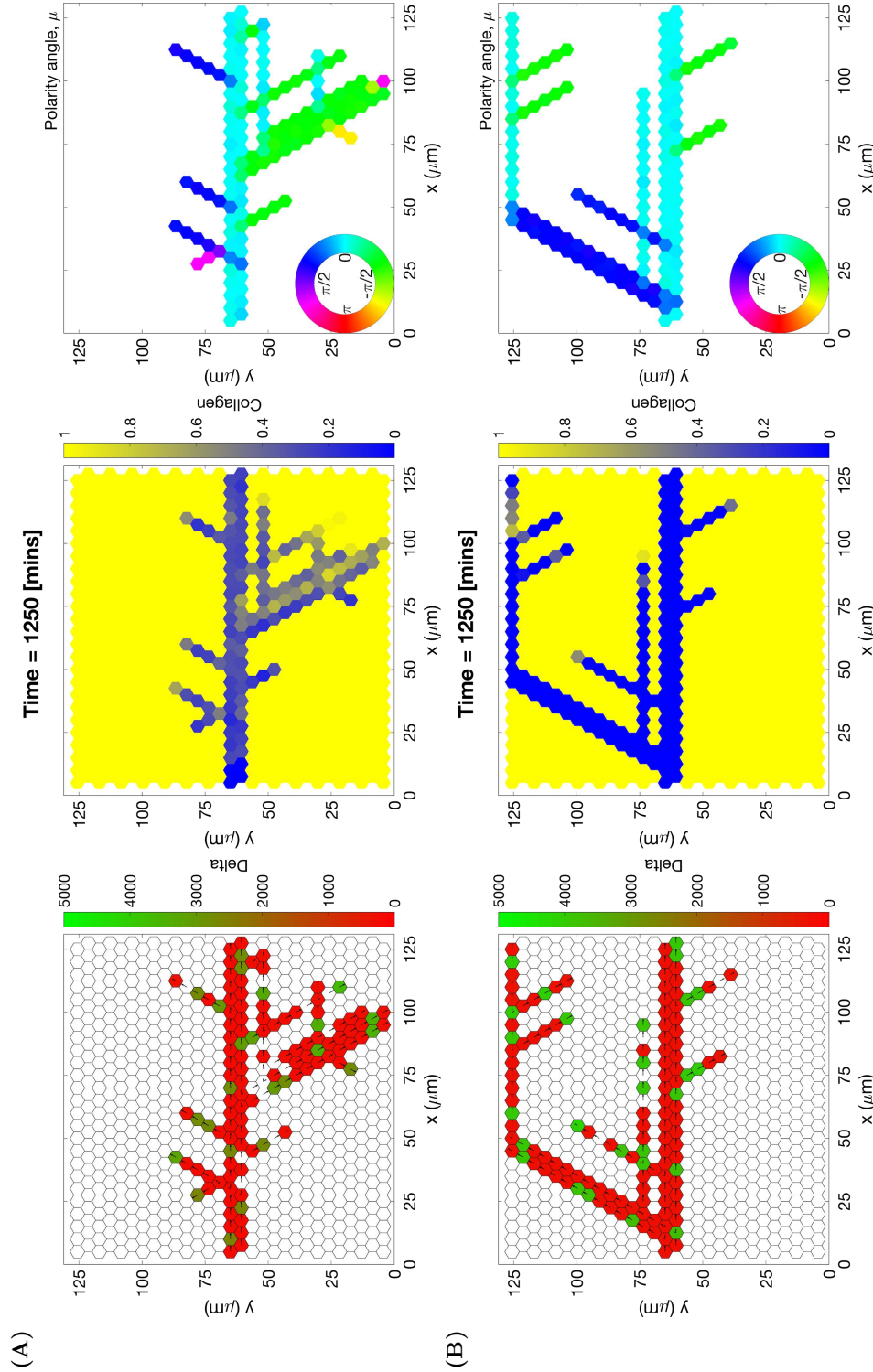


Figure B.18. Individual simulations of vascular networks generated by VEGFR1^{+/-} mutant cells. Final configurations of simulated vascular networks of VEGFR1^{+/-} mutant cells growing in uniform concentration of VEGF = 50 ng/ml, plot (A), and VEGF = 50 ng/ml, plot (B). The leftmost panels show the amount of Delta, D. Higher values (green colour) correspond to tip cell phenotype, low values (red colour) – to stalk. On these plots arrows correspond to the orientation landscape configuration, \mathbf{l} . The central panels indicate the final concentration of the ECM, \mathbf{c} . The rightmost panels – final distribution of the mean polarity angle, μ , variable. Numerical simulations were performed using **Setup 1** from Table B.10 and $T_{max} = 2.5$. Parameter values are listed in Tables B.7 and B.8 for subcellular and cellular/tissue scales, respectively, except of those changed for VEGFR1^{+/-} mutant cells (see Appendix B.3).

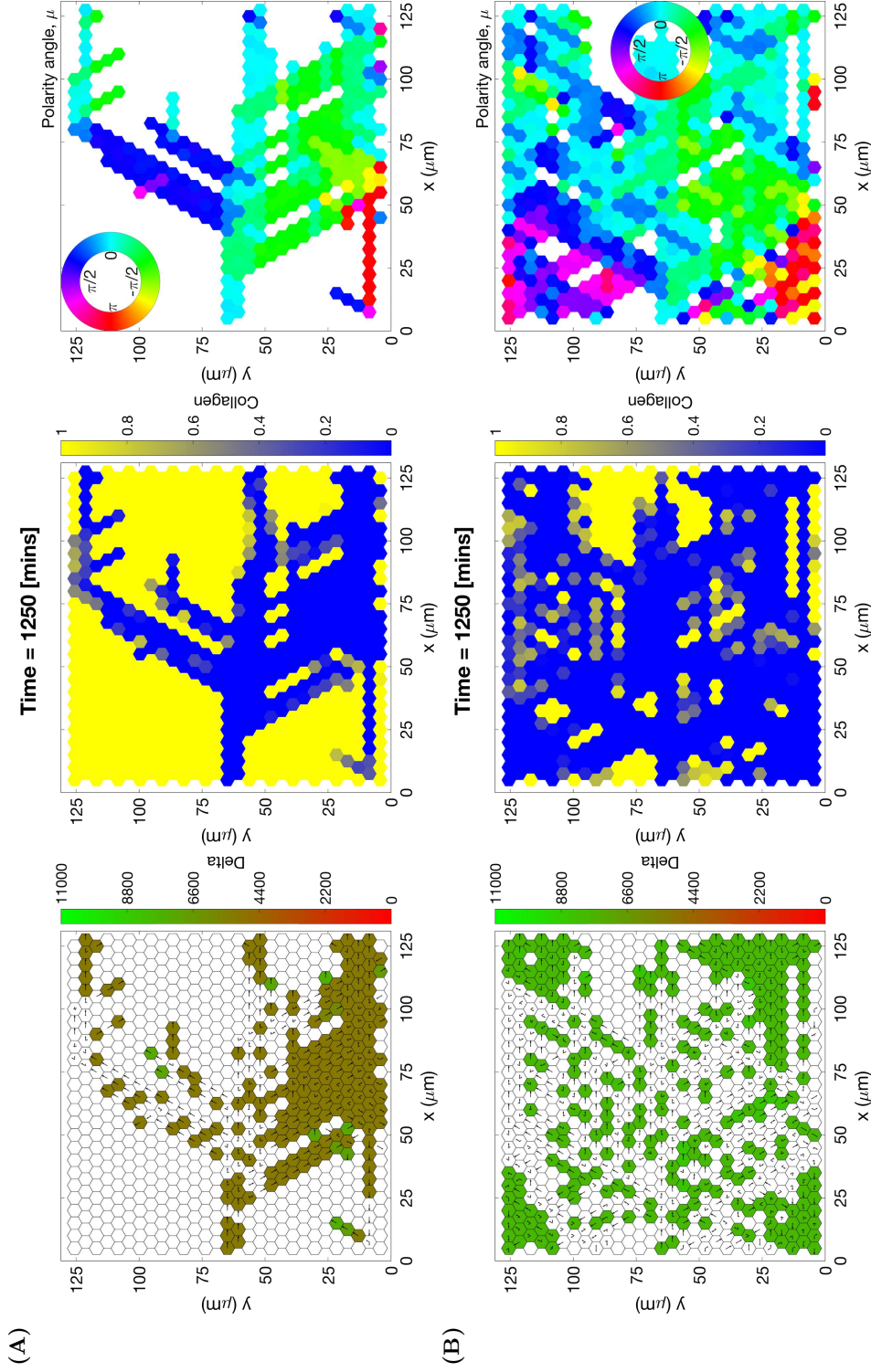


Figure B.19. Individual simulations of vascular networks generated by VEGFR2^{+/-} mutant cells treated with DAPT. Final configurations of simulated vascular networks of VEGFR2^{+/-} mutant cells treated with DAPT growing in uniform concentration of VEGF = 5 ng/ml, plot (A), and VEGF = 50 ng/ml, plot (B). The leftmost panels show the amount of Delta, **D**. Higher values (green colour) correspond to tip cell phenotype, low values (red colour) – to stalk. On these plots arrows correspond to the orientation landscape configuration, **l**. The central panels indicate the final concentration of the ECM, **c**. The rightmost panels – final distribution of the mean polarity angle, μ , variable. Numerical simulations were performed using **Setup 1** from Table B.10 and $T_{max} = 2.5$. Parameter values are listed in Tables B.7 and B.8 for subcellular and cellular/tissue scales, respectively, except of those changed for VEGFR2^{+/-} mutant cells and DAPT treatment (see Appendix B.3).

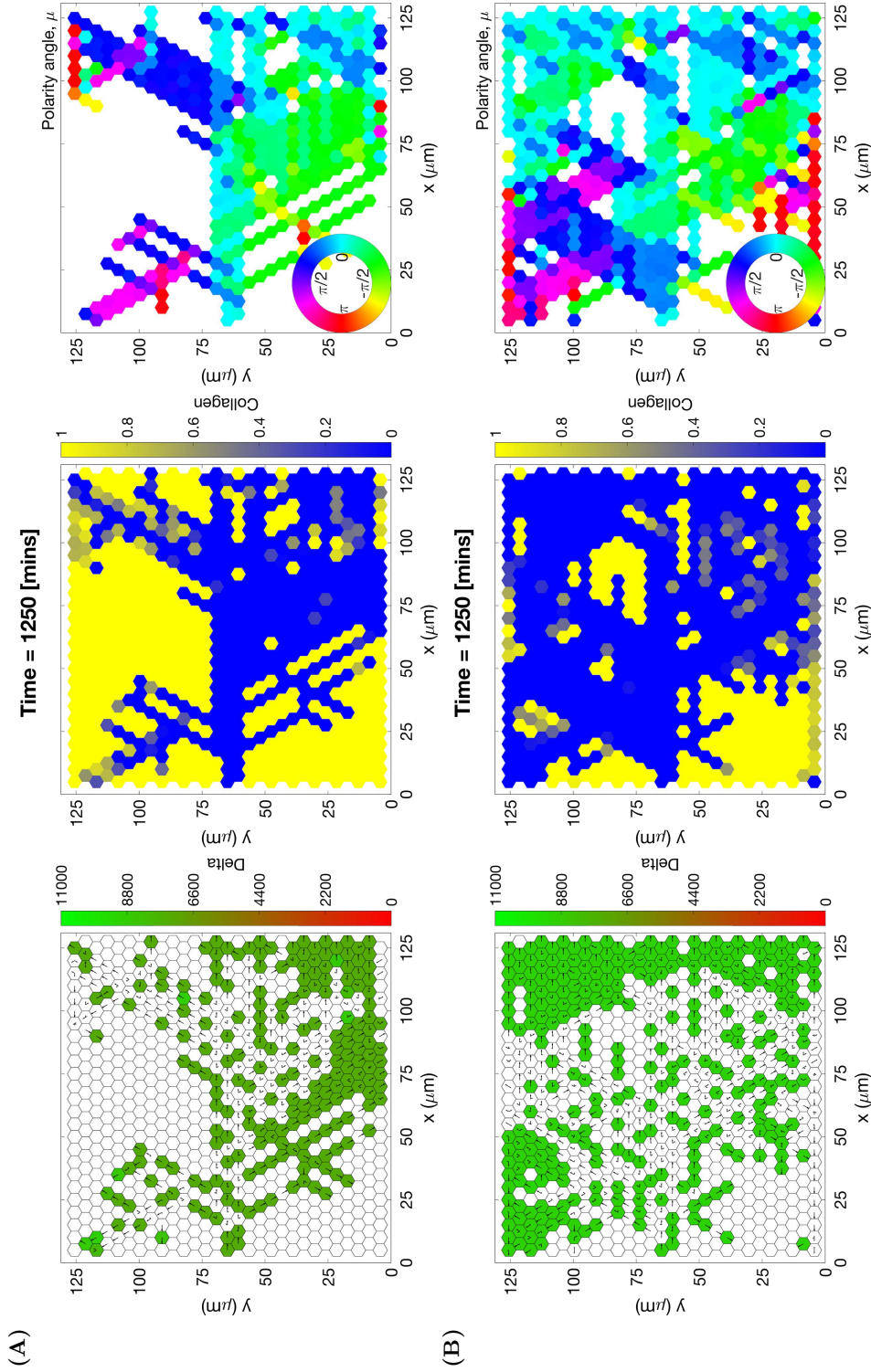


Figure B.20. Individual simulations of vascular networks generated by VEGFR1^{+/-} mutant cells treated with DAPT. Final configurations of simulated vascular networks of VEGFR1^{+/-} mutant cells treated with DAPT growing in uniform concentration of VEGF = 5 ng/ml, plot (A), and VEGF = 50 ng/ml, plot (B). The leftmost panels show the amount of Delta, *D*. Higher values (green colour) correspond to tip cell phenotype, low values (red colour) – to stalk. On these plots arrows correspond to the orientation landscape configuration, *l*. The central panels indicate the final concentration of the ECM, *c*. The rightmost panels – final distribution of the mean polarity angle, μ , variable. Numerical simulations were performed using **Setup 1** from Table B.10 and $T_{max} = 2.5$. Parameter values are listed in Tables B.7 and B.8 for subcellular and cellular/tissue scales, respectively, except of those changed for VEGFR1^{+/-} mutant cells and DAPT treatment (see Appendix B.3).

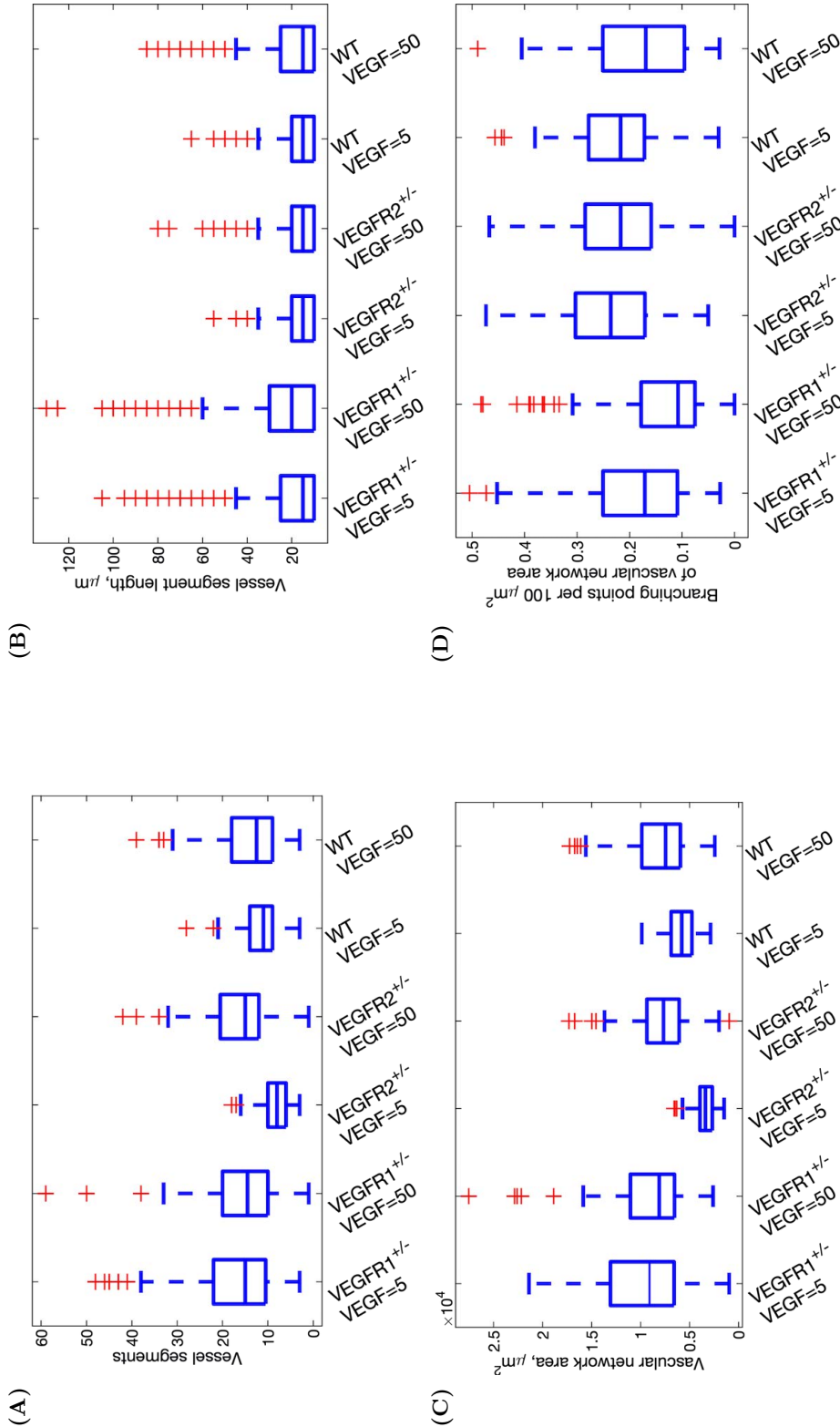


Figure B.21. Quantification of vascular network structure for WT and mutant cells at VEGF = 5 and 50 ng/ml. (A) Number of vessel segments. (B) Vessel segment length (μm). (C) Vascular network area (μm^2) at the end of the numerical simulation. (D) Number of branching points per 100 μm^2 of vascular network area. Details of definitions of these metrics can be found in Appendix B.5. In each box plot, the central line indicates the median, and the horizontal edges of the box represent the 25th and 75th percentiles (for the bottom and top edges, respectively). The outliers are indicated by red cross symbols. Numerical simulation setup used is **Setup 1** from Table B.10 with final simulation time $T_{max} = 2.5$. Parameter values are listed in Tables B.7 and B.8 for subcellular and cellular/tissue scales, respectively, except of those changed for mutant cells (see Appendix B.3). Results are averaged over 100 realisations for each experimental scenario.

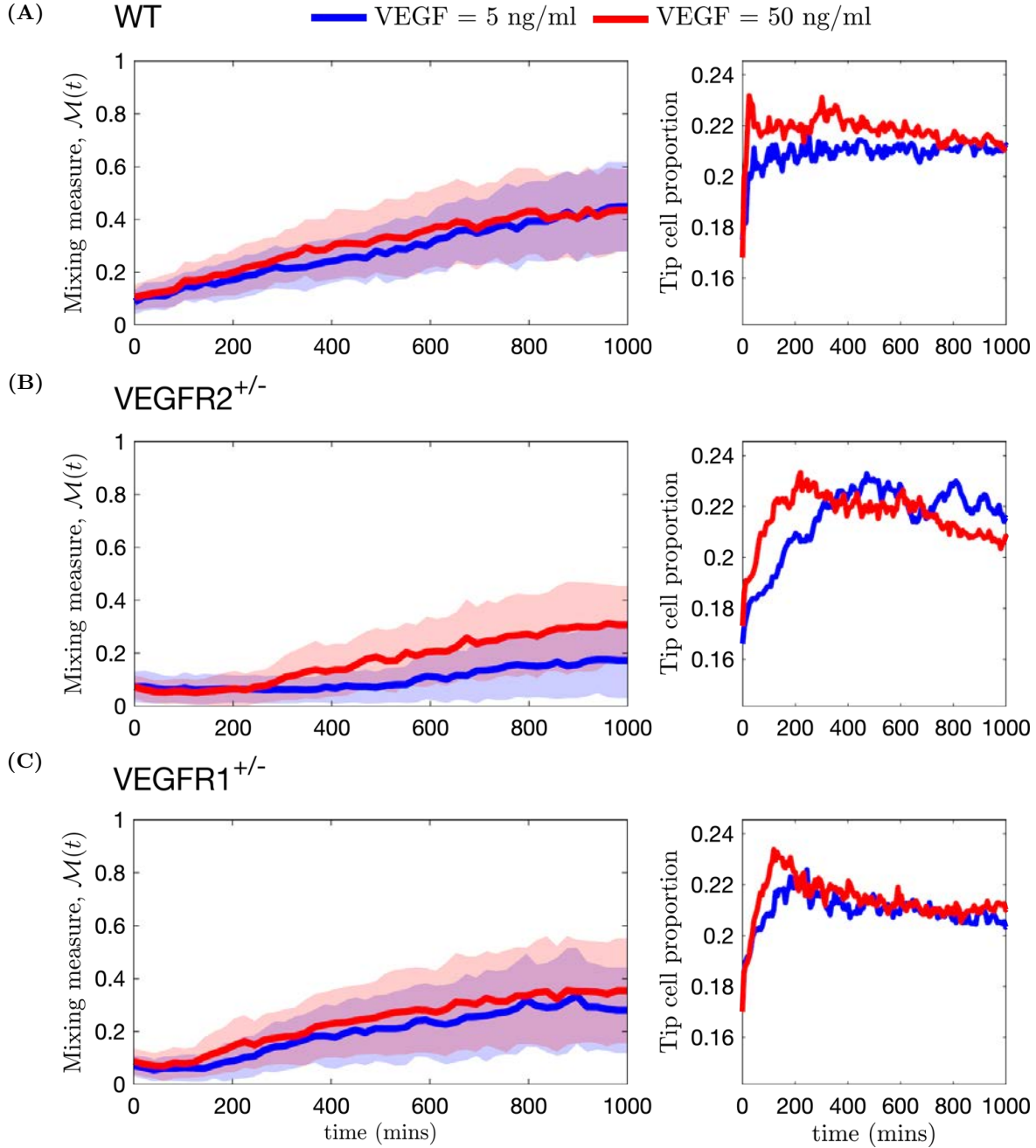


Figure B.22. Temporal evolution of mixing measure and tip cell proportion in simulated vascular networks. Left column plots show the mixing measure, $\mathcal{M}(t)$, as a function of time (the mean value is indicated by a thick line and standard deviation is shown by a band with corresponding colour). Right column plots demonstrate the evolution of tip cell proportion. Simulations were done for networks formed by (A) WT cells; (B) VEGFR2^{+/-} mutant cells; and (C) VEGFR1^{+/-} mutant cells. Numerical simulation setup used is **Setup 1** from Table B.10 with final simulation time $T_{max} = 2.5$. Parameter values are listed in Tables B.7 and B.8 for subcellular and cellular/tissue scales, respectively, except of those changed for mutant cells (see Appendix B.3). Results are averaged over 100 realisations for each experimental scenario.

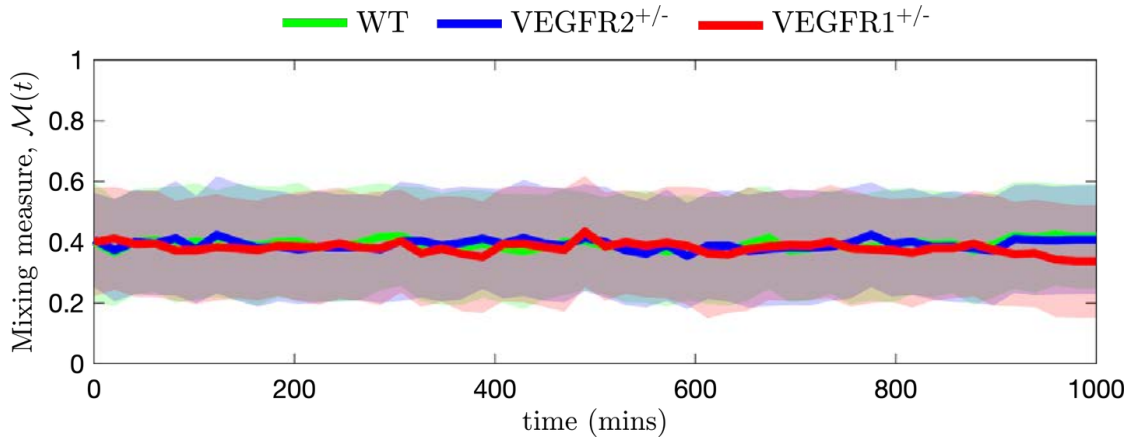


Figure B.23. Mixing measure steady state for VEGF = 0 ng/ml. Plots of mixing measure, $M(t)$, as a function of time for WT, VEGFR2^{+/-} and VEGFR1^{+/-} mutant cells for VEGF=0 ng/ml (the mean value is indicated by a thick line and standard deviation is shown by a band of the corresponding colour). At this concentration of external VEGF, there is no effective sprout elongation, thus cells perform proteolysis-free random shuffling within already existing sprouts [32]. This leads to a steady state of the mixing measure for all cell lineages. Mean values are 0.39, 0.39 and 0.38 for WT, VEGFR2^{+/-} and VEGFR1^{+/-} cells, respectively. Numerical simulations were performed using **Setup 1** from Table B.10 and $T_{max} = 2.5$. Parameter values are listed in Tables B.7 and B.8 for subcellular and cellular/tissue scales, respectively, except of those changed for mutant cells (see Appendix B.3).

Parameter	Units	Description	Value used in simulations	Ref.
R_s	μm	Interaction radius.	15	estim., [11], [34]
b_N	$molec \cdot time^{-1}$	Baseline Notch receptor expression.	500	[155], [156]
b_D	$molec \cdot time^{-1}$	Baseline Delta ligand expression.	800	[155], [156]
b_{R2}	$molec \cdot time^{-1}$	Baseline VEGFR2 expression.	800	[156]
I_0	$molec$	Activation threshold for NICD.	100	[156]
$R2_0^*$	$molec$	Activation threshold for activated VEGFR2.	200	[156]
$\lambda_{I,N}$	<i>dimensionless</i>	Weight factor characterising fold change of the production rate of Notch receptor depending on the NICD concentration.	4.0	[155], [156]
$\lambda_{R2^*,D}$	<i>dimensionless</i>	Weight factor characterising fold change of the production rate of Delta ligand depending on the activated VEGFR2 concentration.	2.0	[156]
$\lambda_{I,R2}$	<i>dimensionless</i>	Weight factor characterising fold change of the production rate of VEGFR2 depending on the NICD concentration.	0.0	[156]
n_N	<i>dimensionless</i>	Cooperativity parameter for Hill function for NICD-dependent Notch up-regulation.	2	[154]
n_D	<i>dimensionless</i>	Cooperativity parameter for Hill function for activated VEGF-dependent Delta up-regulation.	1	[154]
n_{R2}	<i>dimensionless</i>	Cooperativity parameter for Hill function for NICD-dependent VEGFR2 repression.	1	[154]

V	<i>molec</i>	External VEGF.	2500 (Figure 2.3E); 0 – 2500 (Figure 2.3F); {0, 2500, 25000} (in the rest of the simulations)	[155], [156]
D_{ext}	<i>molec</i>	External Delta ligand.	0 – 3000 (Figures 2.3E and 2.3F); calculated from adjacent cells (in the rest of the simula- tions)	[155], [156]
N_{ext}	<i>molec</i>	External Notch receptor.	1000 (Figures 2.3E and 2.3F); calculated from adjacent cells (in the rest of the simulations)	[155], [156]
k_t	$molec^{-1} \cdot time^{-1}$	Trans-binding rate for Notch receptor and Delta ligand.	$5.0e - 5$	[154]
k_c	$molec^{-1} \cdot time^{-1}$	Cis-interaction rate for Notch receptor and Delta ligand.	$6.0e - 4$	[154]
k_v	$molec^{-1} \cdot time^{-1}$	Binding rate for VEGFR2 and external VEGF.	$5.0e - 5$	[156]
η	<i>dimensionless</i>	Endocytic regulation of Notch signalling.	0.5	estim., [223]
γ	$time^{-1}$	Degradation rate of pro- teins.	0.1	[156]
γ_e	$time^{-1}$	Degradation rate of acti- vated receptors.	0.5	[156]

Table B.7. Baseline parameter values for the VEGF-Delta-Notch subcellular model. Description and reference values used in simulations of the subcellular VEGF-Delta-Notch signalling.

Parameter	Value	Parameter	Value	Parameter	Value	Parameter	Value
R_c	1.5h	D_ω	1.0	c_{max}	1.0	Δ_l	0.01
E_{F1}	0.25	E_{F2}	0.7	s_{F1}	35.0	s_{F2}	10.0
p_{max}	0.26	s_p	0.0015	D_p	1500	a	7.0
n	2	K	20.0	k_m	2.6	k_D	0.0002
η_l	0.1	η_{max}	12.5	s_c	0.003	D_c	4200
γ_{max}	17.0	s_m	0.003	D_m	4200		

Table B.8. Parameter values of the cellular and tissue scales used in our simulations.

Variable	Indexes	Description
$E_i = 1$ $E_i = 0$	$i \in \mathcal{I}_{init}$ $i \in \mathcal{I} \setminus \mathcal{I}_{init}$	Initial distribution of cell nuclei.
$N_i = \text{DUnif}[(1 - \xi)b_N, (1 + \xi)b_N]$ $D_i = \text{DUnif}[(1 - \xi)b_D, (1 + \xi)b_D]$ $I_i = \text{DUnif}[(1 - \xi)I_0, (1 + \xi)I_0]$ $R2_i = \text{DUnif}[(1 - \xi)b_{R2}, (1 + \xi)b_{R2}]$ $R2_i^* = \text{DUnif}[(1 - \xi)R2_0^*, (1 + \xi)R2_0^*]$ $N_i = D_i = I_i = R2_i = R2_i^* = 0$	$i \in \mathcal{I}_{init}$ $i \in \mathcal{I} \setminus \mathcal{I}_{init}$	Cells are initialised with ligand/receptor numbers corresponding to their baseline gene expression with a correction for random fluctuations included via the parameter ξ . At the voxels where there is no cell nucleus, subcellular variables are initialised with the value zero.
$l_i^{s_{init}} = 2\Delta_{init}$	$i \in \mathcal{I}_{init}$	The alignment of ECM fibrils for voxels where cells were initially placed in the direction $s_{init} \in \mathcal{S}$.
$l_i^s = \text{Unif}[0, \Delta_{init}]$ $l_i^s = \text{Unif}[0, \Delta_{init}]$	$i \in \mathcal{I} \setminus \mathcal{I}_{init},$ $\forall s \in \mathcal{S}$ $i \in \mathcal{I}_{init},$ $\forall s \neq s_{init} \in \mathcal{S}$	The alignment of ECM fibrils for the rest of the voxels is initialised with a small random value in a given range, $[0, \Delta_{init}]$, imitating random orientation of fibrils prior to their realignment due to cell migration.
$c_i = c_{init}$ $c_i = c_{max}$	$i \in \mathcal{I}_{init}$ $i \in \mathcal{I} \setminus \mathcal{I}_{init}$	The ECM concentration at the voxels with cells is equal to $c_{init} \in [0, c_{max}]$ (specified for each numerical experiment). For other voxels, the ECM is assumed to be unchanged, thus equal to the maximum ECM concentration, c_{max} .
$m_i = m_{init}$ $m_i = 0$	$i \in \mathcal{I}_{init}$ $i \in \mathcal{I} \setminus \mathcal{I}_{init}$	The concentration of BM components at the voxels with cells is equal to $m_{init} \in [0, 1]$ (specified for each numerical experiment). For other voxels, no BM components have been deposited, thus the concentration is set to zero.

Table B.9. (Caption on the next page.)

Table B.9. Initial conditions for numerical simulations. Here \mathcal{I} is the set of all voxels; \mathcal{S} is the set of all possible migration directions. $\text{DUnif}[a, b]$ is a discrete uniform distribution over all integer numbers lying within the interval $[a, b]$; $\text{Unif}[a, b]$ is the uniform distribution on the interval $[a, b]$. Baseline gene expression parameters for the VEGF-Delta-Notch signalling are listed in Table B.7. $\Delta_{init} = 1.0$ for all numerical simulations (this value, as, in general, for the value of the OL variable, is non-dimensional). The fluctuation parameter, ξ , is set to 0.1 in all numerical simulations. The exact values for c_{init} and m_{init} are given for each numerical experiment in Table B.10, as well as the set of initial cell positions, \mathcal{I}_{init} . For the description of model variables see Table 2.1 in the main text.

Set-up	Specifications	Figures
Setup 1: Individual sprout	$N_I^x = 25, N_I^y = 29$ $\mathcal{I}_{init} = \{i = (i_x, i_y)^T : i_x = 1, 2, i_y = 14, 15\}$ $\mathcal{I}_{VP} = \{i = (1, i_y)^T : i_y = 14, 15\}$ $s_{init} = r$ $c_{init} = 0.0, m_{init} = 1.0$ $V \in \{0, 2500, 25000\}$, uniform distribution over the lattice, which correspond to 0, 5 and 50 ng/ml VEGF concentration, respectively. The exact value specified in the text. Simulations with this setup are performed with WT and mutant cells (see Table B.7 and Appendix B.3, respectively).	For WT cells: Figures 2.7, 2.8, 2.10, 2.13, 2.14, B.21-B.23. For mutant cells: Figures 2.15, B.17-B.23.
Setup 2: Vessel in VEGF gradient	$N_I^x = 25, N_I^y = 29$ $\mathcal{I}_{init} = \{i = (i_x, i_y)^T : i_x = 12, 13, i_y = 1, \dots, 29\}$ $\mathcal{I}_{VP} = \mathcal{I}_{init}$ s_{init} - not specified $c_{init} = c_{max}, m_{init} = 0.0$ $V(i_x, i_y) = 2500 \frac{i_y}{N_I^y}$. This corresponds to a VEGF gradient linearly increasing from 0 to 5 ng/ml along the y -axis. Simulations with this setup are performed with WT cells (see Table B.7).	Figure 2.9
Setup 3: Cell bead	$N_I^x = 25, N_I^y = 29$ $\mathcal{I}_{init} = \{i = (i_x, i_y)^T : (i_x - 13)^2 + (i_y - 9)^2 \leq 5, i \in \mathcal{I}\}$ $\mathcal{I}_{VP} = \mathcal{I}_{init}$ s_{init} - not specified $c_{init} = c_{max}, m_{init} = 0.0$ $V(i_x, i_y) = 2500 \frac{i_y}{N_I^y}$. This corresponds to a VEGF gradient linearly increasing from 0 to 5 ng/ml along the y -axis. Simulations with this setup are performed with WT cells (see Table B.7).	Figure 2.11
Setup 4: Linear sprout	$N_I^x = 25, N_I^y = 2$ $\mathcal{I}_{init} = \{i = (i_x, i_y)^T : i_x = 1, \dots, 25, i_y = 1, 2\}$ $\mathcal{I}_{VP} = \mathcal{I}_{init}$ $s_{init} = r$ $c_{init} = 0.0, m_{init} = 1.0$ $V = 15000$, corresponding to a constant uniform distribution of VEGF at the concentration 30 ng/ml (used in [9]). Simulations with this setup are performed with mutant cells (Appendix B.3).	Figure 2.12, Table 2.3

Table B.10. (Caption on the next page.)

Table B.10. Setups of simulation experiments. For each setup of numerical simulation we specify the lattice dimensions, N_I^x and N_I^y ; the set of indices corresponding to the vascular plexus, \mathcal{I}_{VP} ; the initial cell nuclei positions, \mathcal{I}_{init} ; the initial polarisation direction, s_{init} ; the initial ECM and BM concentrations, c_{init} and m_{init} , respectively; the VEGF distribution over the lattice, V ; and cell line used in simulations.

Appendix C

Supplementary materials for Chapter 3

C.1 Geometric minimum action method (gMAM)

The geometric minimum action method (gMAM) was developed in [181] as a technique for efficient numerical computation of the minimum action path (MAP) and the corresponding quasipotential (given as the minimum of the action functional) of a rare event. Briefly, starting with the geometric representation, $\widehat{S}(\phi)$ (Eq (3.6)), the Euler-Lagrange equation associated with the minimisation of $\widehat{S}(\phi)$ is derived, assuming $\hat{\theta}(\phi, \phi')$ is known. Then a (pre-conditioned) steepest descend algorithm can be used to solve this Euler-Lagrange equation, maintaining the standard arc length parametrisation of ϕ . If no explicit formula for $\hat{\theta}(\phi, \phi')$ is available, then $\hat{\theta}(\phi, \phi')$ is computed in the inner loop of the algorithm, as a solution to the system

$$H(x, \hat{\theta}) = 0 \tag{C.1a}$$

$$\frac{\partial H(x, \theta)}{\partial \theta} = \lambda \phi' \tag{C.1b}$$

for some λ .

For a diffusion process of type Eq (3.1), there are explicit expressions for the Lagrangian and the corresponding Hamiltonian

$$L(x, y) = \langle y - b(x), a^{-1}(x)(y - b(x)) \rangle = \|y - b(x)\|_a^2, \tag{C.2a}$$

$$H(x, \theta) = \langle b(x), \theta \rangle + \frac{1}{2} \langle \theta, a(x)\theta \rangle, \tag{C.2b}$$

where $\|p\|_a^2 = \langle p, a^{-1}(x)p \rangle$ is a norm induced by the diffusion tensor, $a(x)$. This allows us to explicitly derive the action functional in its geometric reformulation [181],

$$\widehat{S}(\phi) = \left(\int_0^1 \|\phi'\|_a \|b(\phi)\|_a - \langle \phi', a^{-1}(\phi)b(\phi) \rangle \right) d\alpha,$$

and the solution to the system of equations Eq (C.1):

$$\hat{\theta}(x, y) = a^{-1}(x) \left(\frac{\|b(x)\|_a}{\|y\|_a} - b(x) \right), \quad (\text{C.3a})$$

$$\lambda(x, y) = \frac{\|b(x)\|_a}{\|y\|_a}. \quad (\text{C.3b})$$

For a general birth-death CTMC of type Eq (B.2) with transition rates, $\alpha^R(x)$, and the corresponding stoichiometric vectors, ν^R , the Hamiltonian reads:

$$H(x, \theta) = \sum_R \alpha^R(x) (\exp(\langle \theta, \nu^R \rangle) - 1). \quad (\text{C.4})$$

In this case, there is no explicit solution to the system given by Eq (C.1) but it can be computed in the inner loop of the gMAM [181].

For the convergence of the gMAM for an SDE, a and b must be bounded and uniformly continuous, and a has to be uniformly elliptic, whereas, for a CME, the rate functions, α^R , must be uniformly bounded away from 0 and $+\infty$ [181].

For alternative numerical methods to compute minimum action paths (MAPs) we refer the reader to [180], [185] and references therein.

C.2 System of stochastic differential equations of the VEGF-Delta-Notch model (individual cell)

Let $x^\epsilon = (n^\epsilon, d^\epsilon, \iota^\epsilon, r2^\epsilon, r2^{*\epsilon})^T$. Then, the SDE for the stochastic VEGF-Delta-Notch system reads:

$$dx^\epsilon(t) = b(x^\epsilon)dt + \sqrt{\epsilon}\sigma(x^\epsilon)dW. \quad (\text{C.5})$$

Here the drift vector, $b(x^\epsilon) \in \mathbb{R}^5$, is given by Eq (C.6), the diffusion tensor, $a(x^\epsilon) = (\sigma\sigma^T)(x^\epsilon) \in \mathbb{R}^{5 \times 5}$, and $\sigma^T(x^\epsilon) \in \mathbb{R}^{12 \times 5}$ is given by Eq (C.7). The level of noise is controlled by $\epsilon = \Omega^{-1}$. Finally, W is a Wiener process in \mathbb{R}^{12} .

$$b(x^\epsilon) = \begin{pmatrix} \beta_N H^S(\rho_N \iota^\epsilon; 1.0, \lambda_{I,N}, n_N) - n^\epsilon - d_{ext} n^\epsilon - \kappa n^\epsilon d^\epsilon \\ \beta_D H^S(\rho_{R_2} r2^{*\epsilon}; 1.0, \lambda_{R_2^*,D}, n_D) - d^\epsilon - \eta n_{ext} d^\epsilon - \kappa n^\epsilon d^\epsilon \\ d_{ext} n^\epsilon - \hat{\tau} \iota^\epsilon \\ \beta_{R_2} H^S(\rho_N \iota^\epsilon; 1.0, \lambda_{I,R_2}, n_{R_2}) - (1 + v_{ext}) r2^\epsilon \\ v_{ext} r2^\epsilon - \hat{\tau} r2^{*\epsilon} \end{pmatrix}. \quad (\text{C.6})$$

Here the shifted Hill function, $H^S(p; p_0, \lambda, n) = \frac{1 + \lambda(p/p_0)^n}{1 + (p/p_0)^n}$.

The matrix $\sigma^T(x^\epsilon)$ takes the form:

$$\sigma^T(x^\epsilon) = \begin{pmatrix} S_1(x^\epsilon) & 0_{8 \times 2} \\ 0_{4 \times 3} & S_2(x^\epsilon) \end{pmatrix}, \quad (\text{C.7})$$

where $0_{n \times m}$ is a zero block matrix of size $n \times m$, and block matrices $S_1(x^\epsilon) \in \mathbb{R}^{8 \times 5}$ and $S_2(x^\epsilon) \in \mathbb{R}^{4 \times 2}$ are defined as

$$S_1(x^\epsilon) = \begin{pmatrix} \sqrt{\beta_N H^S(\rho_N t^\epsilon; 1.0, \lambda_{I,N}, n_N)} & 0 & 0 \\ -\sqrt{n^\epsilon} & 0 & 0 \\ 0 & \sqrt{\beta_D H^S(\rho_{R2} r^{2*\epsilon}; 1.0, \lambda_{R2^*,D}, n_D)} & 0 \\ 0 & -\sqrt{d^\epsilon} & 0 \\ -\sqrt{d_{ext} n^\epsilon} & 0 & \sqrt{d_{ext} n^\epsilon} \\ 0 & -\sqrt{\eta n_{ext} d^\epsilon} & 0 \\ 0 & 0 & -\sqrt{\hat{\tau} r^{2*\epsilon}} \\ -\sqrt{\kappa n^\epsilon d^\epsilon} & -\sqrt{\kappa n^\epsilon d^\epsilon} & 0 \end{pmatrix},$$

$$S_2(x^\epsilon) = \begin{pmatrix} \sqrt{\beta_{R2} H^S(\rho_N t^\epsilon; 1.0, \lambda_{I,R2}, n_{R2})} & 0 \\ -\sqrt{v_{ext} r^{2^\epsilon}} & -\sqrt{v_{ext} r^{2^\epsilon}} \\ -\sqrt{r^{2^\epsilon}} & 0 \\ 0 & -\sqrt{r^{2*\epsilon}} \end{pmatrix}.$$

C.3 Minimum action path (MAP) for the VEGF-Delta-Notch system in individual cell

Using the SDE for the VEGF-Delta-Notch system (Eqs (C.5), (C.6) and (C.7)), we implemented the gMAM to compute the minimum action path (MAP) and the corresponding quasipotential (using explicit expressions for the Hamiltonian and the momentum, Eqs (C.2) and (C.3)). An illustration of the MAPs for transitions between phenotypes for a fixed set of parameters (Table C.1) is shown in Figure C.1. In addition, Figure C.2 demonstrates the tubular neighbourhoods around these MAPs (the transition tubes within which phenotype transitions occur) for different values of the noise level. It can be seen that transition paths can diverge more from the corresponding MAP in higher noise levels ($\epsilon \approx 0.014$ in Figure 3.4A) than in lower ones ($\epsilon \approx 0.002$ in Figure 3.4B).

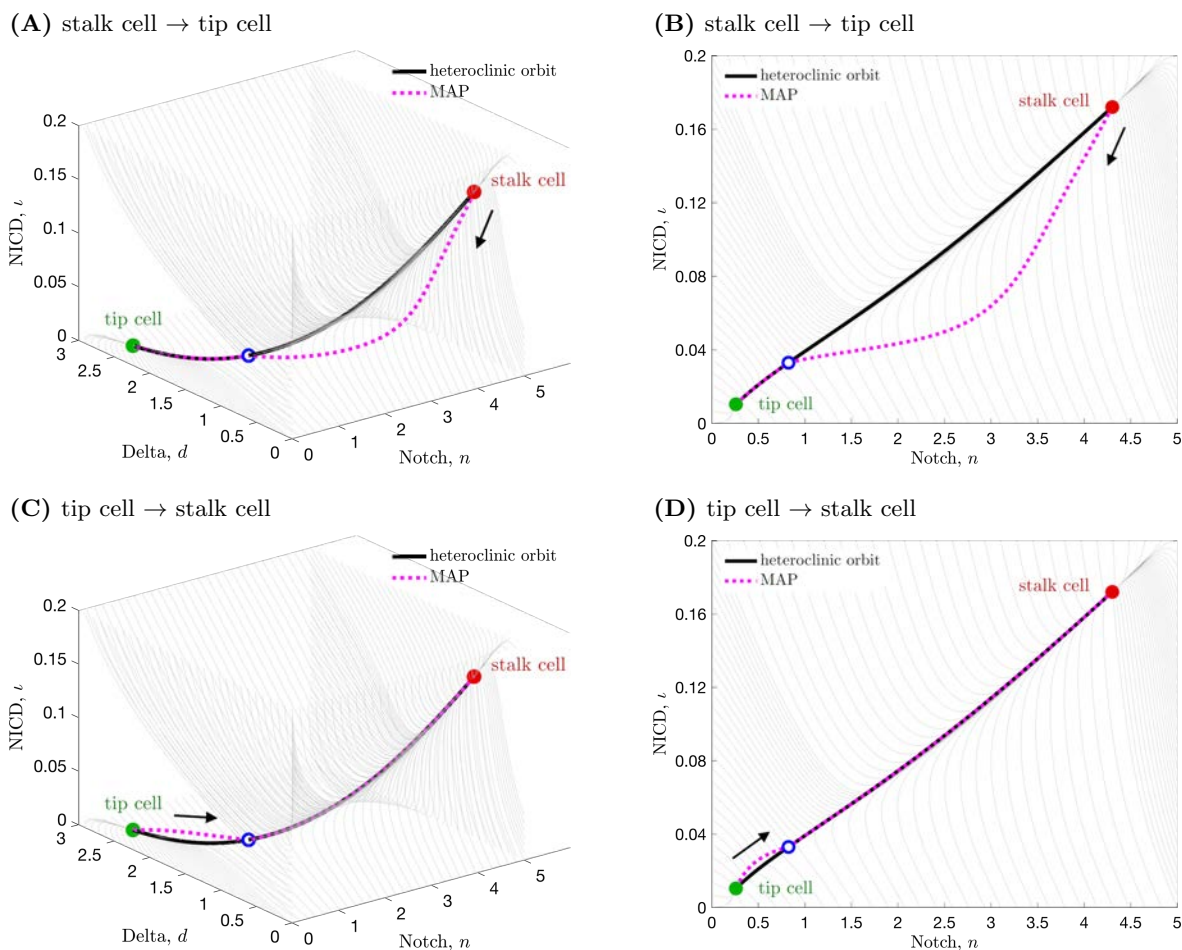


Figure C.1. Minimum action paths. Projections (3D, left panels; 2D, right panels) of the MAPs computed using the gMAM (dotted magenta lines) for transitions from (A)-(B) stalk cell \rightarrow tip cell; (C)-(D) tip cell \rightarrow stalk cell. Streamlines associated with the mean-field model are drawn in grey. Stable steady states corresponding to tip (stalk) cell phenotype are indicated by filled green (red) circles; unstable saddle points are indicated by unfilled blue circles. Heteroclinic orbits, connecting steady states, are indicated by thick black lines.

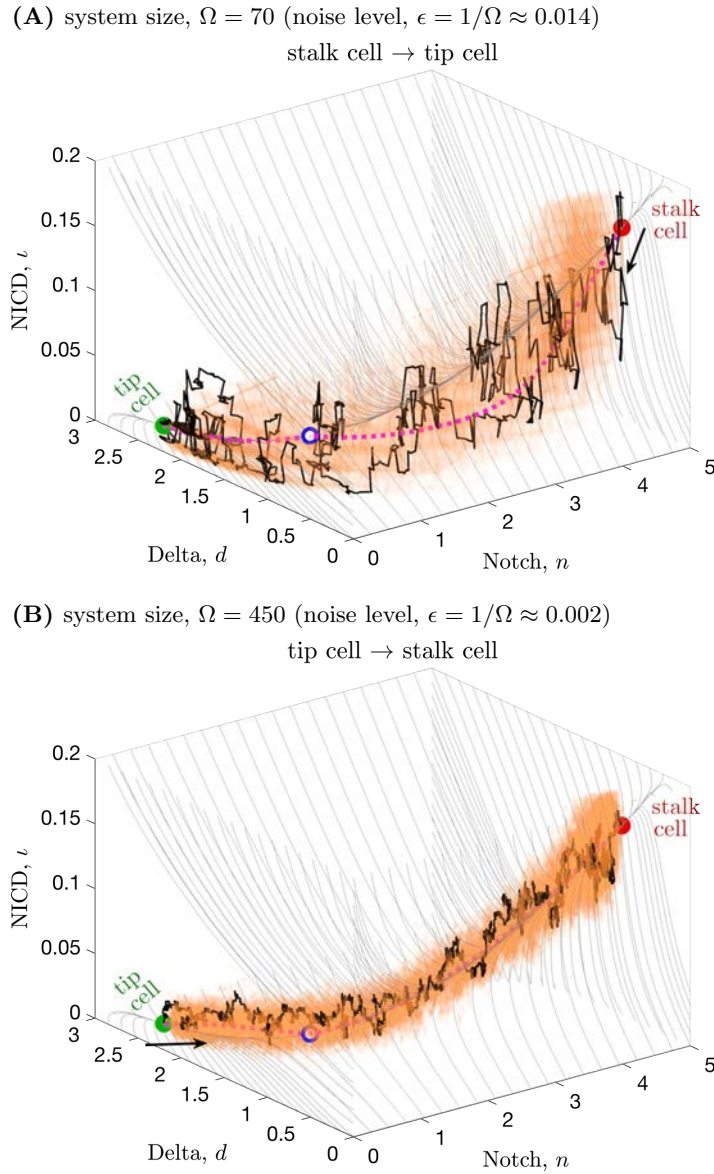


Figure C.2. An illustration of the transition tubes for stochastic sample paths of transitions between the cell phenotypes. This figure corresponds to Figure 3.4 of the main text. Here, we additionally plotted in orange 100 transition paths for the corresponding trajectories from (A) stalk to tip cell and (B) tip to stalk cell. Thus, the regions shaded in orange indicate the transition tubes around the MAPs (indicated by the dotted magenta lines) for the corresponding noise level. Representative stochastic sample paths (identical to the ones shown in Figure 3.4) obtained by simulating the full stochastic CTMC model (Table B.1) with the system sizes (A) $\Omega = 70$, (B) $\Omega = 450$, are plotted in black. The thin grey lines indicate streamlines of the corresponding mean-field system (Eq (B.4)). The tip (stalk) cell stable steady state is indicated by a green (red) filled circle; the unstable saddle by a blue unfilled circle. The plots represent three-dimensional projections of the full five-dimensional system as defined by Eq (B.4). Parameter values are fixed as indicated in Table C.1.

C.4 Pseudocode algorithm for simulating the multi-agent CG model of a system with a region of multistability

Algorithm 8. Pseudocode algorithm for simulating the multi-agent CG model of a system with a region of multistability.

- 1: Specify final simulation time, T_{final} , and the system size, Ω .
- 2: Given a discretisation, $\{u_j\}_j$, of the external (bifurcation) variables, read look-up tables for steady states, quasipotential and prefactor values.
- 3: For each u_j , compute CG transition rates, $\omega_{x_k \rightarrow x_l}$, $k, l = 1 \dots \mathcal{K}$, $k \neq l$, defined by Eq (3.7) for the specified Ω . Here $\{x_k\}_{k=1}^{\mathcal{K}}$ is a set of stable steady states.
- 4: Initialise interpolation routines to establish an input-output relationship between an arbitrary $u \in \mathcal{U}$ and the CG transition rates, $\omega_{x_k \rightarrow x_l}$.
- 5: Initialise the system with a pre-pattern by using the original stochastic model or its mean-field limit (preferable).
- 6: Set the simulation time, $t = 0$.
- 7: **while** $t < T_{final}$ **do**
- 8: Set total propensity, $P = 0$.
- 9: **for** each entity, e , **do**
- 10: Compute its external variables, u^e .
- 11: **for** $k, l = 1 \dots \mathcal{K}$, $k \neq l$, **do**
- 12: Interpolate $\omega_{x_k \rightarrow x_l}^e$ for the given u^e .
- 13: $P = P + \omega_{x_k \rightarrow x_l}^e$.
- 14: **end for**
- 15: **end for**
- 16: Sample the waiting time for the next transition to occur, $\bar{\tau} \sim \text{Exp}(1/P)$, where $\text{Exp}(\lambda)$ is an exponential distribution of intensity λ .
- 17: Probabilistically (as in the Gillespie algorithm), decide which transition occurs (in which entity, \bar{e} , and between which stable steady states).
- 18: For this entity, compute again $u^{\bar{e}}$ and interpolate its new steady state after the transition.
- 19: Update the simulation time, $t = t + \bar{\tau}$.
- 20: **end while**
- 21: End of simulation.

C.5 Quantification metrics

We used the following metrics to compare our models.

Tip cell proportion This metric is defined as in Appendix B.5 with a difference that here we use the *non-dimensional* Delta levels as a proxy to determine cell phenotype. Thus, the number of tip cells is given by the number of cells whose (non-dimensional) Delta level exceeds the threshold $d_{tip} = 0.1\beta_D$. Then the tip cell proportion at time, t , can be computed as the ratio of the number of tip cells to the total number of cells. Here, β_D is the characteristic expression of Delta in a cell (see Table C.1).

Tip cell cluster distribution Depending on the parameter values, in the final spatial pattern (at a fixed final simulation time), tip cells can form small clusters, i.e. be adjacent (see Figure C.3). We extracted the distribution of the cluster sizes for final configurations of the spatial phenotype pattern.

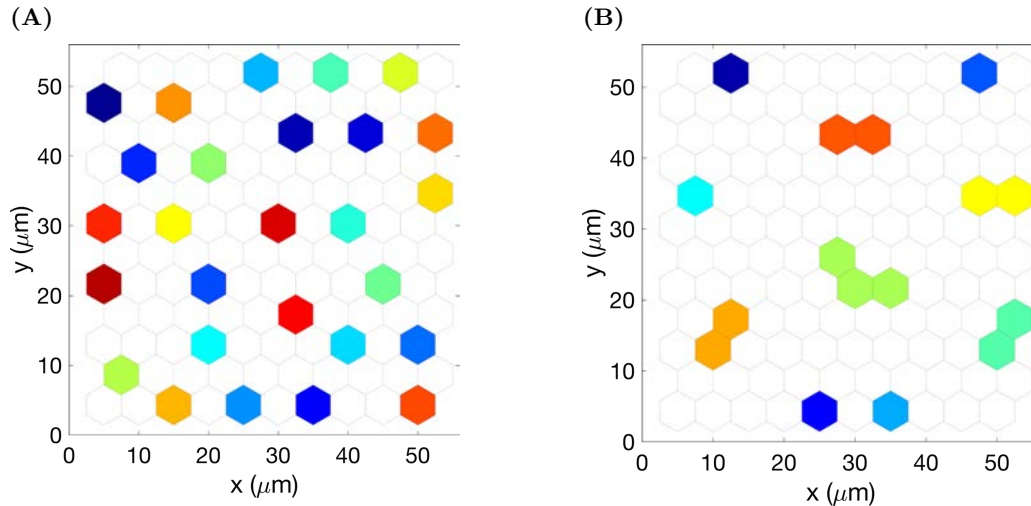


Figure C.3. Simulation results showing how the long time distribution of tip cell clusters in a small monolayer of cells changes as the cell-to-cell interaction radius varies. Cell interaction radius (A) $R_s = 5\mu m$ (B) $R_s = 15\mu m$. Each group of tip cells (a cluster) is coloured by a distinct colour (randomly chosen). Stalk cells are left white.

Computational cost Computational cost is defined to be the mean CPU times (in seconds) required to perform a single realisation of a model simulation. Technical specifications of computers used to perform the simulations are indicated in File 3.1.

C.6 Supplementary files, movies, figures and tables

File 3.1 Technical specifications of the computers used to perform simulations in this work. The file is available for download at https://github.com/daria-stepanova/PhD_thesis_supplementary_materials.

Movie 3.1 A simulation movie showing different pattern configurations explored by the CG system in a small 2D cell monolayer. The movie is the complete animation of the simulation snapshots shown in Figure 3.9 of the main text. This movie demonstrates how the spatial distribution of cells with two phenotypes changes over time in the CG system due to phenotype switches in individual cells. The colour bar indicates the levels of Delta. For this simulation, the interaction radius and system size were fixed at $R_s = 15\mu m$ and $\Omega = 100$, respectively; the values of the remaining parameters were fixed at the values given in Table C.1. The movie is available for download at https://github.com/daria-stepanova/PhD_thesis_supplementary_materials.

Movie 3.2 A simulation movie showing the emergence of robust pattern configurations in simulations of the CG system. The movie is the complete animation of the simulation snapshot shown in Figure 3.10 of the main text. This movie illustrates the emergence of a robust spatial pattern in the dynamics of the CG system at long times. Due to the exploration of different pattern configurations, the CG system settles on a configuration whose total propensity, P , is small. Thus, the mean waiting time for a phenotype switch for this pattern (given by $1/P$) tends to infinity and it becomes robust to any further phenotype switches. The lattice site highlighted in cyan indicates the position of a cell whose dynamics are shown in Figures 3.10C and 3.10D. The colour bar indicates the levels of Delta. For this simulation, the interaction radius and system size were fixed at $R_s = 15\mu m$ and $\Omega = 1000$, respectively; the values of all remaining parameters were fixed at the values given in Table C.1. The movie is available for download at https://github.com/daria-stepanova/PhD_thesis_supplementary_materials.

Movie 3.3 A simulation movie showing different pattern configurations explored by the CG system in a branching network. The movie is the complete animation of the simulation snapshots shown in Figure C.7. It illustrates the evolution of the CG system simulated on a branching network. The colour bar indicates the levels of Delta. For this simulation, the interaction radius and system size were fixed at $R_s = 15\mu m$ and $\Omega = 100$, respectively; the values of the remaining parameters were fixed at the values given in Table C.1. The movie is available for download at https://github.com/daria-stepanova/PhD_thesis_supplementary_materials.

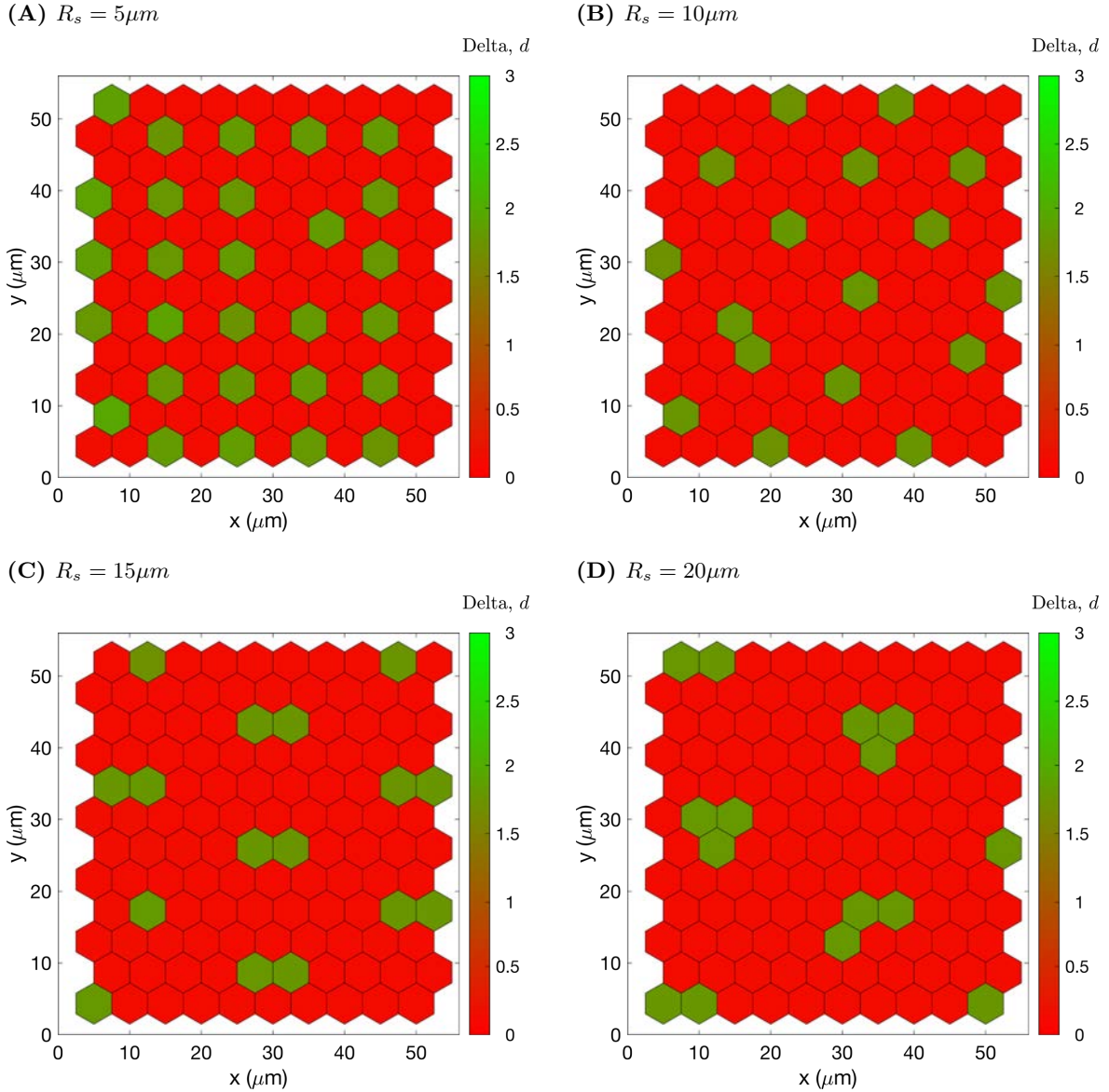


Figure C.4. A series of plots showing how the spatial patterns, generated by the VEGF-Delta-Notch signalling in a cell monolayer, become more clustered as the interaction radius, R_s , increases. For these simulations, the interaction radius is fixed at (A) $R_s = 5\mu m$; (B) $R_s = 10\mu m$; (C) $R_s = 15\mu m$; (D) $R_s = 20\mu m$. The system size is fixed at, $\Omega = 100$; the rest of the parameter values were fixed as indicated in Table C.1. The colour bar indicates the levels of Delta, d , in each cell.

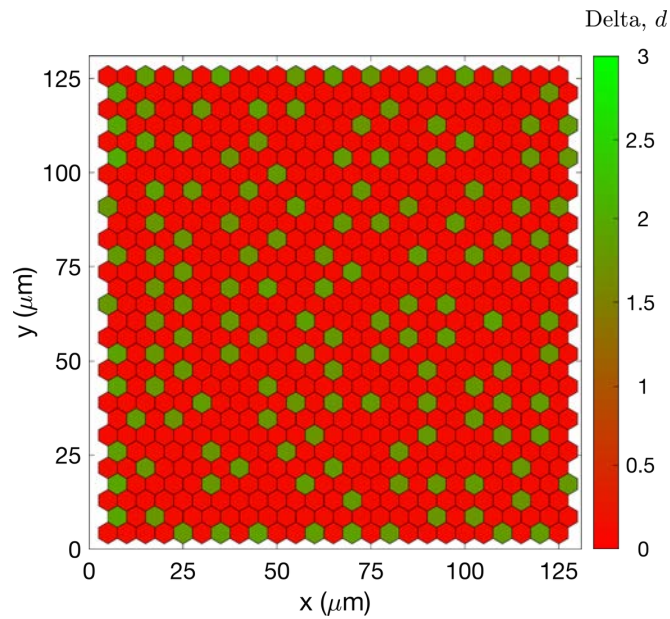


Figure C.5. Initial configuration of a cell monolayer for numerical simulation. The size of the monolayer is 25×29 voxels. The colour bar indicates the initial levels of Delta, d , in each cell.

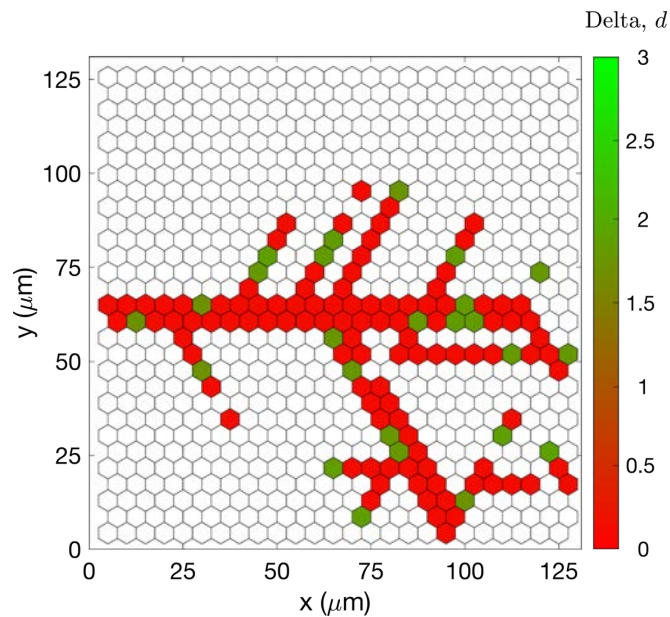


Figure C.6. Initial setup configuration of a branching network for numerical simulation. We extracted this configuration from a simulation of the angiogenesis model (Chapter 2). The colour bar indicates the level of Delta, d . Voxels without cells are left white in the plot.

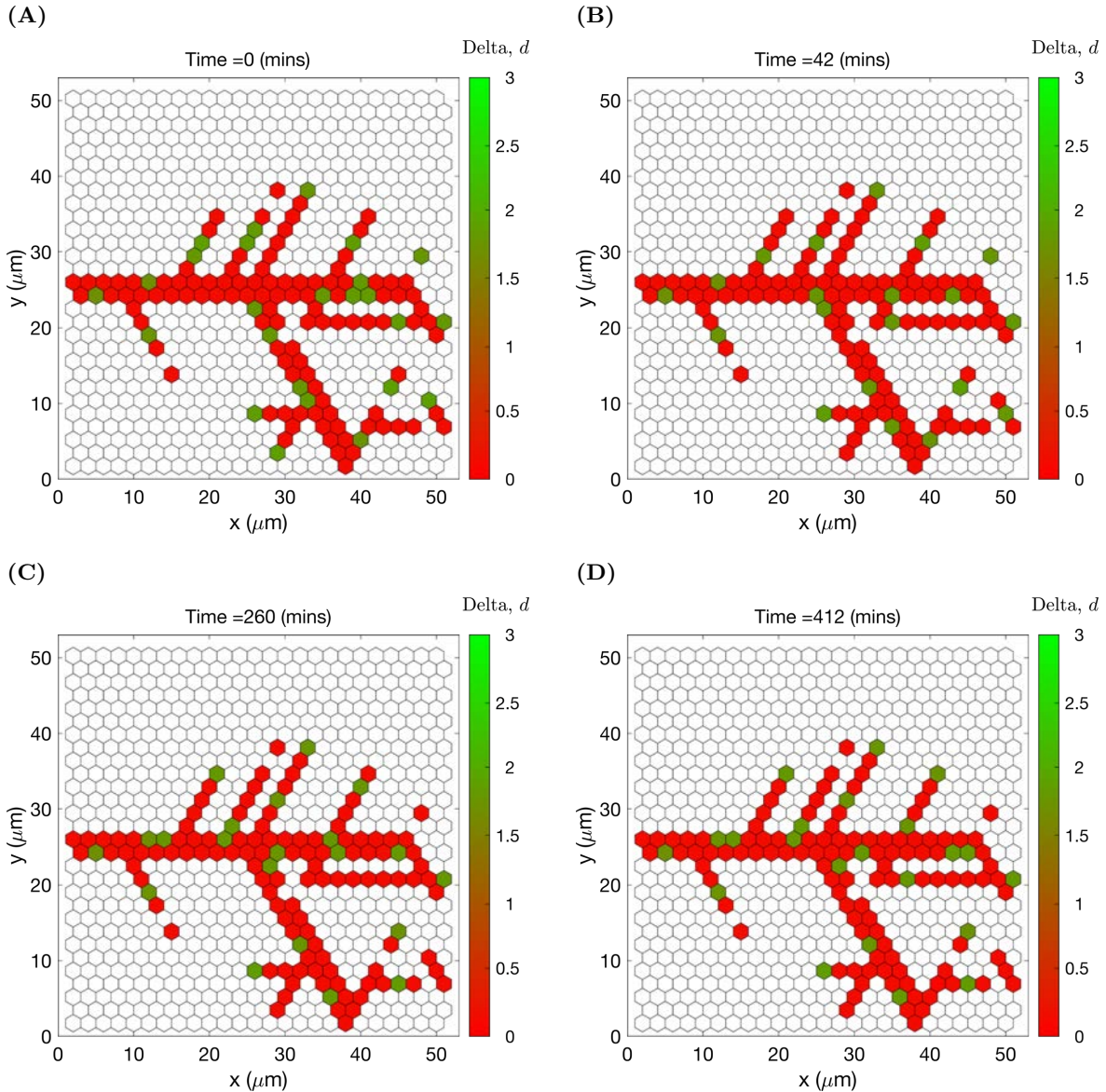


Figure C.7. A series of plots illustrating the time evolution of the phenotype patterning in a branching network in a typical simulation of the CG system for the multicellular VEGF-Delta-Notch signalling pathway. Time points (indicated in the title of each plot) are (A) $t = 0$, (B) $t = 42$, (C) $t = 260$, (D) $t = 412$ minutes. The colour bar indicates the levels of Delta, d , in each cell. For these simulations, the interaction radius and system size were fixed at $R_s = 15\mu\text{m}$ and $\Omega = 100$, respectively. The remaining parameter values were fixed as indicated in Table C.1.

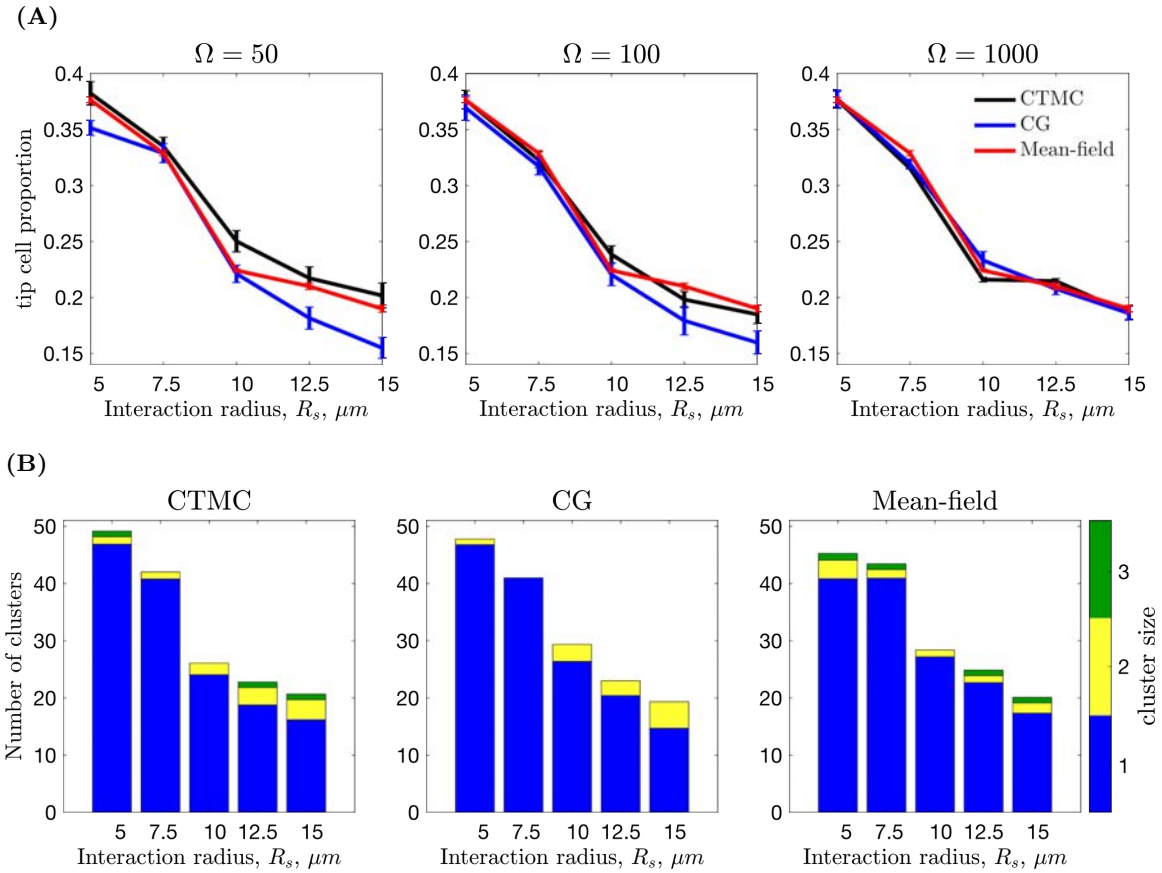


Figure C.8. Comparison of the dynamics of the multicellular VEGF-Delta-Notch model simulated on a branching network using the full stochastic (CTMC), CG, and mean-field descriptions. (A) The tip cell proportion as a function of the cell-to-cell interaction radius, R_s , for varying noise amplitude, $\epsilon = 1/\Omega$ (the value of Ω is indicated in the title of each plot), for the full stochastic CTMC (black), CG (blue) and mean-field (red) descriptions. (B) A series of bar plots showing how the long-time distribution of tip cell clusters changes as the interaction radius, R_s , varies for the full stochastic CTMC (left panel), CG (middle panel), and mean-field (right panel) systems. The number of single tip cells in the final pattern (i.e. at a fixed final simulation time) is shown in blue; the number of clusters with 2, and 3 adjacent tip cells is shown in yellow and green, respectively. For these simulations, we fixed $\Omega = 1000$ ($\epsilon = 0.001$). The results are averaged over 100 realisations. The remaining parameter values were fixed as indicated in Table C.1.

Parameter	Value
β_N	2.5, fixed in all figures.
β_D	4.0, fixed in all figures.
β_{R2}	4.0, fixed in all figures.
ρ_N	20.0, fixed in all figures.
ρ_{R2}	10.0, fixed in all figures.
$\lambda_{I,N}$	4.0, fixed in all figures.
$\lambda_{I,R2}$	0.0, fixed in all figures.
$\lambda_{R2^*,D}$	2.0, fixed in all figures.
n_N	2, fixed in all figures.
n_D	1, fixed in all figures.
n_{R2}	1, fixed in all figures.
η	0.5, fixed in all figures.
τ	5.0, fixed in all figures.
κ	4.0 for Figures 3.4, 3.5, 3.6 and C.1; 12.0 for all other figures and simulations.
v_{ext}	0.1 for Figures 3.4, 3.5,3.6, C.1; 1.25 for all other figures and simulations.
d_{ext}	0.2 for Figures 3.4, 3.5, 3.6 and C.1; $d_{ext} \in [0.0, 4.0]$ and the exact value is determined during the simulations (depending on the neighbourhood of each cell) for all other figures.
n_{ext}	0.5 for Figures 3.4, 3.5, 3.6 and C.1; $n_{ext} \in [0.0, 4.0]$ and the exact value is determined during the simulations (depending on the neighbourhood of each cell) for all other figures.
voxel width, h	5 μm in all multicellular simulations (hexagon width).
R_s	15 μm in Figures 3.9, 3.10 and C.7; for all other multicellular simulations R_s is indicated in the text and/or figure captions.
final simulation time, T_{final}	12000 mins for Figures 3.9 and C.4; $5 \cdot 10^{23}$ mins for Figure 3.10; 1500 mins for Figures 3.11, C.8 and 3.12; 9000 mins for Figure C.7.

Table C.1. Non-dimensional parameters of the VEGF-Delta-Notch system.

Appendix D

Supplementary materials for Chapter 4

D.1 Details on computational simulations

We used the non-dimensional VEGF-Delta-Notch system to coarse-grain the subcellular signalling of ECs (see Chapter 3). Thus, in this chapter, we use non-dimensional subcellular variables and parameters (see Table B.2). In Chapter 2, we used (dimensional) Delta levels to distinguish between tip and stalk cell phenotypes, which further determined the migration transition rate in Eq (2.7) and updates at the tissue scale (Eqs 2.16, (2.19) and (2.21)). Using the conversion factor indicated in Table B.2, we transformed these expressions (Eqs (2.7), 2.16, (2.19) and (2.21)) to non-dimensional Delta level, d . We performed a similar conversion procedure for the initial conditions of the subcellular proteins for each cell in simulations of the angiogenesis model (initial conditions for the dimensional variables are listed in Table B.9). We kept the rest of the parameters unchanged.

We performed simulations using two numerical setups described in Table D.3 and illustrated in Figure D.1. The values of the parameters specific to Chapter 4 are indicated in Table D.1. In addition, parameter values for the considered proliferation setups are shown in Table D.2.

D.2 Supplementary movies, figures and tables

Movie 4.1 Evolution of the quasipotential surface for the transition from stalk cell to tip cell for increasing levels of VEGF from 0 to 50 ng/ml ([0,12.5] in non-dimensional values). The monostability region in which the unique stable steady state corresponds to a tip (stalk) cell is coloured green (red) and the corresponding quasipotential, $Q(\text{stalk}, \text{tip}) = 0$ ($Q(\text{stalk}, \text{tip}) = \infty$). The colour bar indicates the value of the quasipotential. The movie is available for download at https://github.com/daria-stepanova/PhD_thesis_supplementary_materials.

Movie 4.2 Comparison of vascular networks generated by single realisations of the original and CG phenotype models for VEGF level of 5 ng/ml. Left panel: the original model; right panel: CG phenotype model. The colour bar indicates non-dimensional Delta levels, d , (green colour corresponds to tip cells, red – to stalk cells). Arrows indicate the configuration of the orientation landscape, l . The numerical simulation was performed

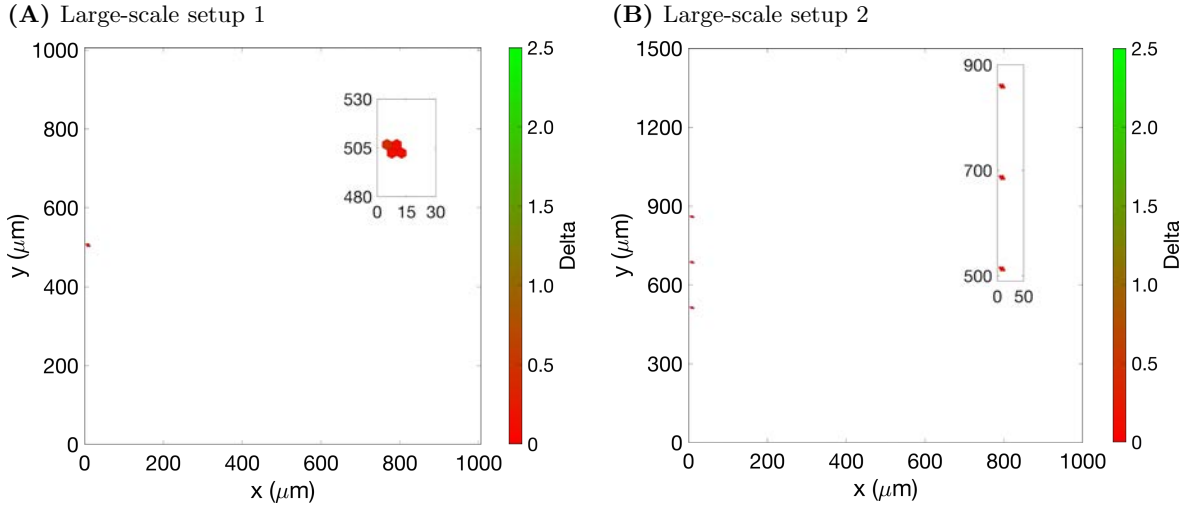


Figure D.1. Initial conditions for large-scale simulations. Initial placement of cells in (A) large-scale setup 1 and (B) large-scale setup 2 from Table D.3.

using **Setup 1** from Table B.10 with final simulation time $T_{max} = 2.5$. Parameter values are listed in Tables B.7 and B.8 for subcellular and cellular/tissue scales, respectively. The movie is available for download at https://github.com/daria-stepanova/PhD_thesis_supplementary_materials.

Movie 4.3 A large-scale simulation movie showing the growth of a vascular network at low proliferation rate. A single realisation of our large-scale model on a domain of $1000^2 \mu m^2$ with linear VEGF gradient of 1 – 10 ng/ml increasing in the direction of the x-axis. The movie is the complete animation of the simulation snapshot shown in Figure 4.9A of the main text. The colour bar indicates non-dimensional Delta levels, d , (green colour corresponds to tip cells, red – to stalk cells). We used proliferation setup 1 (slow cell cycle of 30-90 hours, see Table D.2). The numerical simulation was performed using large-scale setup 1 from Table D.3. Parameter values are listed in Table D.1 and final simulation time was fixed at $T_{max} = 72.0$ (equivalent to 25 days in real time units). The movie is available for download at https://github.com/daria-stepanova/PhD_thesis_supplementary_materials.

Movie 4.4 A large-scale simulation movie showing the growth of a vascular network at high proliferation rate. A single realisation of our large-scale model on a domain of $1000^2 \mu m^2$ with linear VEGF gradient of 1 – 10 ng/ml increasing in the direction of the x-axis. The movie is the complete animation of the simulation snapshot shown in Figure 4.9H of the main text. The colour bar indicates non-dimensional Delta levels, d , (green colour corresponds to tip cells, red – to stalk cells). We used proliferation setup 8 (short cell cycle of 12-20 hours, see Table D.2). The numerical simulation was performed using large-scale setup 1 from Table D.3. Parameter values are listed in Table D.1 and final simulation time was fixed

at $T_{max} = 72.0$ (equivalent to 25 days in real time units). The movie is available for download at https://github.com/daria-stepanova/PhD_thesis_supplementary_materials.

Movie 4.5 A large-scale simulation movie showing the growth of a vascular network with an initial condition of three main sprouts. A single realisation of our large-scale model on a domain of $1000 \times 1500 \mu m^2$ with a linear VEGF gradient of $1 - 10$ ng/ml increasing in the direction of the x-axis. The colour bar indicates non-dimensional Delta levels, \mathbf{d} , (green colour corresponds to tip cells, red – to stalk cells). We used proliferation setup 8 (short cell cycle of 12-20 hours, see Table D.2). The numerical simulation was performed using large-scale setup 2 from Table D.3. Parameter values are listed in Table D.1 and final simulation time was fixed at $T_{max} = 58.0$ (equivalent to 20 days in real time units). The movie is available for download at https://github.com/daria-stepanova/PhD_thesis_supplementary_materials.

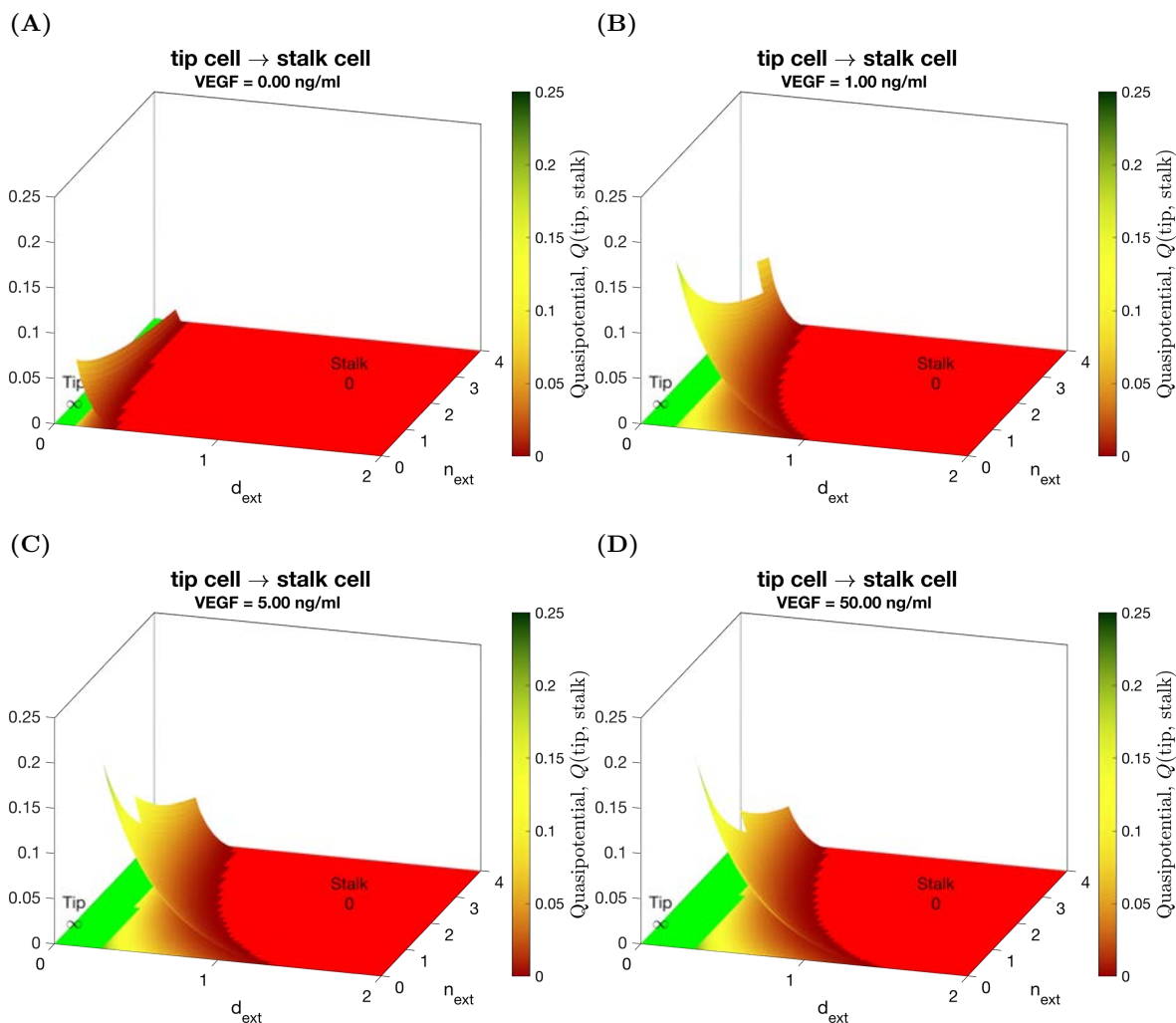


Figure D.2. An illustration of the evolution of the quasipotential surface for the transition from tip to stalk cell for increasing levels of VEGF. Quasipotential surfaces, $Q(\text{tip}, \text{stalk})$, for VEGF levels equal to (A) 0, (B) 1, (C) 5 and (D) 50 ng/ml (for simplicity of interpretation we indicate here dimensional values of the VEGF levels). The monostability region in which the unique stable steady state corresponds to a tip (stalk) cell is coloured green (red) and the corresponding quasipotential, $Q(\text{tip}, \text{stalk}) = \infty$ ($Q(\text{tip}, \text{stalk}) = 0$). The colour bar indicates the value of the quasipotential.

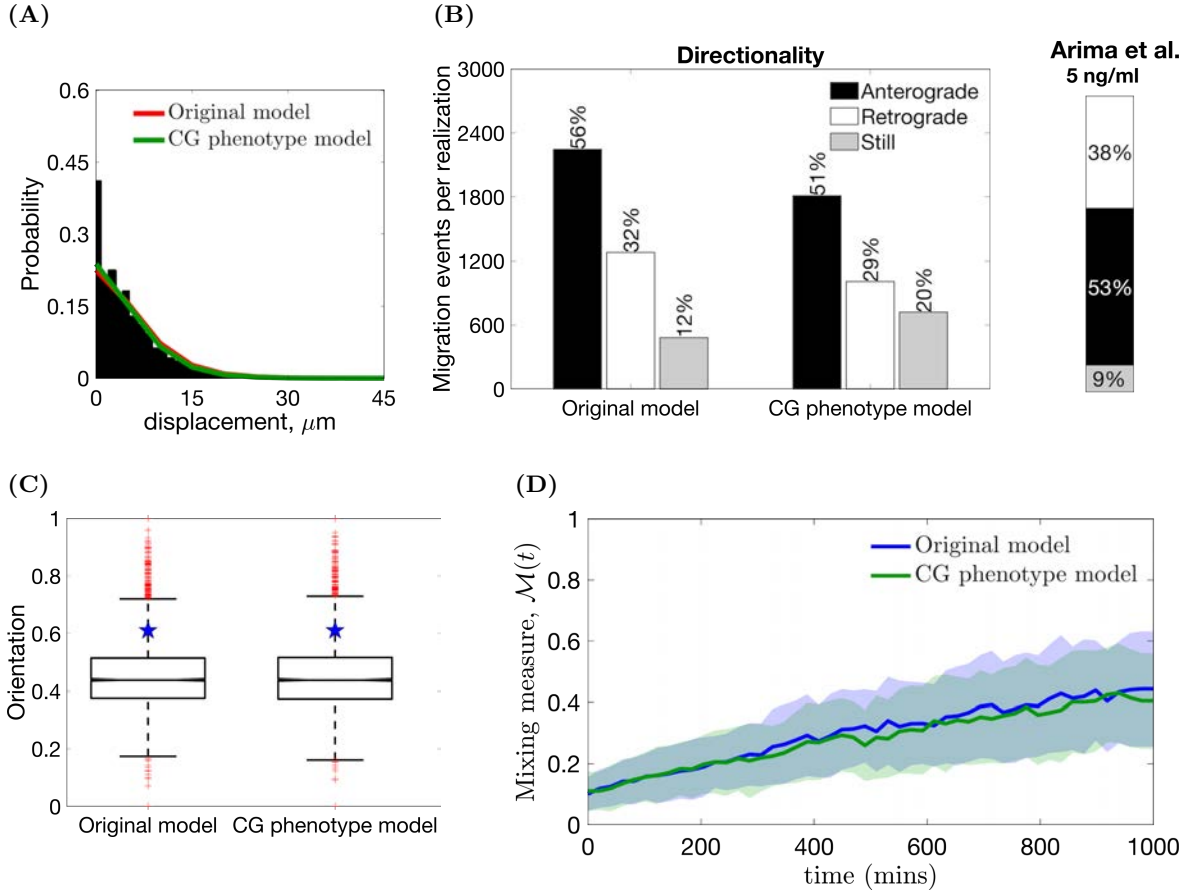


Figure D.3. Comparison of statistics extracted from simulations of original and CG phenotype models for VEGF = 50 ng/ml. (A) Histograms of cell displacements during a 15 minute time period for VEGF level of 50 ng/ml. The black histogram corresponds to the experimental data taken from the Supplementary Material of [10], the red (green) line corresponds to the displacement curves for simulations of the original (CG phenotype) model. (B) The directionality statistics for simulations of both models (left panel); the directionality statistics extracted from the experimental data in [4] (right panel). (C) Box plots of the orientation statistic extracted from simulations of both models. Red crosses indicate box plot outliers. Orientation statistics obtained from the experimental data from [4] are shown by blue stars on each box plot. (D) Temporal evolution of mixing measure, $\mathcal{M}(t)$, as a function of time (the mean value is indicated by a thick line and standard deviation is denoted by a colour band). All statistics were computed for 100 realisations. Numerical simulations were performed using **Setup 1** from Table B.10 and $T_{max} = 2.5$. Parameter values are listed in Tables B.7 and B.8 for subcellular and cellular/tissue scales, respectively.

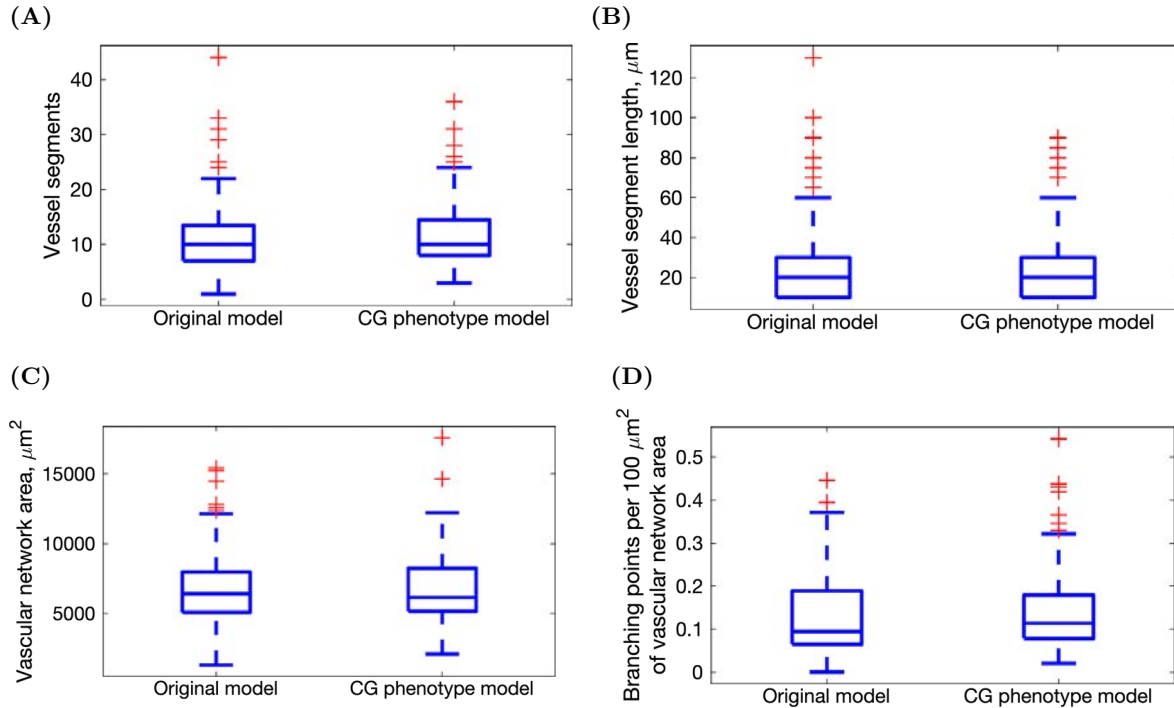


Figure D.4. Comparison of metrics for quantification of vascular network structure for the original and CG phenotype models for VEGF level of 50 ng/ml. (A) Number of vessel segments. (B) Vessel segment length (μm). (C) Vascular network area (μm^2). (D) Number of branching points per 100 μm^2 of vascular network area. Details of the definitions of these metrics can be found in Appendix B.5. In each box plot, the central line indicates the median, and the horizontal edges of the box represent the 25th and 75th percentiles (for the bottom and top edges, respectively). The outliers are indicated by the red cross symbols. Numerical simulation setup used is **Setup 1** from Table B.10 with final simulation time, $T_{max} = 2.5$. Parameter values are listed in Tables B.7 and B.8 for subcellular and cellular/tissue scales, respectively. Results are averaged over 100 realisations.

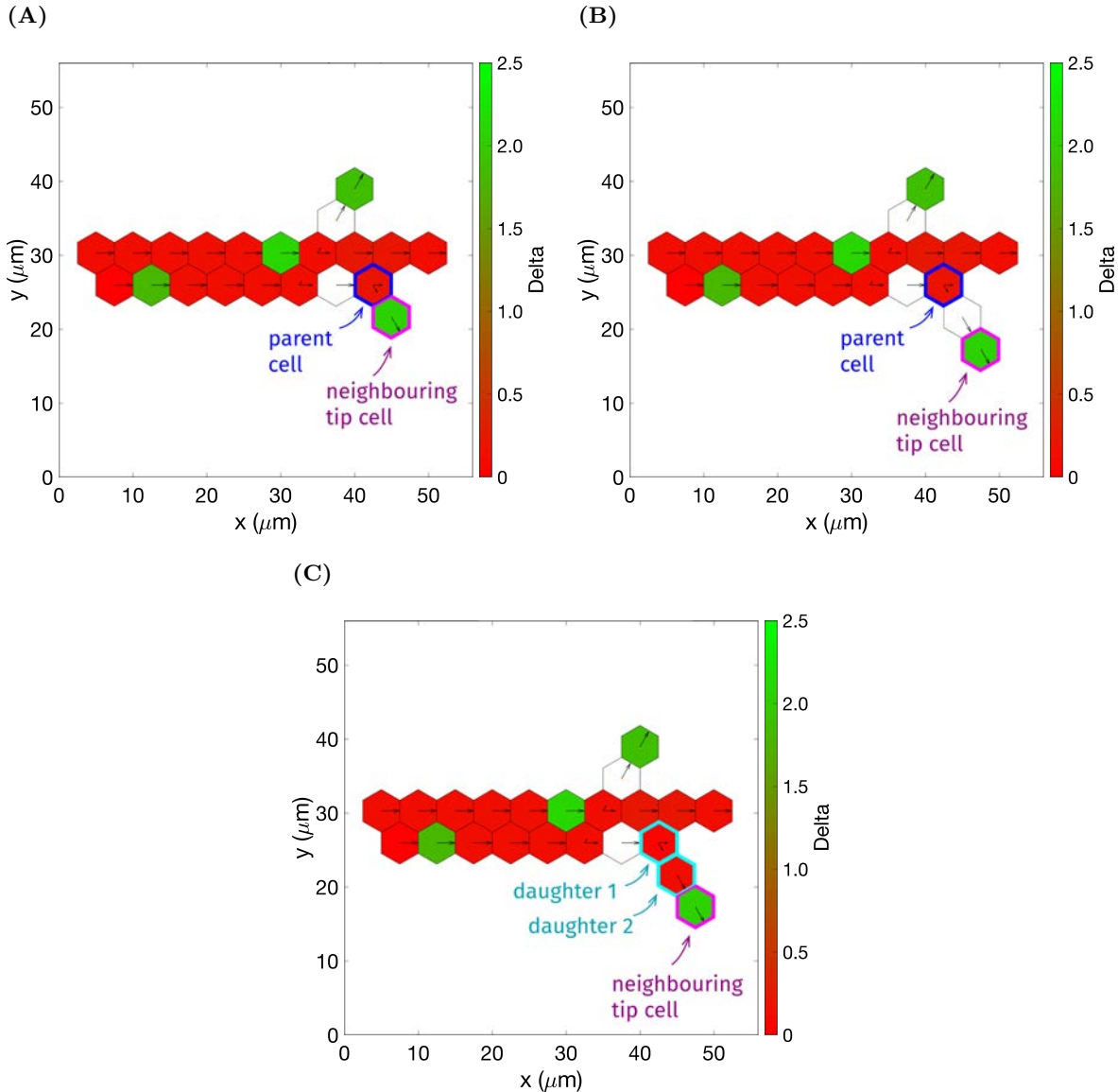


Figure D.5. An illustration of a cell division event in a simulation of our model on a small lattice. (A) Original configuration of the vascular network prior to cell division. A cell proliferation event occurs in a voxel highlighted in blue (parent cell). (B) Division direction, s_{div} , in this event coincides with the vessel elongation direction (downward-right). Since the voxel in this direction is occupied by a neighbouring tip cell (outlined in magenta), this tip cell is pushed forward in the same direction, freeing a voxel for cell division. (C) Cell division occurs and two daughter cells (highlighted in cyan) are placed in the lattice.

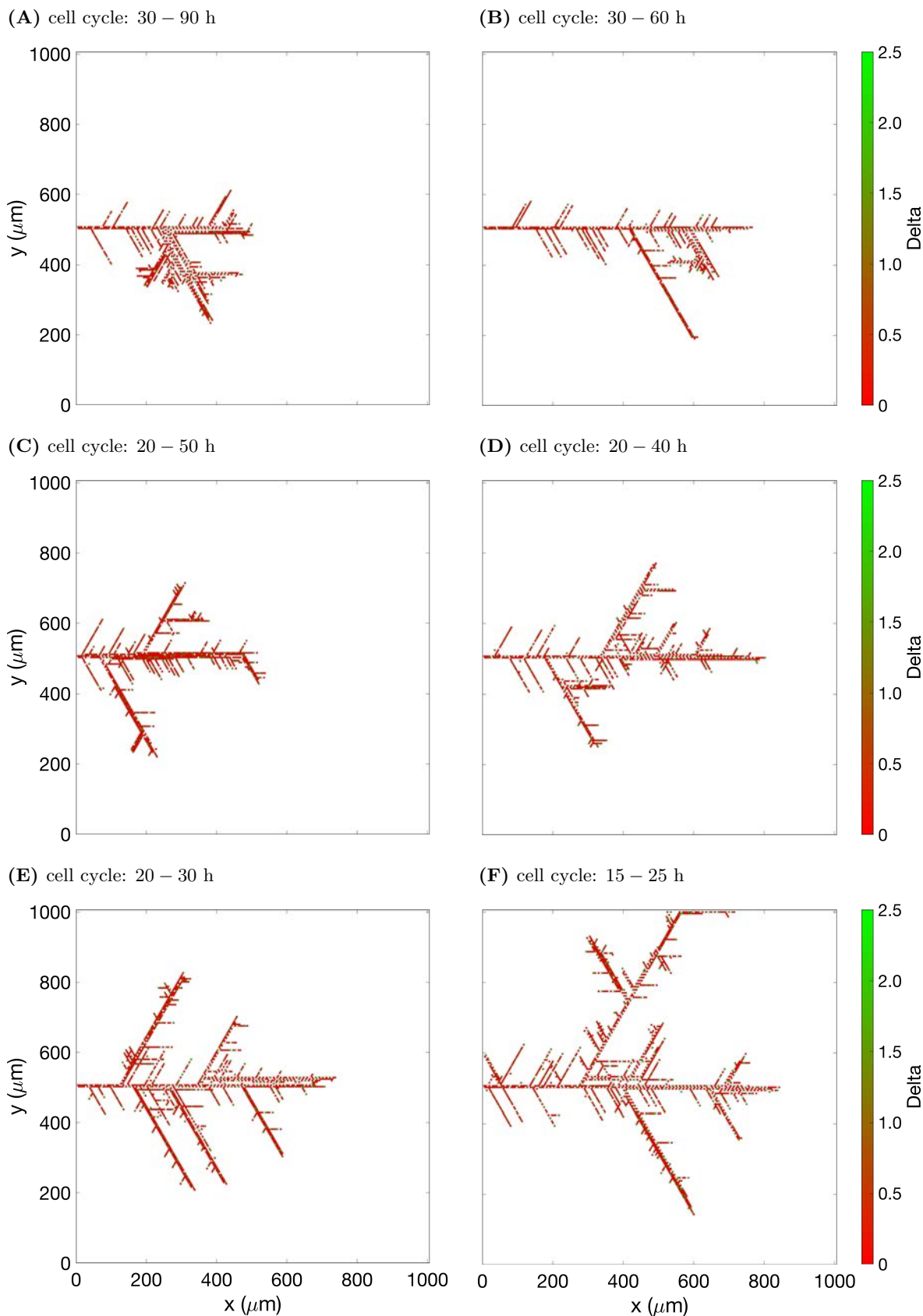


Figure D.6. (Continuation on the next page.)

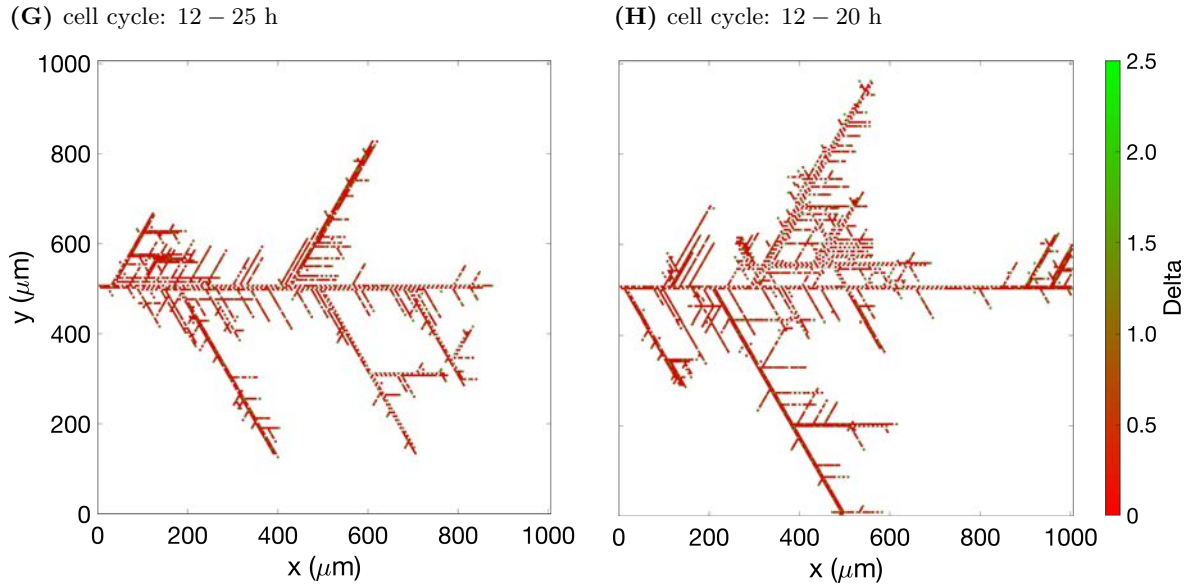


Figure D.6. Effects of cell proliferation on vasculature expansion. Single realisations of our model on a large domain of $1000^2 \mu\text{m}^2$ with a linear VEGF gradient of $1 - 5 \text{ ng/ml}$ increasing in the direction of the x-axis. Proliferation setups (see Table D.2) determining cell cycle duration are indicated in the title of each panel. The numerical simulations were performed using large-scale setup 1 from Table D.3. Parameter values are listed in Table D.1 and final simulation time was fixed at $T_{max} = 72.0$ (equivalent to 25 days in real time units).

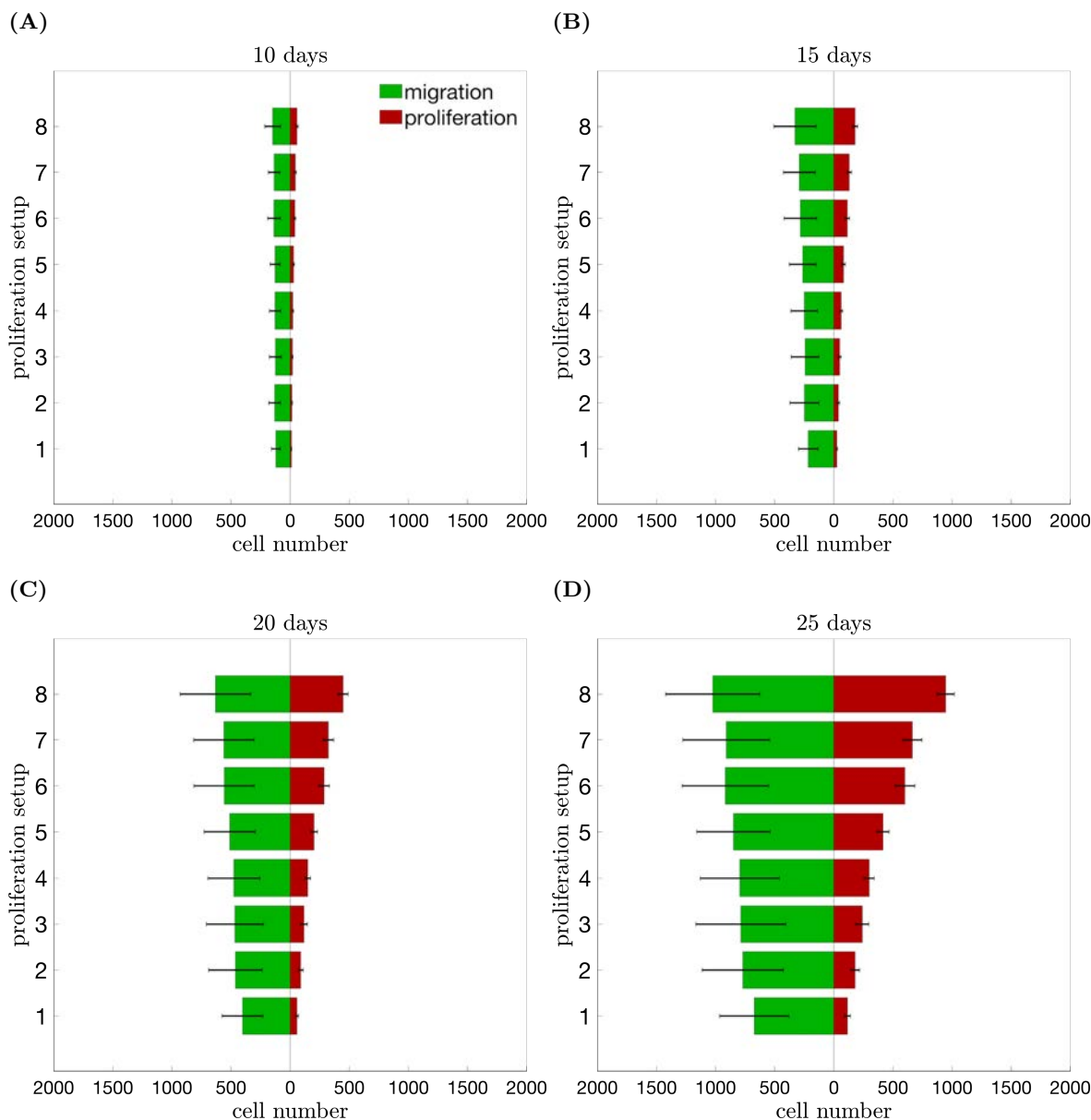


Figure D.7. Proliferation contribution to the overall cell supply into the network for simulations in VEGF gradient, where VEGF level increases from 1 to 5 ng/ml. The bar plot provides a breakdown of cell supply into growing vasculatures due to migration from the sprout base (shown in green) and cell proliferation (shown in red) at (A) 10 days; (A) 15 days; (A) 20 days; (A) 25 days. The black error bars indicate standard deviation for the proliferation contribution. The vertical axis indicates proliferation setups (see Table D.2); the horizontal axis shows mean cell number. All results are averaged over 100 realisations. The numerical simulations were performed using large-scale setup 1 from Table D.3. Parameter values are listed in Table D.1.

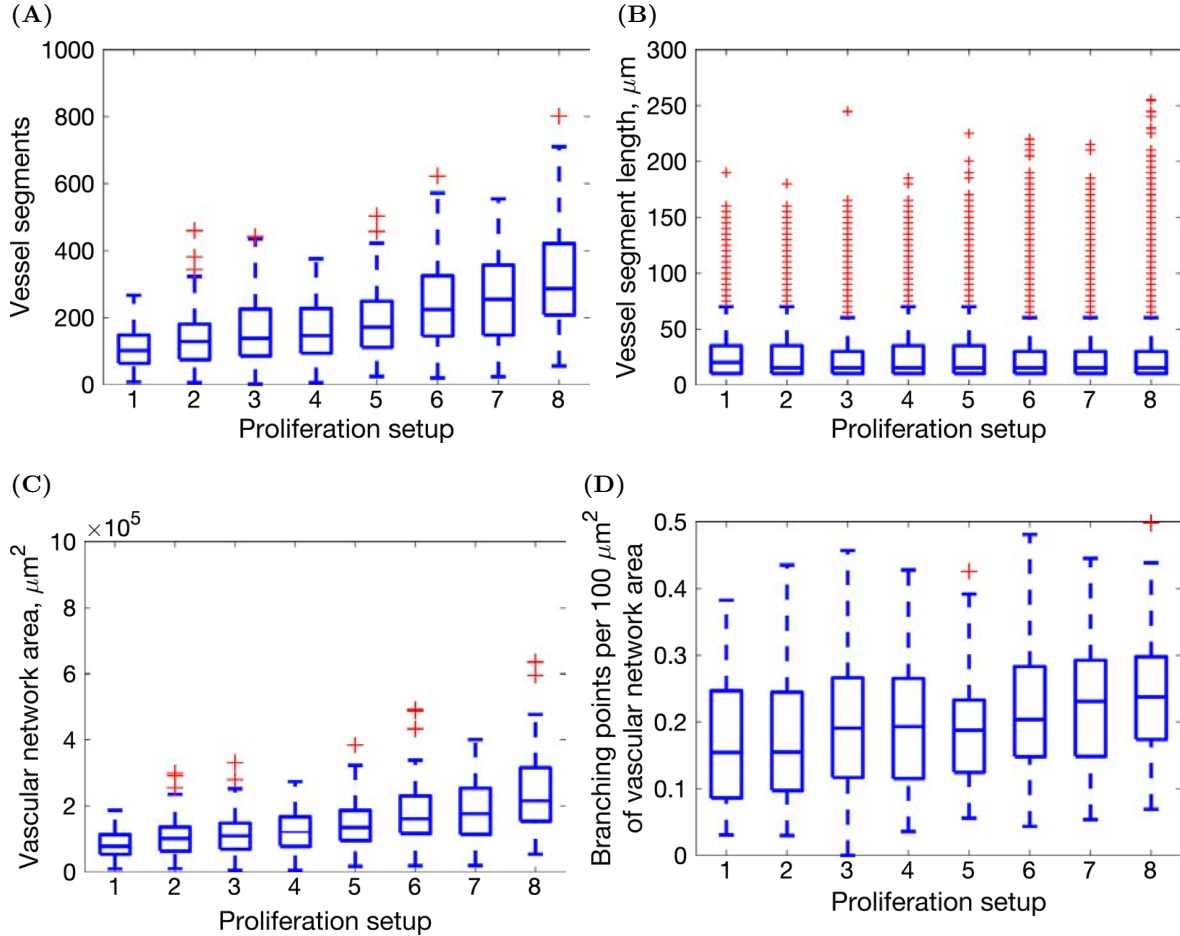


Figure D.8. Network quantification metrics for large-scale simulations in VEGF gradient, where VEGF level increases from 1 to 5 ng/ml. (A) Number of vessel segments. **(B)** Vessel segment length (μm). **(C)** Vascular network area (μm^2). **(D)** Number of branching points per $100 \mu\text{m}^2$ of vascular network area. Details of definitions of these metrics can be found in Appendix B.5. In each box plot, the central line indicates the median, and the horizontal edges of the box represent the 25th and 75th percentiles (for the bottom and top edges, respectively). The outliers are indicated by the red cross symbols. All results are averaged over 100 realisations. Proliferation setups are listed in Table D.2. The numerical simulations were performed using large-scale setup 1 from Table D.3. Parameter values are listed in Table D.1 and final simulation time was fixed at $T_{max} = 72.0$ (equivalent to 25 days in real time units).

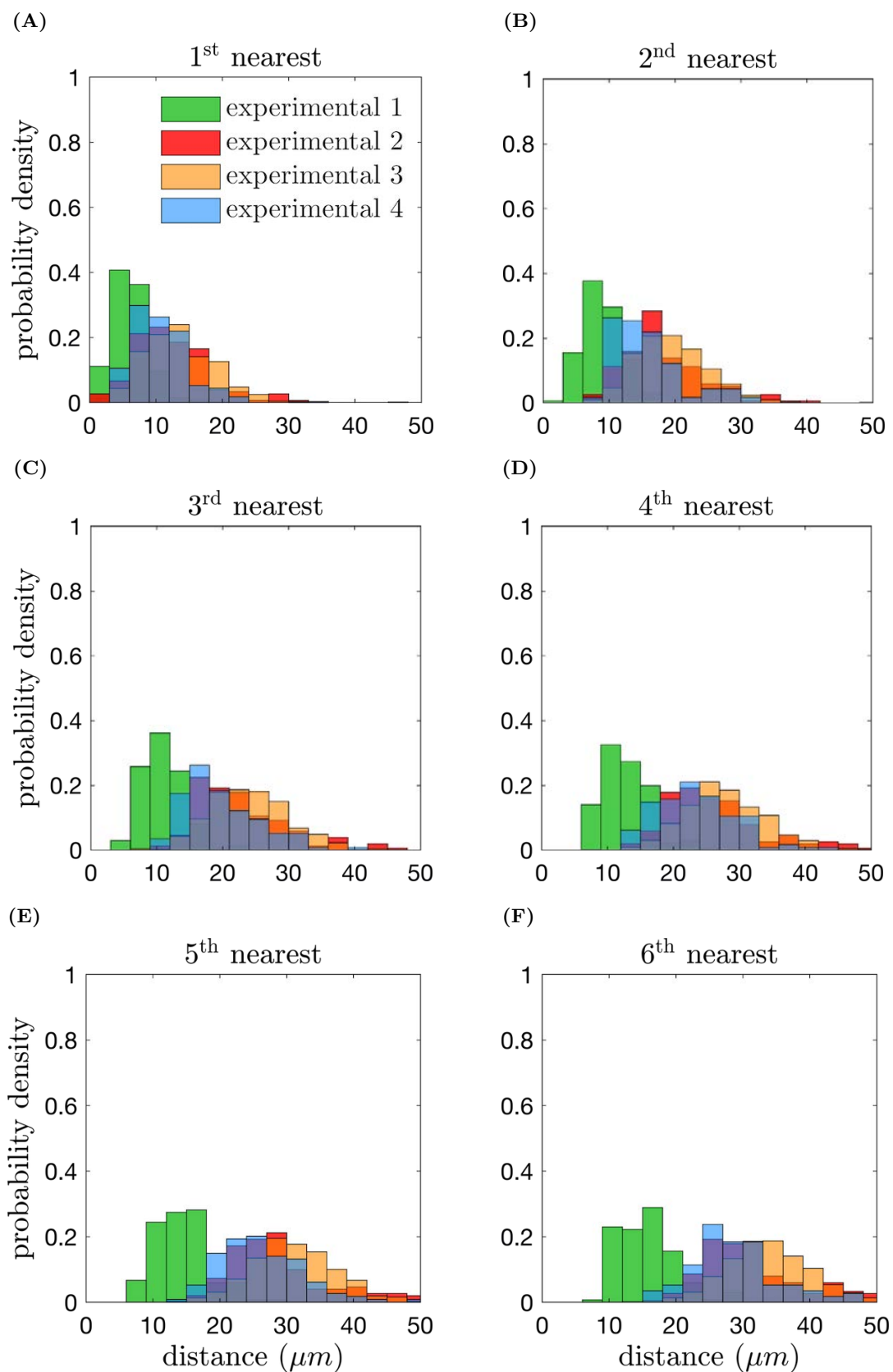


Figure D.9. (Caption on the next page.)

Figure D.9. A comparison of distributions of distances between cell nuclei obtained from experimental data. Colour code: experimental 1 (green): Fig. 3c (control) [3], 135 cells; experimental 2 (red): Fig. 1f (control) [212], 151 cells; experimental 3 (orange): Fig. 1a (control) [45], 881 cells; experimental 4 (blue): Figure 4 B (control) [213], 114 cells. The panels correspond to the distance to the **(A)** nearest; **(B)** 2nd nearest; **(C)** 3rd nearest; **(D)** 4th nearest; **(E)** 5th nearest; **(F)** 6th nearest neighbouring cell from a focal cell.

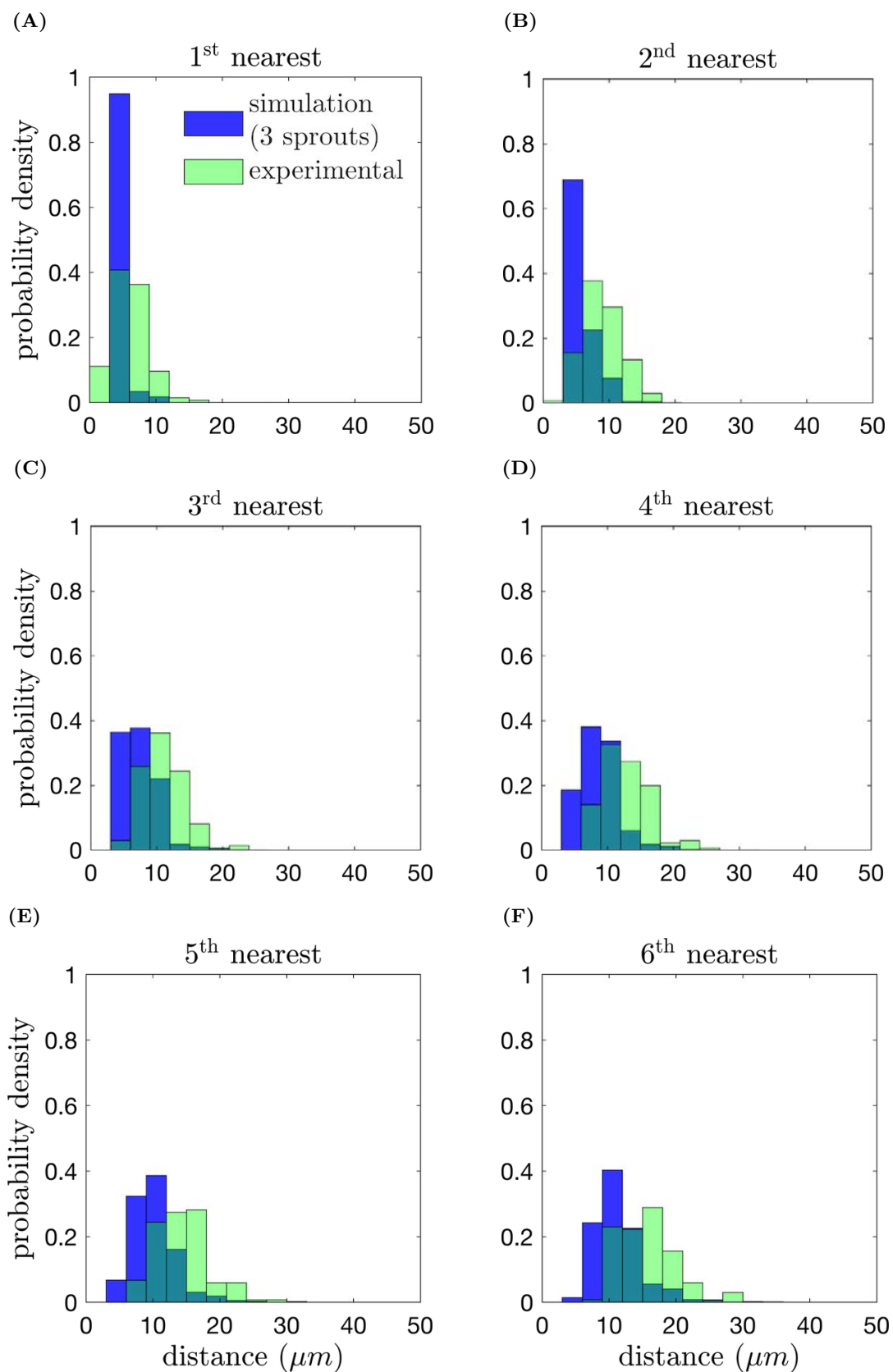


Figure D.10. (Caption on the next page.)

Figure D.10. A comparison of distributions of distances between cell nuclei obtained from simulations of our model, with the initial condition of three main sprouts, and experimental data. The distributions of distances extracted from our simulations are indicated in blue, while those corresponding to experimental data (obtained from Fig. 3c (control) in [3]) are shown in green. The panels correspond to the distance to the (A) nearest; (B) 2nd nearest; (C) 3rd nearest; (D) 4th nearest; (E) 5th nearest; (F) 6th nearest neighbouring cell from a focal cell. Simulation results are averaged over 5 realisations. The experimental results obtained from [3] are averaged over 135 cells. The numerical simulations were performed using large-scale setup 2 from Table D.3 and proliferation setup 8 from Table D.2 (see Movie 4.5 for an animation of a representative simulation). Parameter values are listed in Table D.1 and final simulation time was fixed at $T_{max} = 58.0$ (equivalent to 20 days in real time units).

Parameter	Value	Interpretation
r_{act}^{cycle}	0.1	Cell cycle duration, Eq (4.1).
r_{deact}^{cycle}	0.3	
s_{act}	30.0	
s_{deact}	40.0	
$T_{min}^{cycle}, T_{min}^{cycle}$	Specified in Table D.2.	
s_{BM}	30.0	BM inhibition of cell cycle, Eq (4.2).
m_{BM}	0.9	
D_{min}	0.2	BM inhibition of cell migration, Eq (4.8).
D_{max}	0.5	
γ_{min}	0.3	Baseline BM assembly, Eq (4.7).

Table D.1. Parameter values used in large-scale simulations. Here we list only parameter values used for the model extension to large-scale simulations (introduced in Chapter 4). The rest of the model parameters are fixed as in the previous simulations (parameter values of the subcellular scale are indicated in Table C.1; parameter values of the cellular and tissue scales are listed in Table B.8).

Proliferation setup	T_{min}^{cycle}	T_{max}^{cycle}
1.	30	90
2.	30	60
3.	20	50
4.	20	40
5.	20	30
6.	15	25
7.	12	25
8.	12	20

Table D.2. Proliferation setups. Minimum and maximum cell cycle durations (see Eq (4.1)). All values are indicated in hours.

Set-up	Specifications	Figures
large-scale setup 1	$N_I^x = 200, N_I^y = 231$ $\mathcal{I}_{init} = \{i = (i_x, i_y)^T : i_x = 1, 2, i_y = 115, 116\}$ $\mathcal{I}_{VP} = \{i = (1, i_y)^T : i_y = 115, 116\}$ $s_{init} = r$ $c_{init} = 0.0, m_{init} = 1.0$ VEGF gradient of 1-5 ng/ml: $v_{ext}(i_x, i_y) = 0.25 + 1.0 \frac{i_x}{N_I^x}$; VEGF gradient of 1-10 ng/ml: $v_{ext}(i_x, i_y) = 0.25 + 2.25 \frac{i_x}{N_I^x}$. This corresponds to a linear VEGF gradient increasing along the x -axis.	Figures 4.8,4.9, 4.10, 4.11, 4.12, D.6, D.7, D.8.
large-scale setup 2	$N_I^x = 200, N_I^y = 347$ $\mathcal{I}_{init} = \{i = (i_x, i_y)^T : i_x = 1, 2,$ $i_y = 118, 119, 158, 159, 198, 199\}$ $\mathcal{I}_{VP} = \{i = (1, i_y)^T : i_y = 118, 119, 158, 159, 198, 199\}$ $s_{init} = r$ $c_{init} = 0.0, m_{init} = 1.0$ VEGF gradient of 1-10 ng/ml: $v_{ext}(i_x, i_y) = 0.25 + 2.25 \frac{i_x}{N_I^x}$. This corresponds to a linear VEGF gradient increasing along the x -axis.	Figure D.10.

Table D.3. Setups of large-scale simulation experiments. For each numerical simulation setup we specify the lattice dimensions, N_I^x and N_I^y ; the set of indices corresponding to the vascular plexus, \mathcal{I}_{VP} ; the initial cell nuclei positions, \mathcal{I}_{init} ; the initial polarisation direction, s_{init} ; the initial ECM and BM concentrations, c_{init} and m_{init} , respectively; the VEGF distribution over the lattice, v_{ext} . Figure D.1 illustrates the initial conditions for the placement of cells for both setups.

Bibliography

- [1] P. Carmeliet, “Angiogenesis in life, disease and medicine”, *Nature*, vol. 438, no. 7070, pp. 932–936, 2005.
- [2] M. Potente and P. Carmeliet, “The link between angiogenesis and endothelial metabolism”, *Annual Review of Physiology*, vol. 79, pp. 43–66, 2017.
- [3] A. Angulo-Urarte, P. Casado, S. D. Castillo, P. Kobialka, M. P. Kotini, A. M. Figueiredo, P. Castel, V. Rajeeve, M. Mila-Guasch, J. Millan, C. Wiesner, H. Serra, L. Muixi, O. Casanovas, F. Viñals, M. Affolter, H. Gerhardt, S. Huvneers, H.-G. Belting, P. R. Cutillas, and M. Graupera, “Endothelial cell rearrangements during vascular patterning require pi3-kinase-mediated inhibition of actomyosin contractility”, *Nature Communications*, vol. 9, no. 1, p. 4826, 2018.
- [4] S. Arima, K. Nishiyama, T. Ko, Y. Arima, Y. Hakozaki, K. Sugihara, H. Koseki, Y. Uchijima, Y. Kurihara, and H. Kurihara, “Angiogenic morphogenesis driven by dynamic and heterogeneous collective endothelial cell movement”, *Development*, vol. 138, no. 21, pp. 4763–4776, 2011.
- [5] K. Bentley, C. A. Franco, A. Philippides, R. Blanco, M. Dierkes, V. Gebala, F. Stanchi, M. Jones, I. M. Aspalter, G. Cagna, S. Westrom, L. Claesson-Welsh, D. Vestweber, and H. Gerhardt, “The role of differential ve-cadherin dynamics in cell rearrangement during angiogenesis”, *Nature Cell Biology*, vol. 16, no. 309, pp. 309–321, 2014.
- [6] K. De Bock, M. Georgiadou, S. Schoors, A. Kuchnio, B. W. Wong, A. R. Cantelmo, A. Quaegebeur, B. Ghesquiere, S. Cauwenberghs, G. Eelen, *et al.*, “Role of pfkfb3-driven glycolysis in vessel sprouting”, *Cell*, vol. 154, no. 3, pp. 651–663, 2013.
- [7] B. Cruys, B. W. Wong, A. Kuchnio, D. Verdegem, A. R. Cantelmo, L.-C. Conradi, S. Vandekeere, A. Bouche, I. Cornelissen, S. Vinckier, R. M. H. Merks, E. Dejana, H. Gerhardt, M. Dewerchin, K. Bentley, and P. Carmeliet, “Glycolytic regulation of cell rearrangement in angiogenesis”, *Nature Communications*, vol. 7, p. 12240, 2016.
- [8] C. A. Franco, M. L. Jones, M. O. Bernabeu, I. Geudens, T. Mathivet, A. Rosa, F. M. Lopes, A. P. Lima, A. Ragab, R. T. Collins, *et al.*, “Dynamic endothelial cell rearrangements drive developmental vessel regression”, *PLoS Biology*, vol. 13, no. 4, 2015.
- [9] L. Jakobsson, C. A. Franco, K. Bentley, R. T. Collins, B. Ponsioen, I. M. Aspalter, I. Rosewell, M. Busse, G. Thurston, A. Medvinsky, *et al.*, “Endothelial cells dynamically compete for the tip cell position during angiogenic sprouting”, *Nature Cell Biology*, vol. 12, no. 10, p. 943, 2010.
- [10] K. Sugihara, K. Nishiyama, S. Fukuhara, A. Uemura, S. Arima, R. Kobayashi, A. Köhn-Luque, N. Mochizuki, T. Suda, H. Ogawa, *et al.*, “Autonomy and non-autonomy of angiogenic cell movements revealed by experiment-driven mathematical modeling”, *Cell Reports*, vol. 13, no. 9, pp. 1814–1827, 2015.
- [11] B. Ubezio, R. A. Blanco, I. Geudens, F. Stanchi, T. Mathivet, M. L. Jones, A. Ragab, K. Bentley, and H. Gerhardt, “Synchronization of endothelial dll4-notch dynamics switch blood vessels from branching to expansion”, *ELife*, vol. 5, e12167, 2016.
- [12] R. Vega, M. Carretero, R. D. Travasso, and L. L. Bonilla, “Notch signaling and taxis mechanisms regulate early stage angiogenesis: A mathematical and computational model”, *PLoS Computational Biology*, vol. 16, no. 1, e1006919, 2020.

- [13] P. H. Burri, R. Hlushchuk, and V. Djonov, "Intussusceptive angiogenesis: Its emergence, its characteristics, and its significance", *Developmental Dynamics: an official publication of the American Association of Anatomists*, vol. 231, no. 3, pp. 474–488, 2004.
- [14] S. J. Mentzer and M. A. Konerding, "Intussusceptive angiogenesis: Expansion and remodeling of microvascular networks", *Angiogenesis*, vol. 17, no. 3, pp. 499–509, 2014.
- [15] G. Eelen, P. de Zeeuw, L. Treps, U. Harjes, B. W. Wong, and P. Carmeliet, "Endothelial cell metabolism", *Physiological Reviews*, vol. 98, no. 1, pp. 3–58, 2018.
- [16] L.-K. Phng and H. Gerhardt, "Angiogenesis: A team effort coordinated by notch", *Developmental Cell*, vol. 16, no. 2, pp. 196–208, 2009.
- [17] U. R. Michaelis, "Mechanisms of endothelial cell migration", *Cellular and Molecular Life Sciences*, vol. 71, no. 21, pp. 4131–4148, 2014.
- [18] D. R. Senger and G. E. Davis, "Angiogenesis", *Cold Spring Harbor Perspectives in Biology*, vol. 3, no. 8, a005090, 2011.
- [19] J. Sottile, "Regulation of angiogenesis by extracellular matrix", *Biochimica et Biophysica Acta (BBA)-Reviews on Cancer*, vol. 1654, no. 1, pp. 13–22, 2004.
- [20] M. G. McCoy, J. M. Wei, S. Choi, J. P. Goerger, W. Zipfel, and C. Fischbach, "Collagen fiber orientation regulates 3d vascular network formation and alignment", *ACS Biomaterials Science & Engineering*, vol. 4, no. 8, pp. 2967–2976, 2018.
- [21] N. M. Myer and K. A. Myers, "Clasp1 regulates endothelial cell branching morphology and directed migration", *Biology Open*, vol. 6, no. 10, pp. 1502–1515, 2017.
- [22] M. S. Wietecha, W. L. Cerny, and L. A. DiPietro, "Mechanisms of vessel regression: Toward an understanding of the resolution of angiogenesis", *New Perspectives in Regeneration*, pp. 3–32, 2012.
- [23] I. Geudens and H. Gerhardt, "Coordinating cell behaviour during blood vessel formation", *Development*, vol. 138, no. 21, pp. 4569–4583, 2011.
- [24] A. Mukwaya, L. Jensen, and N. Lagali, "Relapse of pathological angiogenesis: Functional role of the basement membrane and potential treatment strategies", *Experimental & Molecular Medicine*, vol. 53, no. 2, pp. 189–201, 2021.
- [25] R. Blanco and H. Gerhardt, "Vegf and notch in tip and stalk cell selection", *Cold Spring Harbor Perspectives in Medicine*, vol. 3, no. 1, a006569, 2013.
- [26] H. Gerhardt, M. Golding, M. Fruttiger, C. Ruhrberg, A. Lundkvist, A. Abramsson, M. Jeltsch, C. Mitchell, K. Alitalo, D. Shima, *et al.*, "Vegf guides angiogenic sprouting utilizing endothelial tip cell filopodia", *The Journal of Cell Biology*, vol. 161, no. 6, pp. 1163–1177, 2003.
- [27] M. Hellström, L.-K. Phng, J. J. Hofmann, E. Wallgard, L. Coultas, P. Lindblom, J. Alva, A.-K. Nilsson, L. Karlsson, N. Gaiano, *et al.*, "Dll4 signalling through notch1 regulates formation of tip cells during angiogenesis", *Nature*, vol. 445, no. 7129, pp. 776–780, 2007.
- [28] S. Rousseau, F. Houle, H. Kotanides, L. Witte, J. Waltenberger, J. Landry, and J. Huot, "Vascular endothelial growth factor (vegf)-driven actin-based motility is mediated by vegfr2 and requires concerted activation of stress-activated protein kinase 2 (sapk2/p38) and geldanamycin-sensitive phosphorylation of focal adhesion kinase", *Journal of Biological Chemistry*, vol. 275, no. 14, pp. 10661–10672, 2000.
- [29] L. Lamalice, F. Le Boeuf, and J. Huot, "Endothelial cell migration during angiogenesis", *Circulation Research*, vol. 100, no. 6, pp. 782–794, 2007.
- [30] T. Watanabe, J. Noritake, and K. Kaibuchi, "Regulation of microtubules in cell migration", *Trends in Cell Biology*, vol. 15, no. 2, pp. 76–83, 2005.
- [31] C. A. Reinhart-King, M. Dembo, and D. A. Hammer, "The dynamics and mechanics of endothelial cell spreading", *Biophysical Journal*, vol. 89, no. 1, pp. 676–689, 2005.

- [32] A. N. Stratman, W. B. Saunders, A. Sacharidou, W. Koh, K. E. Fisher, D. C. Zawieja, M. J. Davis, and G. E. Davis, "Endothelial cell lumen and vascular guidance tunnel formation requires mt1-mmp-dependent proteolysis in 3-dimensional collagen matrices", *Blood*, vol. 114, no. 2, pp. 237–247, 2009.
- [33] N. D. Kirkpatrick, S. Andreou, J. B. Hoying, and U. Utzinger, "Live imaging of collagen remodeling during angiogenesis", *American Journal of Physiology-Heart and Circulatory Physiology*, vol. 292, no. 6, H3198–H3206, 2007.
- [34] Y. Du, S. C. Herath, Q.-g. Wang, D.-a. Wang, H. H. Asada, and P. C. Chen, "Three-dimensional characterization of mechanical interactions between endothelial cells and extracellular matrix during angiogenic sprouting", *Scientific Reports*, vol. 6, p. 21362, 2016.
- [35] R. S. Sopher, H. Tokash, S. Natan, M. Sharabi, O. Shelah, O. Tchaicheeyan, and A. Lesman, "Nonlinear elasticity of the ecm fibers facilitates efficient intercellular communication", *Biophysical Journal*, vol. 115, no. 7, pp. 1357–1370, 2018.
- [36] S. Pillay, H. M. Byrne, and P. K. Maini, "Modeling angiogenesis: A discrete to continuum description", *Physical Review E*, vol. 95, p. 012410, 2017.
- [37] K. Bentley, G. Mariggi, H. Gerhardt, and P. A. Bates, "Tipping the balance: Robustness of tip cell selection, migration and fusion in angiogenesis", *PLoS Computational Biology*, vol. 5, pp. 1–19, 2009.
- [38] W. Chen, P. Xia, H. Wang, J. Tu, X. Liang, X. Zhang, and L. Li, "The endothelial tip-stalk cell selection and shuffling during angiogenesis", *Journal of Cell Communication and Signaling*, pp. 1–11, 2019.
- [39] K. Herz, A. Becker, C. Shi, M. Ema, S. Takahashi, M. Potente, M. Hesse, B. K. Fleischmann, and D. Wenzel, "Visualization of endothelial cell cycle dynamics in mouse using the flt-1/egfp-anillin system", *Angiogenesis*, vol. 21, no. 2, pp. 349–361, 2018.
- [40] B. Zheng, G. Li, W. C. Chen, B. M. Deasy, J. B. Pollett, B. Sun, L. Drowley, B. Gharaibeh, A. Usas, B. Péault, *et al.*, "Human myogenic endothelial cells exhibit chondrogenic and osteogenic potentials at the clonal level", *Journal of Orthopaedic Research*, vol. 31, no. 7, pp. 1089–1095, 2013.
- [41] D. Form, B. Pratt, and J. Madri, "Endothelial cell proliferation during angiogenesis. in vitro modulation by basement membrane components.", *Laboratory Investigation; a Journal of Technical Methods and Pathology*, vol. 55, no. 5, pp. 521–530, 1986.
- [42] C. A. Frye and C. W. Patrick, "Isolation and culture of rat microvascular endothelial cells", *In Vitro Cellular & Developmental Biology-Animal*, vol. 38, no. 4, pp. 208–212, 2002.
- [43] M. D. Snead, A. Papapetropoulos, G. O. Carrier, and J. D. Catravas, "Isolation and culture of endothelial cells from the mesenteric vascular bed", *Methods in Cell Science*, vol. 17, no. 4, pp. 257–262, 1995.
- [44] A. Anagnostou, E. S. Lee, N. Kessimian, R. Levinson, and M. Steiner, "Erythropoietin has a mitogenic and positive chemotactic effect on endothelial cells.", *Proceedings of the National Academy of Sciences*, vol. 87, no. 15, pp. 5978–5982, 1990.
- [45] S. Pontes-Quero, M. Fernández-Chacón, W. Luo, F. F. Lunella, V. Casquero-Garcia, I. Garcia-Gonzalez, A. Hermoso, S. F. Rocha, M. Bansal, and R. Benedito, "High mitogenic stimulation arrests angiogenesis", *Nature Communications*, vol. 10, no. 1, pp. 1–16, 2019.
- [46] A. Lesman, D. Rosenfeld, S. Landau, and S. Levenberg, "Mechanical regulation of vascular network formation in engineered matrices", *Advanced Drug Delivery Reviews*, vol. 96, pp. 176–182, 2016.
- [47] E. Chavakis and S. Dimmeler, "Regulation of endothelial cell survival and apoptosis during angiogenesis", *Arteriosclerosis, Thrombosis, and Vascular Biology*, vol. 22, no. 6, pp. 887–893, 2002.
- [48] E. C. Watson, Z. L. Grant, and L. Coultas, "Endothelial cell apoptosis in angiogenesis and vessel regression", *Cellular and Molecular Life Sciences*, vol. 74, no. 24, pp. 4387–4403, 2017.
- [49] A. Zecchin, J. Kalucka, C. Dubois, and P. Carmeliet, "How endothelial cells adapt their metabolism to form vessels in tumors", *Frontiers in Immunology*, vol. 8, p. 1750, 2017.

- [50] G. Bergers and S. Song, “The role of pericytes in blood-vessel formation and maintenance”, *Neuro-Oncology*, vol. 7, no. 4, pp. 452–464, 2005.
- [51] A. B. Stundzia and C. J. Lumsden, “Stochastic simulation of coupled reaction–diffusion processes”, *Journal of Computational Physics*, vol. 127, no. 1, pp. 196–207, 1996.
- [52] M. Howard and A. D. Rutenberg, “Pattern formation inside bacteria: Fluctuations due to the low copy number of proteins”, *Physical Review Letters*, vol. 90, no. 12, p. 128 102, 2003.
- [53] E. Moro, “Hybrid method for simulating front propagation in reaction-diffusion systems”, *Phys. Rev. E.*, vol. 69, 060101(R), 2004.
- [54] D. Bernstein, “Simulating mesoscopic reaction-diffusion systems using the gillespie algorithm”, *Physical Review E*, vol. 71, no. 4, p. 041 103, 2005.
- [55] S. Engblom, L. Ferm, A. Hellander, and P. Lötstedt, “Simulation of stochastic reaction-diffusion processes on unstructured meshes”, *SIAM Journal on Scientific Computing*, vol. 31, no. 3, pp. 1774–1797, 2009.
- [56] M. B. Flegg, S. J. Chapman, and R. Erban, “The two-regime method for optimizing stochastic reaction–diffusion simulations”, *Journal of the Royal Society Interface*, vol. 9, no. 70, pp. 859–868, 2012.
- [57] A Hellander, S Hellander, and P Lotstedt, “Coupled mesoscopic and microscopic simulation of reaction-diffusion processes in mixed dimensions”, *Multiscale Model. Sim.*, vol. 10, pp. 585–611, 2012.
- [58] B. Franz, M. B. Flegg, S. J. Chapman, and R. Erban, “Multiscale reaction-diffusion algorithms: Pde-assisted brownian dynamics”, *SIAM Journal on Applied Mathematics*, vol. 73, no. 3, pp. 1224–1247, 2013.
- [59] F. Spill, P. Guerrero, T. Alarcon, P. K. Maini, and H. M. Byrne, “Mesoscopic and continuum modelling of angiogenesis”, *Journal of Mathematical Biology*, vol. 70, no. 3, pp. 485–532, 2015.
- [60] P. Guerrero, H. M. Byrne, P. K. Maini, and T. Alarcón, “From invasion to latency: Intracellular noise and cell motility as key controls of the competition between resource-limited cellular populations”, *J. Math. Biol.*, vol. 72, pp. 123–156, 2015.
- [61] C. A. Yates and M. B. Flegg, “The pseudo-compartment method for coupling partial differential equation and compartment-based models of diffusion”, *Journal of The Royal Society Interface*, vol. 12, no. 106, 2015, ISSN: 1742-5689.
- [62] D. T. Gillespie, L. R. Petzold, and E. Seitaridou, “Validity conditions for stochastic chemical kinetics in diffusion-limited systems”, *The Journal of Chemical Physics*, vol. 140, no. 5, 02B604.1, 2014.
- [63] S. A. Isaacson, “A convergent reaction-diffusion master equation”, *The Journal of Chemical Physics*, vol. 139, no. 5, p. 054 101, 2013.
- [64] J. Elf and M. Ehrenberg, “Spontaneous separation of bi-stable biochemical systems into spatial domains of opposite phases”, *Systems Biology*, vol. 1, no. 2, pp. 230–236, 2004.
- [65] D. T. Gillespie, “A general method for numerically simulating the stochastic time evolution of coupled chemical reactions”, *Journal of Computational Physics*, vol. 22, no. 4, pp. 403–434, 1976.
- [66] S. Bernard, “How to build a multiscale model in biology”, *Acta Biotheoretica*, vol. 61, no. 3, pp. 291–303, 2013.
- [67] T. S. Deisboeck, Z. Wang, P. Macklin, and V. Cristini, “Multiscale cancer modeling”, *Annual Review of Biomedical Engineering*, vol. 13, pp. 127–155, 2011.
- [68] A. Deutsch, P. Friedl, L. Preziosi, and G. Theraulaz, *Multi-scale analysis and modelling of collective migration in biological systems*, 2020.
- [69] K. A. Rejniak and A. R. Anderson, “State of the art in computational modelling of cancer”, *Mathematical Medicine and Biology: A Journal of the IMA*, vol. 29, no. 1, pp. 1–2, 2012.

- [70] T. Heck, M.-M. Vaeyens, and H. Van Oosterwyck, “Computational models of sprouting angiogenesis and cell migration: Towards multiscale mechanochemical models of angiogenesis”, *Mathematical Modelling of Natural Phenomena*, vol. 10, no. 1, pp. 108–141, 2015.
- [71] R. Bardini, G. Politano, A. Benso, and S. Di Carlo, “Multi-level and hybrid modelling approaches for systems biology”, *Computational and Structural Biotechnology Journal*, vol. 15, pp. 396–402, 2017.
- [72] J. M. Osborne, A. Walter, S. Kershaw, G. Mirams, A. Fletcher, P. Pathmanathan, D. Gavaghan, O. Jensen, P. Maini, and H. Byrne, “A hybrid approach to multi-scale modelling of cancer”, *Philosophical Transactions of the Royal Society A: Mathematical, Physical and Engineering Sciences*, vol. 368, no. 1930, pp. 5013–5028, 2010.
- [73] M. Scianna, C. Bell, and L. Preziosi, “A review of mathematical models for the formation of vascular networks”, *Journal of Theoretical Biology*, vol. 333, pp. 174–209, 2013.
- [74] G. Vilanova, I. Colominas, and H. Gomez, “Computational modeling of tumor-induced angiogenesis”, *Archives of Computational Methods in Engineering*, vol. 24, no. 4, pp. 1071–1102, 2017.
- [75] N. V. Mantzaris, S. Webb, and H. G. Othmer, “Mathematical modeling of tumor-induced angiogenesis”, *Journal of Mathematical Biology*, vol. 49, no. 2, pp. 111–187, 2004.
- [76] D. Balding and D. McElwain, “A mathematical model of tumour-induced capillary growth”, *Journal of Theoretical Biology*, vol. 114, no. 1, pp. 53–73, 1985, ISSN: 0022-5193.
- [77] M. A. Chaplain and A. M. Stuart, “A model mechanism for the chemotactic response of endothelial cells to tumour angiogenesis factor”, *Mathematical Medicine and Biology: A Journal of the IMA*, vol. 10, no. 3, pp. 149–168, 1993.
- [78] H. Byrne and M. Chaplain, “Mathematical models for tumour angiogenesis: Numerical simulations and nonlinear wave solutions”, *Bulletin of Mathematical Biology*, vol. 57, no. 3, pp. 461–486, 1995, ISSN: 0092-8240.
- [79] B. Sleeman and I. Wallis, “Tumour induced angiogenesis as a reinforced random walk: Modelling capillary network formation without endothelial cell proliferation”, *Mathematical and Computer Modelling*, vol. 36, no. 3, pp. 339–358, 2002.
- [80] A. R. A. Anderson and M. A. J. Chaplain, “Continuous and discrete mathematical models of tumor-induced angiogenesis”, *Bulletin of Mathematical Biology*, vol. 60, pp. 857–899, 1998.
- [81] S. Tong and F. Yuan, “Numerical simulations of angiogenesis in the cornea”, *Microvascular Research*, vol. 61, no. 1, pp. 14–27, 2001.
- [82] M. Plank and B. Sleeman, “Lattice and non-lattice models of tumour angiogenesis”, *Bulletin of Mathematical Biology*, vol. 66, no. 6, pp. 1785–1819, 2004.
- [83] V. Capasso and D. Morale, “Stochastic modelling of tumour-induced angiogenesis”, *Journal of Mathematical Biology*, vol. 58, no. 1, pp. 219–233, 2009.
- [84] J. Folkman, “Tumor angiogenesis”, *Advances in Cancer Research*, vol. 19, pp. 331–358, 1974.
- [85] —, “The vascularization of tumors”, *Scientific American*, vol. 234, no. 5, pp. 58–73, 1976.
- [86] M. A. Gimbrone Jr, R. S. Cotran, S. B. Leapman, and J. Folkman, “Tumor growth and neovascularization: An experimental model using the rabbit cornea”, *Journal of the National Cancer Institute*, vol. 52, no. 2, pp. 413–427, 1974.
- [87] V. Muthukkaruppan and R. Auerbach, “Angiogenesis in the mouse cornea”, *Science*, vol. 205, no. 4413, pp. 1416–1418, 1979.
- [88] A. Deakin, “Model for initial vascular patterns in melanoma transplants.”, *Growth*, vol. 40, no. 2, pp. 191–201, 1976.
- [89] M. A. Chaplain and A. M. Stuart, “A mathematical model for the diffusion of tumour angiogenesis factor into the surrounding host tissue”, *Mathematical Medicine and Biology: A Journal of the IMA*, vol. 8, no. 3, pp. 191–220, 1991.

- [90] M. Chaplain, “The mathematical modelling of tumour angiogenesis and invasion”, *Acta Biotheoretica*, vol. 43, no. 4, pp. 387–402, 1995.
- [91] —, “Avascular growth, angiogenesis and vascular growth in solid tumours: The mathematical modelling of the stages of tumour development”, *Mathematical and Computer Modelling*, vol. 23, no. 6, pp. 47–87, 1996.
- [92] M. Orme and M. Chaplain, “A mathematical model of the first steps of tumour-related angiogenesis: Capillary sprout formation and secondary branching”, *Mathematical Medicine and Biology: A Journal of the IMA*, vol. 13, no. 2, pp. 73–98, 1996.
- [93] —, “Two-dimensional models of tumour angiogenesis and anti-angiogenesis strategies”, *Mathematical Medicine and Biology: A Journal of the IMA*, vol. 14, no. 3, pp. 189–205, 1997.
- [94] H. A. Levine, S. Pamuk, B. D. Sleeman, and M. Nilsen-Hamilton, “Mathematical modeling of capillary formation and development in tumor angiogenesis: Penetration into the stroma”, *Bulletin of Mathematical Biology*, vol. 63, no. 5, pp. 801–863, 2001.
- [95] M. Aubert, M. Chaplain, S. McDougall, A. Devlin, and C. Mitchell, “A continuum mathematical model of the developing murine retinal vasculature”, *Bulletin of Mathematical Biology*, vol. 73, no. 10, pp. 2430–2451, 2011.
- [96] J. A. Flegg, D. L. McElwain, H. M. Byrne, and I. W. Turner, “A three species model to simulate application of hyperbaric oxygen therapy to chronic wounds”, *PLoS Computational Biology*, vol. 5, no. 7, e1000451, 2009.
- [97] A. J. Connor, R. P. Nowak, E. Lorenzon, M. Thomas, F. Herting, S. Hoert, T. Quaiser, E. Shochat, J. Pitt-Francis, J. Cooper, *et al.*, “An integrated approach to quantitative modelling in angiogenesis research”, *Journal of The Royal Society Interface*, vol. 12, no. 110, p. 20150546, 2015.
- [98] H. Byrne and M. Chaplain, “Explicit solutions of a simplified model of capillary sprout growth during tumor angiogenesis”, *Applied Mathematics Letters*, vol. 9, no. 1, pp. 69–74, 1996.
- [99] D. Manoussaki, S. Lubkin, R. Vemon, and J. Murray, “A mechanical model for the formation of vascular networks in vitro”, *Acta Biotheoretica*, vol. 44, no. 3, pp. 271–282, 1996.
- [100] M. Holmes and B. Sleeman, “A mathematical model of tumour angiogenesis incorporating cellular traction and viscoelastic effects”, *Journal of Theoretical Biology*, vol. 202, no. 2, pp. 95–112, 2000.
- [101] C. L. Stokes and D. A. Lauffenburger, “Analysis of the roles of microvessel endothelial cell random motility and chemotaxis in angiogenesis”, *Journal of Theoretical Biology*, vol. 152, no. 3, pp. 377–403, 1991.
- [102] N. Hill and D.-P. Häder, “A biased random walk model for the trajectories of swimming microorganisms”, *Journal of Theoretical Biology*, vol. 186, no. 4, pp. 503–526, 1997.
- [103] M. A. Chaplain, “Mathematical modelling of angiogenesis”, *Journal of Neuro-Oncology*, vol. 50, no. 1, pp. 37–51, 2000.
- [104] S. R. McDougall, A. Anderson, M. Chaplain, and J. Sherratt, “Mathematical modelling of flow through vascular networks: Implications for tumour-induced angiogenesis and chemotherapy strategies”, *Bulletin of Mathematical Biology*, vol. 64, no. 4, pp. 673–702, 2002.
- [105] A. Stephanou, S. R. McDougall, A. R. Anderson, and M. A. Chaplain, “Mathematical modelling of flow in 2d and 3d vascular networks: Applications to anti-angiogenic and chemotherapeutic drug strategies”, *Mathematical and Computer Modelling*, vol. 41, no. 10, pp. 1137–1156, 2005.
- [106] S. R. McDougall, A. R. Anderson, and M. A. Chaplain, “Mathematical modelling of dynamic adaptive tumour-induced angiogenesis: Clinical implications and therapeutic targeting strategies”, *Journal of Theoretical Biology*, vol. 241, no. 3, pp. 564–589, 2006.
- [107] S. R. McDougall, M. A. Chaplain, A. Stéphanou, and A. R. Anderson, “Modelling the impact of pericyte migration and coverage of vessels on the efficacy of vascular disrupting agents”, *Mathematical Modelling of Natural Phenomena*, vol. 5, no. 1, pp. 163–202, 2010.

- [108] K. Bartha and H. Rieger, “Vascular network remodeling via vessel cooption, regression and growth in tumors”, *Journal of Theoretical Biology*, vol. 241, no. 4, pp. 903–918, 2006, issn: 0022-5193.
- [109] S. Sun, M. F. Wheeler, M. Obeyesekere, and C. Patrick Jr, “Multiscale angiogenesis modeling using mixed finite element methods”, *Multiscale Modeling & Simulation*, vol. 4, no. 4, pp. 1137–1167, 2005.
- [110] F. Milde, M. Bergdorf, and P. Koumoutsakos, “A hybrid model for three-dimensional simulations of sprouting angiogenesis”, *Biophysical Journal*, vol. 95, no. 7, pp. 3146–3160, 2008.
- [111] K.-A. Norton and A. S. Popel, “Effects of endothelial cell proliferation and migration rates in a computational model of sprouting angiogenesis”, *Scientific Reports*, vol. 6, no. 1, pp. 1–10, 2016.
- [112] H. Perfahl, B. D. Hughes, T. Alarcón, P. K. Maini, M. C. Lloyd, M. Reuss, and H. M. Byrne, “3d hybrid modelling of vascular network formation”, *Journal of Theoretical Biology*, vol. 414, pp. 254–268, 2017.
- [113] W. D. Martinson, H. M. Byrne, and P. K. Maini, “Evaluating snail-trail frameworks for leader-follower behavior with agent-based modeling”, *Physical Review E*, vol. 102, no. 6, p. 062417, 2020.
- [114] J. A. Grogan, A. J. Connor, B. Markelc, R. J. Muschel, P. K. Maini, H. M. Byrne, and J. M. Pitt-Francis, “Microvessel chaste: An open library for spatial modeling of vascularized tissues”, *Biophysical Journal*, vol. 112, no. 9, pp. 1767–1772, 2017.
- [115] M. R. Owen, I. J. Stamper, M. Muthana, G. W. Richardson, J. Dobson, C. E. Lewis, and H. M. Byrne, “Mathematical modeling predicts synergistic antitumor effects of combining a macrophage-based, hypoxia-targeted gene therapy with chemotherapy”, *Cancer Research*, vol. 71, no. 8, pp. 2826–2837, 2011.
- [116] H. A. Harrington, M. Maier, L. Naidoo, N. Whitaker, and P. G. Kevrekidis, “A hybrid model for tumor-induced angiogenesis in the cornea in the presence of inhibitors”, *Mathematical and Computer Modelling*, vol. 46, no. 3-4, pp. 513–524, 2007.
- [117] T. Jackson and X. Zheng, “A cell-based model of endothelial cell migration, proliferation and maturation during corneal angiogenesis”, *Bulletin of Mathematical Biology*, vol. 72, no. 4, pp. 830–868, 2010.
- [118] M. Watson, S. McDougall, M. Chaplain, A. Devlin, and C. Mitchell, “Dynamics of angiogenesis during murine retinal development: A coupled in vivo and in silico study”, *Journal of The Royal Society Interface*, vol. 9, no. 74, pp. 2351–2364, 2012.
- [119] K. Bentley, H. Gerhardt, and P. A. Bates, “Agent-based simulation of notch-mediated tip cell selection in angiogenic sprout initialisation”, *Journal of Theoretical Biology*, vol. 250, no. 1, pp. 25–36, 2008.
- [120] G. Costa, K. I. Harrington, H. E. Lovegrove, D. J. Page, S. Chakravartula, K. Bentley, and S. P. Herbert, “Asymmetric division coordinates collective cell migration in angiogenesis”, *Nature Cell Biology*, vol. 18, no. 12, pp. 1292–1301, 2016.
- [121] B. Zakirov, G. Charalambous, R. Thuret, I. M. Aspalter, K. Van-Vuuren, T. Mead, K. Harrington, E. R. Regan, S. P. Herbert, and K. Bentley, “Active perception during angiogenesis: Filopodia speed up notch selection of tip cells in silico and in vivo”, *Philosophical Transactions of the Royal Society B*, vol. 376, no. 1821, p. 20190753, 2021.
- [122] F. Graner and J. A. Glazier, “Simulation of biological cell sorting using a two-dimensional extended potts model”, *Physical Review Letters*, vol. 69, no. 13, p. 2130, 1992.
- [123] J. A. Glazier and F. Graner, “Simulation of the differential adhesion driven rearrangement of biological cells”, *Physical Review E*, vol. 47, no. 3, p. 2128, 1993.
- [124] A. L. Bauer, T. L. Jackson, and Y. Jiang, “A cell-based model exhibiting branching and anastomosis during tumor-induced angiogenesis”, *Biophysical Journal*, vol. 92, no. 9, pp. 3105–3121, 2007.
- [125] —, “Topography of extracellular matrix mediates vascular morphogenesis and migration speeds in angiogenesis”, *PLoS Computational Biology*, vol. 5, no. 7, e1000445, 2009.

- [126] A. Shamloo and S. C. Heilshorn, “Matrix density mediates polarization and lumen formation of endothelial sprouts in vegf gradients”, *Lab on a Chip*, vol. 10, no. 22, pp. 3061–3068, 2010.
- [127] R. M. Merks, E. D. Perryn, A. Shirinifard, and J. A. Glazier, “Contact-inhibited chemotaxis in de novo and sprouting blood-vessel growth”, *PLoS Computational Biology*, vol. 4, no. 9, e1000163, 2008.
- [128] R. F. M. van Oers, E. G. Rens, D. J. LaValley, C. A. Reinhart-King, and R. M. H. Merks, “Mechanical cell-matrix feedback explains pairwise and collective endothelial cell behavior in vitro”, *PLoS Computational Biology*, vol. 10, no. 8, pp. 1–14, Aug. 2014.
- [129] J. T. Daub and R. M. Merks, “A cell-based model of extracellular-matrix-guided endothelial cell migration during angiogenesis”, *Bulletin of Mathematical Biology*, vol. 75, no. 8, pp. 1377–1399, 2013.
- [130] S. E. M. Boas and R. M. H. Merks, “Tip cell overtaking occurs as a side effect of sprouting in computational models of angiogenesis”, *BMC Systems Biology*, vol. 9, no. 1, p. 86, 2015.
- [131] A. Shirinifard, J. S. Gens, B. L. Zaitlen, N. J. Poplawski, M. Swat, and J. A. Glazier, “3d multi-cell simulation of tumor growth and angiogenesis”, *PloS One*, vol. 4, no. 10, e7190, 2009.
- [132] T. Alarcón, H. M. Byrne, and P. K. Maini, “A cellular automaton model for tumour growth in inhomogeneous environment”, *Journal of Theoretical Biology*, vol. 225, no. 2, pp. 257–274, 2003.
- [133] —, “A multiple scale model of tumour growth”, *Multiscale Model. Sim.*, vol. 3, pp. 440–475, 2005.
- [134] T. Alarcón, M. R. Owen, H. M. Byrne, and P. K. Maini, “Multiscale modelling of tumour growth and therapy: The influence of vessel normalisation on chemotherapy”, *Computational and Mathematical Methods in Medicine*, vol. 7, no. 2-3, pp. 85–119, 2006.
- [135] H. M. Byrne, M. R. Owen, T. Alarcon, J. Murphy, and P. K. Maini, “Modelling the response of vascular tumours to chemotherapy: A multiscale approach”, *Mathematical Models and Methods in Applied Sciences*, vol. 16, no. supp01, pp. 1219–1241, 2006.
- [136] M. R. Owen, T. Alarcón, H. M. Byrne, and P. K. Maini, “Angiogenesis and vascular remodelling in normal and cancerous tissues”, *J. Math. Biol.*, vol. 58, pp. 689–721, 2009.
- [137] H. Perfahl, H. M. Byrne, T. Chen, V. Estrella, T. Alarcón, A. Lapin, R. A. Gatenby, R. J. Gillies, M. C. Lloyd, P. K. Maini, M. Reuss, and M. R. Owen, “Multiscale Modelling of Vascular Tumour Growth in 3D: The Roles of Domain Size and Boundary Conditions”, *PLoS One*, vol. 6, e14790, 2011.
- [138] P. Macklin, S. McDougall, A. R. A. Anderson, M. A. J. Chaplain, V. Cristini, and J. Lowengrub, “Multi-scale modelling and non-linear simulation of vascular tumour growth”, *J. Math. Biol.*, vol. 58, pp. 765–798, 2009.
- [139] C. M. Phillips, E. A. Lima, R. T. Woodall, A. Brock, and T. E. Yankeelov, “A hybrid model of tumor growth and angiogenesis: In silico experiments”, *Plos One*, vol. 15, no. 4, e0231137, 2020.
- [140] R. D. M. Travasso, E. Corvera Poiré, M. Castro, J. C. Rodriguez-Manzaneque, and A. Hernandez-Machado., “Tumour angiogenesis and vascular patterning: a mathematical model”, *PLoS One*, vol. 6, e19989, 2011.
- [141] G. Vilanova, I. Colominas, and H. Gomez, “Coupling of discrete random walks and continuous modeling for three-dimensional tumor-induced angiogenesis”, *Computational Mechanics*, vol. 53, no. 3, pp. 449–464, 2014.
- [142] M. Moreira-Soares, R. Coimbra, L. Rebelo, J. Carvalho, and R. D. M. Travasso, “Angiogenic factors produced by hypoxic cells are a leading driver of anastomoses in sprouting angiogenesis – a computational study”, *Scientific Reports*, vol. 8, p. 8726, 2018.
- [143] G. Vilanova, I. Colominas, and H. Gomez, “A mathematical model of tumour angiogenesis: Growth, regression and regrowth”, *Journal of The Royal Society Interface*, vol. 14, no. 126, p. 20160918, 2017.
- [144] J. Xu, G. Vilanova, and H. Gomez, “A mathematical model coupling tumour growth and angiogenesis”, *PLoS One*, vol. 11, e0149422, 2016.

- [145] J. S. Lowengrub, H. B. Frieboes, F. Jin, Y. L. Chuang, X. Li, P. Macklin, S. M. Wise, and V. Cristini, “Non-linear modelling of cancer: bridging the gap between cells and tumours”, *Nonlinearity*, vol. 23, R1–R91, 2010.
- [146] M. Chaplain, S. McDougall, and A. Anderson, “Mathematical modelling of tumor-induced angiogenesis”, *Annual Review of Biomedical Engineering*, vol. 8, no. 1, pp. 233–257, 2006, PMID: 16834556.
- [147] D. Stepanova, H. M. Byrne, P. K. Maini, and T. Alarcón, “A multiscale model of complex endothelial cell dynamics in early angiogenesis”, *PLoS Computational Biology*, vol. 17, no. 1, e1008055, 2021.
- [148] E. H. Sage and R. B. Vernon, “Regulation of angiogenesis by extracellular matrix: The growth and the glue.”, *Journal of Hypertension. Supplement: Official Journal of the International Society of Hypertension*, vol. 12, no. 10, S145–52, 1994.
- [149] C. W. Gardiner, “The escape time in nonpotential systems”, *J. Stat. Phys.*, vol. 30, pp. 157–177, 1983.
- [150] R. S. Maier and D. L. Stein, “A scaling theory of bifurcations in the symmetric weak-noise escape problem”, *J. Stat. Phys.*, vol. 83, pp. 291–357, 1996.
- [151] R. Guantes and J. F. Poyatos, “Multistable Decision Switches for Flexible Control of Epigenetic Differentiation”, *PLoS Computational Biology*, vol. 4, no. 11, 2008.
- [152] R. Perez-Carrasco, P. Guerrero, J. Briscoe, and K. M. Page, “Intrinsic noise profoundly alters the dynamics and steady state of the morphogen controlled bistable genetic switches”, *PLoS Computational Biology*, vol. 12, e1005154, 2016.
- [153] D. Sprinzak, A. Lakhanpal, L. LeBon, L. A. Santat, M. E. Fontes, G. A. Anderson, J. Garcia-Ojalvo, and M. B. Elowitz, “Cis-interactions between notch and delta generate mutually exclusive signalling states”, *Nature*, vol. 465, no. 7294, p. 86, 2010.
- [154] D. Sprinzak, A. Lakhanpal, L. LeBon, J. Garcia-Ojalvo, and M. B. Elowitz, “Mutual inactivation of notch receptors and ligands facilitates developmental patterning”, *PLoS Computational Biology*, vol. 7, no. 6, e1002069, 2011.
- [155] M. Boareto, M. K. Jolly, M. Lu, J. N. Onuchic, C. Clementi, and E. Ben-Jacob, “Jagged–delta asymmetry in notch signaling can give rise to a sender/receiver hybrid phenotype”, *Proceedings of the National Academy of Sciences*, vol. 112, no. 5, E402–E409, 2015.
- [156] M. Boareto, M. K. Jolly, E. Ben-Jacob, and J. N. Onuchic, “Jagged mediates differences in normal and tumor angiogenesis by affecting tip-stalk fate decision”, *Proceedings of the National Academy of Sciences*, vol. 112, no. 29, E3836–E3844, 2015.
- [157] L. Venkatraman, E. R. Regan, and K. Bentley, “Time to decide? dynamical analysis predicts partial tip/stalk patterning states arise during angiogenesis”, *PLoS One*, vol. 11, pp. 1–23, 2016.
- [158] M. Lu, M. K. Jolly, H. Levine, J. N. Onuchic, and E. Ben-Jacob, “MicroRNA-based regulation of epithelial–hybrid–mesenchymal fate determination”, *Proceedings of the National Academy of Sciences*, vol. 110, no. 45, pp. 18 144–18 149, 2013.
- [159] E. A. Codling, M. J. Plank, and S. Benhamou, “Random walk models in biology”, *Journal of the Royal Society Interface*, vol. 5, no. 25, pp. 813–834, 2008.
- [160] A. P. J. Jansen, *An introduction to kinetic Monte Carlo simulations of surface reactions*. Springer, 2012, vol. 856.
- [161] K. J. Painter and T. Hillen, “Navigating the flow: Individual and continuum models for homing in flowing environments”, *Journal of the Royal Society Interface*, vol. 12, no. 112, p. 20 150 647, 2015.
- [162] T. Hillen, K. J. Painter, A. C. Swan, and A. D. Murtha, “Moments of von mises and fisher distributions and applications”, *Mathematical Biosciences & Engineering*, vol. 14, p. 673, 2017.
- [163] R. del Toro, C. Prahst, T. Mathivet, G. Siegfried, J. S. Kaminker, B. Larrivee, C. Breant, A. Duarte, N. Takakura, A. Fukamizu, *et al.*, “Identification and functional analysis of endothelial tip cell–enriched genes”, *Blood*, vol. 116, no. 19, pp. 4025–4033, 2010.

- [164] M. J. Siemerink, I. Klaassen, C. J. Van Noorden, and R. O. Schlingemann, “Endothelial tip cells in ocular angiogenesis: Potential target for anti-angiogenesis therapy”, *Journal of Histochemistry & Cytochemistry*, vol. 61, no. 2, pp. 101–115, 2013.
- [165] M. Papetti and I. M. Herman, “Mechanisms of normal and tumor-derived angiogenesis”, *American Journal of Physiology-Cell Physiology*, vol. 282, no. 5, pp. C947–C970, 2002.
- [166] M. K. Gupta and R.-Y. Qin, “Mechanism and its regulation of tumor-induced angiogenesis”, *World Journal of Gastroenterology: WJG*, vol. 9, no. 6, p. 1144, 2003.
- [167] M. Plank and B. Sleeman, “Tumour-induced angiogenesis: A review”, *Journal of Theoretical Medicine*, vol. 5, no. 3-4, pp. 137–153, 2003.
- [168] I. Barkefors, S. Le Jan, L. Jakobsson, E. Hejll, G. Carlson, H. Johansson, J. Jarvius, J. W. Park, N. L. Jeon, and J. Kreuger, “Endothelial cell migration in stable gradients of vascular endothelial growth factor a and fibroblast growth factor 2 effects on chemotaxis and chemokinesis”, *Journal of Biological Chemistry*, vol. 283, no. 20, pp. 13 905–13 912, 2008.
- [169] M. I. Dykman, T. Horita, and J. Ross, “Statistical distribution and stochastic resonance in a periodically driven chemical system”, *The Journal of Chemical Physics*, vol. 103, no. 3, pp. 966–972, 1995.
- [170] D. Stepanova, H. M. Byrne, P. K. Maini, and T. Alarcón, “A method to coarse-grain multi-agent stochastic systems with regions of multistability”, *arXiv preprint arXiv:2105.03398*, 2021.
- [171] P. Buske, J. Galle, N. Barker, G. Aust, H. Clevers, and M. Loeffler, “A comprehensive model of the spatio-temporal stem cell and tissue organisation in the intestinal crypt”, *PLoS Computational Biology*, vol. 7, no. 1, e1001045, 2011.
- [172] M. A. Chaplain, “Multiscale modelling of cancer: Micro-, meso- and macro-scales of growth and spread”, in *Approaching Complex Diseases*, Springer, 2020, pp. 149–168.
- [173] M. I. Freidlin and A. D. Wentzell, “Random perturbations”, in *Random perturbations of dynamical systems*, Springer, 1998, pp. 15–43.
- [174] R. de la Cruz, P. Guerrero, J. Calvo, and T. Alarcón, “Coarse-graining and hybrid methods for efficient simulation of stochastic multi-scale models of tumour growth”, *Journal of Computational Physics*, vol. 350, pp. 974–991, 2017.
- [175] R. De La Cruz, R. Perez-Carrasco, P. Guerrero, T. Alarcon, and K. M. Page, “Minimum action path theory reveals the details of stochastic transitions out of oscillatory states”, *Physical Review Letters*, vol. 120, no. 12, p. 128 102, 2018.
- [176] M. I. Dykman, E. Mori, J. Ross, and P. Hunt, “Large fluctuations and optimal paths in chemical kinetics”, *The Journal of Chemical Physics*, vol. 100, no. 8, pp. 5735–5750, 1994.
- [177] G. L. Poppe Jr, “Physical applications of the geometric minimum action method”, 2018.
- [178] D. M. Roma, R. A. O’Flanagan, A. E. Ruckenstein, A. M. Sengupta, and R. Mukhopadhyay, “Optimal path to epigenetic switching”, *Physical Review E*, vol. 71, no. 1, p. 011 902, 2005.
- [179] H. Touchette, “The large deviation approach to statistical mechanics”, *Physics Reports*, vol. 478, no. 1-3, pp. 1–69, 2009.
- [180] T. Grafke, T. Schäfer, and E. Vanden-Eijnden, “Long term effects of small random perturbations on dynamical systems: Theoretical and computational tools”, in *Recent Progress and Modern Challenges in Applied Mathematics, Modeling and Computational Science*, Springer, 2017, pp. 17–55.
- [181] M. Heymann and E. Vanden-Eijnden, “The geometric minimum action method: A least action principle on the space of curves”, *Communications on Pure and Applied Mathematics: A Journal Issued by the Courant Institute of Mathematical Sciences*, vol. 61, no. 8, pp. 1052–1117, 2008.
- [182] J. R. Collier, N. A. Monk, P. K. Maini, and J. H. Lewis, “Pattern formation by lateral inhibition with feedback: A mathematical model of delta-notch intercellular signalling”, *Journal of Theoretical Biology*, vol. 183, no. 4, pp. 429–446, 1996.

- [183] N. A. Monk, J. A. Sherratt, and M. R. Owen, "Spatiotemporal patterning in models of juxtacrine intercellular signalling with feedback", *Mathematical Models for Biological Pattern Formation*, pp. 165–192, 2001.
- [184] C. Lv, X. Li, F. Li, and T. Li, "Constructing the energy landscape for genetic switching system driven by intrinsic noise", *PLoS One*, vol. 9, no. 2, e88167, 2014.
- [185] M. Tao, "Hyperbolic periodic orbits in nongradient systems and small-noise-induced metastable transitions", *Physica D: Nonlinear Phenomena*, vol. 363, pp. 1–17, 2018.
- [186] R. D. O’Dea and J. R. King, "Continuum limits of pattern formation in hexagonal-cell monolayers", *Journal of Mathematical Biology*, vol. 64, no. 3, pp. 579–610, 2012.
- [187] M. Cohen, M. Georgiou, N. L. Stevenson, M. Miodownik, and B. Baum, "Dynamic filopodia transmit intermittent delta-notch signaling to drive pattern refinement during lateral inhibition", *Developmental Cell*, vol. 19, no. 1, pp. 78–89, 2010.
- [188] G. L. Hunter, Z. Hadjivasiliou, H. Bonin, L. He, N. Perrimon, G. Charras, and B. Baum, "Coordinated control of notch/delta signalling and cell cycle progression drives lateral inhibition-mediated tissue patterning", *Development*, vol. 143, no. 13, pp. 2305–2310, 2016.
- [189] F. Corson, L. Couturier, H. Rouault, K. Mazouni, and F. Schweisguth, "Self-organized notch dynamics generate stereotyped sensory organ patterns in drosophila", *Science*, vol. 356, no. 6337, 2017.
- [190] P. Formosa-Jordan, M. Ibañes, S. Ares, and J.-M. Frade, "Lateral inhibition and neurogenesis: Novel aspects in motion", *International Journal of Developmental Biology*, vol. 57, no. 5, pp. 341–350, 2013.
- [191] F. Bocci, J. N. Onuchic, and M. K. Jolly, "Understanding the principles of pattern formation driven by notch signaling by integrating experiments and theoretical models", *Frontiers in Physiology*, vol. 11, 2020.
- [192] S. K. Kay, H. A. Harrington, S. Shepherd, K. Brennan, T. Dale, J. M. Osborne, D. J. Gavaghan, and H. M. Byrne, "The role of the hes1 crosstalk hub in notch-wnt interactions of the intestinal crypt", *PLoS Computational Biology*, vol. 13, no. 2, e1005400, 2017.
- [193] M. K. Jolly, M. Boareto, B. Huang, D. Jia, M. Lu, E. Ben-Jacob, J. N. Onuchic, and H. Levine, "Implications of the hybrid epithelial/mesenchymal phenotype in metastasis", *Frontiers in Oncology*, vol. 5, p. 155, 2015.
- [194] Y. Sha, D. Haensel, G. Gutierrez, H. Du, X. Dai, and Q. Nie, "Intermediate cell states in epithelial-to-mesenchymal transition", *Physical Biology*, vol. 16, no. 2, p. 021001, 2019.
- [195] S. Kéfi, M. B. Eppinga, P. C. de Ruiter, and M. Rietkerk, "Bistability and regular spatial patterns in arid ecosystems", *Theoretical Ecology*, vol. 3, no. 4, pp. 257–269, 2010.
- [196] V. Baldazzi, N. Bertin, H. de Jong, and M. Génard, "Towards multiscale plant models: Integrating cellular networks", *Trends in Plant Science*, vol. 17, no. 12, pp. 728–736, 2012.
- [197] E. Farcot, C. Lavedrine, and T. Vernoux, "A modular analysis of the auxin signalling network", *PLoS One*, vol. 10, no. 3, e0122231, 2015.
- [198] G. Zeng, S. M. Taylor, J. R. McColm, N. C. Kappas, J. B. Kearney, L. H. Williams, M. E. Hartnett, and V. L. Bautch, "Orientation of endothelial cell division is regulated by vegf signaling during blood vessel formation", *Blood*, vol. 109, no. 4, pp. 1345–1352, 2007.
- [199] V. Marin, G. Kaplanski, S. Gres, C. Farnarier, and P. Bongrand, "Endothelial cell culture: Protocol to obtain and cultivate human umbilical endothelial cells", *Journal of Immunological Methods*, vol. 254, no. 1-2, pp. 183–190, 2001.
- [200] S. Dimmeler and A. M. Zeiher, "Endothelial cell apoptosis in angiogenesis and vessel regression", *Circulation Research*, vol. 87, no. 6, pp. 434–439, 2000.
- [201] N. Ferrara, "Binding to the extracellular matrix and proteolytic processing: Two key mechanisms regulating vascular endothelial growth factor action", *Molecular Biology of the Cell*, vol. 21, no. 5, pp. 687–690, 2010.

- [202] G. S. Schultz and A. Wysocki, “Interactions between extracellular matrix and growth factors in wound healing”, *Wound Repair and Regeneration*, vol. 17, no. 2, pp. 153–162, 2009.
- [203] C. Bonnans, J. Chou, and Z. Werb, “Remodelling the extracellular matrix in development and disease”, *Nature Reviews Molecular Cell Biology*, vol. 15, no. 12, pp. 786–801, 2014.
- [204] A. Neve, F. P. Cantatore, N. Maruotti, A. Corrado, and D. Ribatti, “Extracellular matrix modulates angiogenesis in physiological and pathological conditions”, *BioMed Research International*, vol. 2014, 2014.
- [205] H. Lavoie, J. Gagnon, and M. Therrien, “Erk signalling: A master regulator of cell behaviour, life and fate”, *Nature Reviews Molecular Cell Biology*, vol. 21, no. 10, pp. 607–632, 2020.
- [206] S. E. Bell, A. Mavila, R. Salazar, K. J. Bayless, S. Kanagala, S. A. Maxwell, and G. E. Davis, “Differential gene expression during capillary morphogenesis in 3d collagen matrices: Regulated expression of genes involved in basement membrane matrix assembly, cell cycle progression, cellular differentiation and g-protein signaling”, *Journal of Cell Science*, vol. 114, no. 15, pp. 2755–2773, 2001.
- [207] R. Kalluri, “Basement membranes: Structure, assembly and role in tumour angiogenesis”, *Nature Reviews Cancer*, vol. 3, no. 6, pp. 422–433, 2003.
- [208] E. Hohenester and P. D. Yurchenco, “Laminins in basement membrane assembly”, *Cell Adhesion & Migration*, vol. 7, no. 1, pp. 56–63, 2013.
- [209] A. N. Stratman, K. M. Malotte, R. D. Mahan, M. J. Davis, and G. E. Davis, “Pericyte recruitment during vasculogenic tube assembly stimulates endothelial basement membrane matrix formation”, *Blood, The Journal of the American Society of Hematology*, vol. 114, no. 24, pp. 5091–5101, 2009.
- [210] S. Ergün, N. Kilic, J.-H. Wurbach, A. Ebrahimnejad, M. Fernando, S. Sevinc, E. Kilic, F. Chala-jour, W. Fiedler, H. Lauke, *et al.*, “Endostatin inhibits angiogenesis by stabilization of newly formed endothelial tubes”, *Angiogenesis*, vol. 4, no. 3, pp. 193–206, 2001.
- [211] L. P. Diebold, H. J. Gil, P. Gao, C. A. Martinez, S. E. Weinberg, and N. S. Chandel, “Mitochondrial complex iii is necessary for endothelial cell proliferation during angiogenesis”, *Nature Metabolism*, vol. 1, no. 1, pp. 158–171, 2019.
- [212] H. Park, H. Yamamoto, L. Mohn, L. Ambühl, K. Kanai, I. Schmidt, K.-P. Kim, A. Fraccaroli, S. Feil, H. J. Junge, *et al.*, “Integrin-linked kinase controls retinal angiogenesis and is linked to wnt signaling and exudative vitreoretinopathy”, *Nature Communications*, vol. 10, no. 1, pp. 1–14, 2019.
- [213] A. Rattner, J. Williams, J. Nathans, *et al.*, “Roles of hifs and vegf in angiogenesis in the retina and brain”, *The Journal of Clinical Investigation*, vol. 129, no. 9, pp. 3807–3820, 2019.
- [214] D. Antfolk, M. Sjöqvist, F. Cheng, K. Isoniemi, C. L. Duran, A. Rivero-Muller, C. Antila, R. Niemi, S. Landor, C. V. Bouten, *et al.*, “Selective regulation of notch ligands during angiogenesis is mediated by vimentin”, *Proceedings of the National Academy of Sciences*, vol. 114, no. 23, E4574–E4581, 2017.
- [215] T.-Y. Kang, F. Bocci, M. K. Jolly, H. Levine, J. N. Onuchic, and A. Levchenko, “Pericytes enable effective angiogenesis in the presence of proinflammatory signals”, *Proceedings of the National Academy of Sciences*, vol. 116, no. 47, pp. 23 551–23 561, 2019.
- [216] D. Nagata, M. Mogi, and K. Walsh, “Amp-activated protein kinase (ampk) signaling in endothelial cells is essential for angiogenesis in response to hypoxic stress”, *Journal of Biological Chemistry*, vol. 278, no. 33, pp. 31 000–31 006, 2003.
- [217] H.-J. Park, Y. Zhang, S. P. Georgescu, K. L. Johnson, D. Kong, and J. B. Galper, “Human umbilical vein endothelial cells and human dermal microvascular endothelial cells offer new insights into the relationship between lipid metabolism and angiogenesis”, *Stem Cell Reviews*, vol. 2, no. 2, pp. 93–101, 2006.
- [218] K. Bentley, K. Harrington, and E. Regan, “Can active perception generate bistability? heterogeneous collective dynamics and vascular patterning”, in *Artificial Life Conference Proceedings 14*, MIT Press, 2014, pp. 328–335.

-
- [219] Y. L. Koon, S. Zhang, M. B. Rahmat, C. G. Koh, and K.-H. Chiam, “Enhanced delta-notch lateral inhibition model incorporating intracellular notch heterogeneity and tension-dependent rate of delta-notch binding that reproduces sprouting angiogenesis patterns”, *Scientific Reports*, vol. 8, no. 1, pp. 1–15, 2018.
- [220] B. Debir, C. Meaney, M. Kohandel, and M. B. Unlu, “The role of calcium oscillations in the phenotype selection in endothelial cells”, *Scientific Reports*, vol. 11, no. 1, pp. 1–12, 2021.
- [221] A. Atri, J. Amundson, D. Clapham, and J. Sneyd, “A single-pool model for intracellular calcium oscillations and waves in the xenopus laevis oocyte”, *Biophysical Journal*, vol. 65, no. 4, pp. 1727–1739, 1993.
- [222] T. H. Cormen, C. E. Leiserson, R. L. Rivest, and C. Stein, *Introduction to algorithms*. MIT press, 2009.
- [223] M. E. Fortini and D. Bilder, “Endocytic regulation of notch signaling”, *Current Opinion in Genetics & Development*, vol. 19, no. 4, pp. 323–328, 2009.